universität wien

MASTERARBEIT | MASTER'S THESIS

Titel | Title

Genome Editing of Mutations in Patient-Derived Lung Cancer Organoids using CRISPR-Cas9-based Technologies

verfasst von | submitted by

Sandy Sulaiman B.Sc.

angestrebter akademischer Grad | in partial fulfilment of the requirements for the degree of

Master of Science (MSc)

Wien | Vienna, 2026

Studienkennzahl lt. Studienblatt | Degree programme code as it appears on the student record sheet:	UA 066 830
Studienrichtung lt. Studienblatt | Degree programme as it appears on the student record sheet:	Masterstudium Molecular Microbiology, Microbial Ecology and Immunobiology
Betreut von | Supervisor:	Univ.-Prof. Dr. Joao Matos

Contents

1 Abstract **1**

2 Abstrakt **2**

3 Introduction **3**

3.1 Lung Cancer: Background and Clinical Relevance 3
3.2 *TP53* Mutations 5
3.3 *RET* as an Oncogenic Driver in NSCLC 6
3.4 Patient-derived Lung Tumor Organoids 7
3.5 CRISPR-Cas9 Genome Editing 9
3.6 CRISPR Base Editing 10
3.7 Development of NG-ABE8e 13
3.8 CRISPR-Cas9 and Base Editor Delivery Strategies 14
3.9 Clinical and therapeutic Applications 16
3.10 Aims of the Thesis 19
3.10.1 Correcting *TP53* C275Y mutation and its functional analysis using adenine base editing 19
3.10.2 CRISPR–Cas9–based inactivation of the KIF5B–RET fusion oncogene 19

4 Materials and Methods **22**

4.1 Organoid Culture 22
4.2 Genotyping of PMU315 *TP53* exon8 23
4.3 Genotyping of PMU315 KIF5B-RET fusion breakpoint site 24
4.4 Primer Design for Validating the KIF5B:RET Fusion Breakpoint 25
4.5 Design of small guide RNA (sgRNA) 26
4.6 gRNAs Cloning into Lentiviral Vectors 26
4.6.1 Oligos Annealing 27
4.6.2 Restriction/Ligation Golden Gate 27
4.6.3 Bacterial Transformation 27
4.7 Cloning of Adenine Base Editor into Lentiviral Vector 27
4.8 Cell Culture 28
4.9 Lentivirus Production 28
4.10 Transduction of Lung Organoids 29
4.11 Flow Cytometry Analysis 29
4.12 EditR to quantify base editing efficiency 30
4.13 Materials, Equipments and Medias 31
4.13.1 Reagents and Kits 31
4.13.2 Materials for Cell and Organoid Culture 31

4.13.3 Equipments 32
4.13.4 Media and solutions for organoid culture 32

5 Results **34**
5.1 Correcting *TP53* C275Y Mutation in Patient-Derived Lung Cancer Organoids 34
5.1.1 Confirmation of the *TP53* C275Y Mutation in the PMU315 Lung Cancer Organoid Line 35
5.1.2 Generation of Lung Cancer Organoid Line Expressing NG-ABE8e Base Editor 36
5.1.3 Efficient Correction of the *TP53* C275Y (G→A) Mutation in Lung Cancer Organoids Using Adenine Base Editing Approach 39
5.1.4 Early Time Course Analysis Reveals Efficient Correction of the TP53 C275Y (G→A) within 12 Hours following Adenine Base Editing Approach 43
5.1.5 Deviation between Editing Efficiency and tdTomato Expression Suggests Partial Viral Packaging or Reporter Silencing 46
5.1.6 Characterization of tdTomato Reporter Expression in Panc-1 Cells 48
5.2 Targeting approaches of Fusion Oncogene KIF5B:RET in Lung Cancer Organoids 49
5.2.1 Validation of oncogenic Fusion *KIF5B-RET* in PMU315 organoids 51
5.2.2 Targeting *KIF5B-RET* Fusion Oncogene in Lung Cancer Organoids using CRISPR-Cas9 based viral Infection Approach 54
5.2.3 Targeting *KIF5B-RET* Fusion Oncogene in Lung Cancer Organoids using RNA Transfection Approach 56

6 Discussion **60**
6.1 TP53 C275Y Correction 60
6.1.1 Efficient and Rapid Correction of the TP53 C275Y Mutation in Lung Cancer Organoids 61
6.1.2 Functional Consequences of TP53 Correction 61
6.1.3 Deviation between Editing Efficiency and Reporter Expression . . 62
6.1.4 Implications and Future Directions 63
6.2 Targeting the Oncogenic Fusion *KIF5B-RET* 64
6.2.1 Validation of oncogenic Fusion *KIF5B-RET* in PMU315 organoids 64
6.2.2 Targeting *KIF5B-RET* Fusion Oncogene in Lung Cancer Organoids using CRISPR-Cas9 based viral Infection Approach 65
6.2.3 Targeting KIF5B-RET Fusion Oncogene in Lung Cancer Organoids using RNA Transfection Approach 65
6.2.4 Future Optimization 66

7 Conclusion **67**

8 Supplement **76**

9 Acknowledgments **81**

List of Figures

Figure 1 Global cancer mortality distribution 3
Figure 2 Microscopic image of the PMU315 patient-derived lung cancer. . 8
Figure 3 Molecular principles of CRISPR genome editing 12
Figure 4 Schematic workflow of the experimetns. 21
Figure 5 PMU315 organoids stained with hematoxylin and eosin 23
Figure 6 Example output from the EditR analysis 30
Figure 7 Validation of the *TP53* C275Y (G→A) mutation in PMU315 lung cancer organoids. 35
Figure 8 Schematic of *TP53* C275Y Mutation Site and sgRNA Design . . . 36
Figure 9 Flow cytometric Plots of GFP-positive cells infected with pL-ABE8e. 37
Figure 10 Puromycin kill curve of wild-type PMU315 lung cancer organoids. 38
Figure 11 Establishment of ABE8e organoid line using puromycin. 39
Figure 12 Time course analysis of tdTomato-positive cells in PMU315 *TP53* C275Y organoids over 26 days after infection. 40
Figure 13 PCR amplification of *TP53* exon 8 in PMU315 organoids at day 4 after lentiviral infection. 41
Figure 14 Sanger sequencing chromatograms of *TP53* (G→A) mutation at 4 dpi. 42
Figure 15 Early time course analysis of tdTomato-positive cells in PMU315 *TP53* C275Y organoids over 96 hours after infection 43
Figure 16 PCR amplification of *TP53* exon 8 in PMU315 organoids at 12 and 48 hours after lentiviral infection. 44
Figure 17 Sanger sequencing chromatograms of *TP53* (G→A) mutation at early time point, 16 hpi. 45
Figure 18 EditR Quantification of predicted editing percentage of *TP53* C275Y (G→A) at early time points 46
Figure 19 Flow cytometric Plots of tdTomato-positive cells at 12 hpi and 4 dpi with sgC275Y-gRNA1. 47
Figure 20 Time course of tdTomato-positive Panc-1 cells over 72 hours . . 49
Figure 21 Schematic representation of *KIF5B–RET* fusion region and primer design strategy. 51
Figure 22 PCR amplification and validation of *KIF5B–RET* fusion. 53
Figure 23 Schematic representation of the *KIF5B–RET* fusion and gRNA design. 54
Figure 24 GFP expression following mRNA transfection at 3 days post-transfection (3 dpt). 57

Figure 25 Effect of *RET:KIF5B* targeting on organoid viability at 3 and 7 days post-transfection. 58
Figure 26 Sanger sequencing validation of CRISPR–Cas9-induced edits in KIF5B and RET target introns. 59
Figure 27 ICE analysis of CRISPR editing outcomes using EditCO software. 60
Figure S1 gRNA designs for dual intron targeting of the KIF5B::RET fusion. 77
Figure S2 Lentiviral Plasmid pL-ABE8e 78
Figure S3 Lentiviral Plasmid pL-CRISPR-Cas9 79
Figure S4 Lentiviral Plasmid with gRNA, tdTomato, P2A and Blasticidin resistance (LRT2B) 80

Abbreviations

CRISPR	Clustered regularly interspaced short palindromic repeats
Cas9	CRISPR-associated protein
bp	Base pair of DNA
sgRNA	Single guide RNA
ABE	Adenine Base Editing
ABE8e	Evolved Adenine Base Editor 8e
CBE	Cytosine Base Editing
Amp	Ampicillin
DNA	Deoxyribonucleic acid
dNTP	Deoxynucleoside triphosphate
DSB	double stranded DNA break
FACS	Fluorescence-activated cell sorting
E. coli	Escherichia coli
gDNA	Genomic DNA
RET	Rearranged during Transfection
TKI	tyrosine kinase inhibitors
KIF5B	Kinesin Family Member 5B
PMU	Preclinical Model Unit
F+++	Advanced DMEM-Medium/F12 mit GlutaMAX, HEPES und Penicillin-Streptomycin
Y-27632	(1R,4r)-4-((R)-1-aminoethyl)-N-(pyridin-4-yl)cyclohexanecarboxamide
NSCLC	Non-Small Cell Lung Cancer
DBD	DNA-Binding Domain
FACS	Fluorescence-Activated Cell Sorting
tdTomato	Tandem Dimer Tomato Fluorescent Protein

GFP Green Fluorescent Protein

NCT National Center for Tumor Diseases (your collaborator)

TP53 Tumor Protein p53

CAR-T Chimeric Antigen Receptor T cell

1 Abstract

Lung adenocarcinoma is caused by various genetic alterations, including tumor-suppressor mutations and oncogenic gene fusions, which together shape tumor progression and remain difficult to therapeutically target due to resistance development. Patient-derived lung cancer organoids offer a physiologically relevant model for studying these alterations and evaluating emerging genome-editing strategies. This thesis applies CRISPR-based technologies in lung cancer organoids to functionally dissect two clinically relevant mutations: the TP53 C275Y mutation and the KIF5B–RET fusion oncogene. An adenine base editor (ABE) was used to correct the TP53 C275Y (G→A) mutation within the DNA-binding domain of p53. High-efficiency A→G conversion (60–90%) was achieved in organoids using a lentiviral delivery system. Correction of the mutation resulted in a significant reduction in organoid viability (>75% depletion of live cells) already within three days, indicating reactivation of p53-medited tumor-suppressive programs. The second project aimed to disrupt the oncogenic KIF5B–RET fusion using CRISPR–Cas9 delivered via a virus-free (m)RNA transfection approach. Two strategies were designed: (i) break-point targeting and (ii) dual-intron targeting to induce large deletions independent of the fusion junction. One guide RNA achieved 15% editing. However, low editing and limited phenotypic impact likely resulted from p53-mediated error-free repair mechanisms. These can potentially preserve the KIF5B–RET oncogene and limit knockout efficiency. These findings establish a robust workflow for base editing in patient-derived organoids and demonstrate the feasibility of studying TP53 hotspot mutations in their native environment and in a patient-specific context. In addition, it demonstrates how genome-editing platforms can facilitate functional characterization of cancer mutations and support the development of personalized therapeutic strategies in non-small cell lung cancer and beyond.

2 Abstrakt

Lungen Adenokarzinom entsteht durch verschiedene genetische Veränderungen, darunter Mutationen in Tumorsuppressor und onkogene Genfusionen, die gemeinsam das Tumorprogressionsverhalten bestimmen. Aufgrund von Resistenzentwicklungen sind diese Mutationen therapeutisch schwierig zu behandeln. Allerdings bieten Patientenabgeleitete Organoide ein physiologisch relevantes Modellsystem, um diese Veränderungen zu untersuchen und neue genomeditierende Methoden zu evaluieren.
In dieser Arbeit wurden CRISPR-basierte Technologien in Lungenkrebs-Organoiden eingesetzt, um zwei klinisch relevante genetische Veränderungen funktionell zu analysieren: die *TP53* Mutation C275Y sowie die onkogene *KIF5B-RET* Fusion. Zur Korrektur der *TP53* C275Y Mutation (G→A) in der DNA-Bindungsdomäne von p53 wurde das Adenin-Basen-Editierung System ABE8e verwendet. Mittels Lentiviren konnten CRISPR Komponenten in die Organoiden geliefert werden und eine hohe A→G-Umwandlungseffizienz von 60–90% erzielt werden. Die Korrektur der Mutation führte zu einer deutlichen Wachstumshemmung der Organoiden (> 75% Verlust lebender Zellen), was auf die Reaktivierung p53-vermittelter tumorsuppressiver Programme hinweist. Im zweiten Teil des Projekts wurde die onkogene KIF5B-RET-Fusion mittels CRISPR-Cas9 gezielt inaktiviert. Das erfolgte über eine virusfreie (m)RNA-Transfektion. Es wurden zwei Strategien entwickelt: (i) eine Breakpoint-spezifische gezielte Inaktivierung und (ii) eine Doppelte Intron-Inaktivierung zur Induktion einer großen Deletion unabhängig von der genauen Fusionsstelle. Eine der verwendeten gRNAs erreichte einen Editingprozentsatz von 15%. Die geringe Effizienz und der ausbleibende phänotypische Effekt könnten auf ein mögliche Gen-Stilllegung der Cas9 oder auf durch mutiertes p53 induzierte fehlerfreie DNA-Reparaturmechanismen zurückzuführen sein, welche die Funktion des KIF5B-RET-Onkogens erhalten und damit die Knockout-Effizienz begrenzen. Insgesamt etabliert diese Arbeit einen robusten Arbeitsablauf für Adenin-Basen-Editierung in patientenspezifischen Organoiden, demonstriert die Machbarkeit der funktionellen Untersuchung von TP53 Punktmutationen im tumorrelevanten Umfeld. Außerdem zeigt diese Arbeit wie genomeditierende Plattformen zur funktionellen Charakterisierung von Krebs verbundene Mutationen beitragen. Damit liefert sie wichtige Grundlagen für die Entwicklung personalisierter Therapiestrategien beim Lungenkrebs.

3 Introduction

3.1 Lung Cancer: Background and Clinical Relevance

Cancer is a genetic disease driven by the accumulation of somatic mutations that deregulate cellular proliferation, survival, and differentiation [1]. Lung cancer is the most commonly diagnosed cancer worldwide and remains the leading cause of cancer-related mortality, responsible for approximately 1.8 million deaths per year and nearly 19% of all cancer deaths [2]. The high mortality rate is largely attributed to late stage detection and the aggressive biological behavior of several subtypes. Lung cancer is broadly classified into two main groups: non–small cell lung cancer (NSCLC), which represents approximately 85% of cases, and small cell lung cancer (SCLC), which makes up the remaining 15% [3]. NSCLC includes several histological subtypes such as adenocarcinoma (ADC), squamous-cell carcinoma (SCC), adenosquamous carcinoma (ASC) and large-cell carcinoma (LCC)(Herbst et al., 2018). Among these, lung adenocarcinoma is the most frequent, representing about 40% of NSCLC cases.

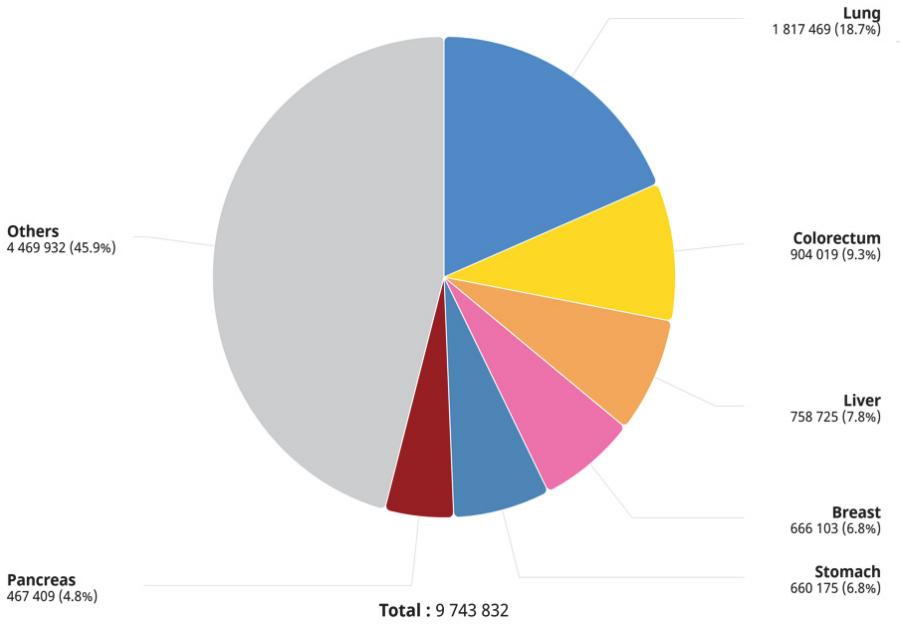

Figure 1: **Global cancer mortality distribution** Chart showing the proportion of cancer-related deaths worldwide, based on data from the International Agency for Research on Cancer. Lung cancer accounts for the largest share of mortality (18.7%). Absolute numbers, Mortality, Both sexes, in 2022 [2].

Like many cancers, NSCLC is driven by genetic alterations that activate growth-promoting pathways and support malignant transformation [1]. Genomic abnormalities arise either from the activation of oncogenes or the loss of function of tumor-suppressor genes. Mutations in proto-oncogenes convert them into oncogenes, which drive uncontrolled

cell proliferation. In contrast, tumor-suppressor genes act as cellular brakes, leading the cell cycle to stop and promoting cell death when necessary. When these genes are mutated, their ability to maintain genomic integrity is compromised, apoptosis is impaired, and malignant growth can no longer be effectively suppressed.

The most common genetic alterations in lung cancer are oncogenic mutations in EGFR, ALK, ROS1, KRAS, ERBB2, BRAF, RET, and MET [1]. Most of these genes encode for receptor tyrosine kinases, which are permanently activated by oncogenic mutations in a ligand-independent manner and thus activate downstream signaling pathways such as the RAS/RAF/MAPK signaling pathway [4]. This in turn leads to uncontrolled cell growth and survival [**signal**].

Therapeutically, tyrosine kinase inhibitors (TKI) can be used to suppress this permanent activation by binding to specific sites on the receptors [5]. Numerous clinical studies have shown that patients with NSCLC can be treated more effectively and with fewer side effects using TKIs compared to conventional chemotherapies, when their tumor show oncogenic mutations in the mentioned genes [6]. However, this only applies for one third of all lung cancer patients [6].
A major clinical challenge is that many lung adenocarcinomas do not carry targetable oncogenic drivers, leaving patients dependent on conventional chemotherapy [5]. Furthermore, therapeutic pressure leads to the development of secondary resistance mutations in almost all driver-mutated NSCLC, which limits the effectiveness of such targeted therapies [7]. Although patients with oncogenic mutations typically experience longer progression-free survival when treated with TKIs compared to chemotherapy, secondary resistance mutations often arise within a year, requiring alternative treatment strategies [8]. This highlights the importance of characterizing the complete mutational landscape of NSCLC, not only to guide initial therapy, but also to anticipate and manage drug resistance.

Among all genetic alterations in NSCLC, *TP53* mutations stand out due to their extremely high prevalence and broad impact on tumor biology [9]. *TP53* is the most frequently mutated gene in human cancers, and its inactivation is particularly common in NSCLC [10]. NSCLC Patients with mutations in *TP53* generally exhibit poorer responses to chemotherapy and radiation and have worse overall survival [11]. Despite its importance, to date there are no effective targeted therapies for *TP53* mutations [9]. Therefore, a major clinical challenge in the treatment of lung cancer is the development of drugs that can be used for as many patients as possible over a long period of time. Characterizing the mutational landscape and understanding the biology of different mutations seems to be crucial to develop new promising therapeutics in the future.

3.2 *TP53* Mutations

The *TP53* gene, located on chromosome 17p13.1, encodes the tumor suppressor protein p53, often called the "guardian of the genome" [12]. p53 acts as a transcription factor that regulates the cell cycle in response to stress signals, such as DNA damage or oncogene activation, by controlling the expression of genes involved in cell cycle arrest, apoptosis, DNA repair, and senescence [13]. Mutations in *TP53* are the most frequent genetic alterations in human cancers, occurring in about 50% of all cases [10]. In lung cancer, *TP53* mutations are found in 45–80% of cases, with higher prevalence in smoking-related adenocarcinomas according to Cancer Genome Atlas (TCGA) database. Structurally, p53 is a 393-amino-acid protein composed of several key domains, including the central DNA-binding domain (DBD), which recognizes specific promoters of p53 target genes. Most *TP53* mutations are single amino acid substitutions in the DBD, spanning exons 5–8, which include hotspot regions [14]. Mutations at hotspots such as R175, G245, R248, R273, and R282 are the most common genetic changes in human cancers, present in 5–10% of all samples tested [15] [16].
Some of the hotspot mutations in *TP53* can eliminate its normal tumor-suppressive roles resulting in loss-of-function (LOF) mutations. In contrast, some other hotspot mutations give the protein new functions that help cancer cells survive and grow, resulting in gain-of-function mutations (GOF) [17]. These mutations often occur at specific hotspot sites within DBD and there are two main types of these sites: Contact mutants (such as R273H, R248Q, R248W) mainly disrupt how p53 binds DNA, while conformational mutants (such as R175H, G245S, R249S, R282H) alter the protein's folding. Both types are known to produce GOF effects [17]. Additionally, the buildup of mutant p53 inside cells can amplify signaling pathways driven by these GOF activities which highlights the complexity of p53 genetics [17].

Several drugs have been developed to either reactivate mutant p53, such as APR-246 (Eprenetapopt) or promote its selective degradation (like HSP90 inhibitors). However, none have yet shown clear or consistent clinical efficacy in *TP53*-mutant cancers, and no *TP53*-mutation–targeted therapy has been clinically approved [18].
Given these limitations, genome editing technologies, such as adenine base editors (ABEs), offer a promising approach for permanently restoring wild-type *TP53* sequence. Studies in cell lines have shown that base editing can be used to correct *TP53* point mutations, and this correction can restore p53 function and lead to tumor cell depletion [19] [20].

3.3 *RET* as an Oncogenic Driver in NSCLC

In healthy tissue, proto-oncogenes function as key regulators of cell proliferation and differentiation. Alterations in their gene sequence affect the structure of their resultant proteins, which in turn change multiple regulatory growth factors and signal transduction events that control the dynamics of normal cell differentiation and proliferation. When such changes lead to constitutive activation of a downstream signaling pathway, proto-oncogenes become oncogenes that drive malignant cell growth. This activation can arise through point mutations, chromosomal rearrangements, or epigenetic alterations [21]. For example the *RET* gene encodes a transmembrane receptor tyrosine kinase (RTK) with proto-oncogenic properties. Under physiological conditions, *RET* interacts with neurotrophic ligand-receptor complexes, leading to receptor dimerization, autophosphorylation and activation of downstream signaling pathways such as RAS/MAPK. In NSCLC, chromosomal rearrangements that fuse the *RET* kinase domain to a partner gene result in ligand-independent constitutive activation of these pathways driving uncontrolled cell growth and survival [22].

RET fusions occur in approximately 1–2 % of NSCLC cases, with KIF5B–RET being the most common variant (70 % of *RET*-positive tumors) [23]. Selective *RET* inhibitors, including selpercatinib and pralsetinib, have shown good clinical responses comparing to conventional therapies [5]. However, acquired resistance -similar to resistance observed with other targeted therapies, limits their long term efficacy [24].

A broader challenge in NSCLC is the presence of additional oncogenic drivers such as mutated *KRAS* and *EGFR*. Although targeted therapies have improved patient outcomes, they rarely eliminate disease entirely. For example, EGFR-mutant NSCLC typically responds well to third-generation TKIs such as osimertinib, but resistance emerges within about one year of progression-free survival (PFS), often through activation of bypass signaling pathways [7]. *RET* fusions can constitute one such bypass mechanism, enabling tumors to evade *EGFR* inhibition. Chromosomal rearrangements involving *RET* promote activation of MAPK and PI3K–AKT signaling and contribute to acquired TKI resistance [24].

This therapeutic challenge highlights the genetic complexity of *RET* mutations in tumors and the need for new treatment approaches which permanently disrupt chromosomal rearrangements involving the RET gene at DNA level. Emerging genome-editing tools including CRISPR–Cas nucleases offer wide possibilities by enabling selective disruption of oncogenic fusions such as KIF5B-RET [25].

3.4 Patient-derived Lung Tumor Organoids

Organoids are three-dimensional microtissues that mimic important aspects of the structure and function of the corresponding tissue in the body [26]. Organoids derived from pluripotent stem cells, tissue-resident stem cells, or differentiated cells from healthy or diseased tissues, including tumors. Therefore, patient-derived organoids are valuable tools for studying multiple aspects of tumor biology, making them better models for translational cancer research [27]. Compared with 2D cell lines, patient-derived organoids preserve the complexity and heterogeneity of origin tissues, allowing experimental studies such as testing therapeutic drug efficacy and toxicity, as well as assessing individual drug responses [28]. Thus, patient-derived tumor organoids provide a closer experimental model to the patient while maintaining features of the original tumor microenvironment [29]. Organoids derived from metastatic lesions are particularly useful because they retain therapy-resistant cells that often lead to treatment failure and poor clinical outcomes [29]. Generating patient-derived organoids from diverse human cancers enables researchers to study specific mutations and the tumor heterogeneity in more detail.

In addition to their use in drug-response profiling, patient-derived organoids are increasingly emerging as powerful diagnostic tools. Their ability to preserve patient-specific genetic backgrounds makes them highly suitable for functional genomics approaches using CRISPR screens [28]. These approaches allow researchers to systematically interrogate gene function, identify tumor dependencies, and uncover mechanisms driving tumor progression or therapy resistance. Here is an example of the application of organoids in CRISPR based clinical research. CRISPR-based mutagenesis can be used to generate specific single point mutations directly in tumor organoids obtained from patients, enabling a functional assessment of how individual variants of specific genes influence T-cell responsiveness within the tumor. For example, several studies have shown that organoid-based CRISPR screening can reveal the functional effects of patient-specific mutations on antitumor immunity and resistance to immunotherapies [30].
Such functional characterization pipelines hold substantial diagnostic promise, as they can help pinpoint actionable mutations and ultimately guide personalized therapeutic strategies for individual patients. By enabling these precise, patient-specific analyses, organoids serve as an essential platform that bridges genomic discovery with clinically meaningful decision-making.
At the National Center for Tumor Diseases (NCT/UCC) Dresden, Patient-derived Tumor Model Units (PMU) organoids are created to systematically study and test cancer mutations. Within the PALUGA clinical trial (“Von Patienten-abgeleitete Lungentumor-

Organoide in der Präzisionsonkologie"), the PMU grows lung cancer tissue into 3D organoids, drug testing is performed, and well-characterized PMUs are generated for use in precision oncology and personalized medicine. In this context, our collaborators at NCT Dresden developed a patient-derived organoid line, PMU315, from a liver metastasis of a 55-year-old female patient with lung adenocarcinoma (smoker, 4 pack-years). This organoid keeps the tumor's genetic profile, including a KIF5B-RET fusion- and a C275Y mutation in the *TP53* gene. The C275Y mutation (cysteine → tyrosine at codon 275, due to G> A single substitutions) is located in the DNA-binding domain of p53, very close to known hotspot mutations at R248, R273, and R282, and therefore is likely affecting the function of p53. As a representative *TP53* point mutation, PMU315 provides a highly relevant model to test our gene base editing approach designed to correct this point mutation, and to functionally analyze the biological consequences of this mutation in a clinically meaningful setting.

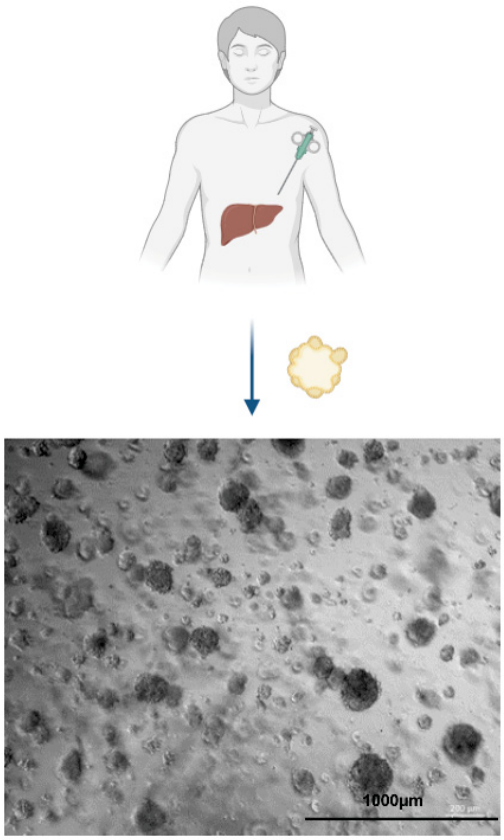

Figure 2: **Microscopic image of the PMU315 patient-derived lung cancer organoid**. The organoid retains a three-dimensional structure, reflecting key features of the original lung cancer metastasis from the liver, and serves as a model for functional studies of the *TP53* C275Y point mutation and KIF5B-RET fusion. Scale bar = 1000 µm.

3.5 CRISPR-Cas9 Genome Editing

Driver mutations are the molecular engines that fuel NSCLC. These alterations cause continuous activation of oncogenes and promote uncontrolled cell proliferation, as well as resistance to chemotherapy, radiation, and checkpoint blockade therapies [8]. Since standard treatments do not eliminate the underlying genetic cause of the disease, there is strong interest in strategies that directly correct or disable mutant alleles. Recent advances in CRISPR-Cas genome editing technologies have opened the door to such precise interventions.

The CRISPR-Cas9 system has revolutionized genome engineering by enabling accurate, sequence-specific double-strand breaks (DSB) that allow knockout of oncogenic drivers, insertion of corrective sequences, or base editing to restore wild-type function of a specific gene [31]. CRISPR systems are powerful genome-editing tools that originate from the adaptive immune system of bacteria and archaea. The first clues about this system emerged in 1987, when unusual repetitive DNA sequences were discovered in the E. coli genome. These repeats, separated by unique sequences from past viral infections, were later recognized as a genetic record of bacterial encounters with phages [32].

The name CRISPR, short for Clustered Regularly Interspaced Short Palindromic Repeats, refers to these spacer-repeat arrays. When a bacterium survives a viral attack, it captures a fragment of the viral genome and inserts it as a new spacer in the CRISPR locus, creating a heritable archive of invaders. The CRISPR array is transcribed, and the transcript is processed into individual CRISPR RNAs (crRNAs), later known as guide RNAs (gRNAs). These gRNAs pair with Cas proteins to form a surveillance complex that identifies and cleaves complementary viral DNA [33].

A major breakthrough occurred in 2012, when biochemical studies showed that Cas9 functions as a programmable DNA endonuclease in mammalian cells [31]. Cas9 activity is guided by a dual-RNA structure consisting of a CRISPR RNA (crRNA) and a trans-activating crRNA (tracrRNA). This discovery enabled the development of CRISPR–Cas9 genome editing: by designing a single-guide RNA (sgRNA) that combines both RNAs and contains a 20-nucleotide target sequence, Cas9 can be directed to nearly any genomic site. The Streptococcus pyogenes Cas9 (SpCas9) is the first Cas nuclease used for genome editing and remains widely used because of its high activity and specificity [31]. SpCas9 belongs to the type II CRISPR system, in which the tracrRNA pairs with the precursor CRISPR RNA (pre-crRNA) to allow RNase-mediated processing into mature gRNAs. These gRNAs then guide Cas9 to a complementary DNA protospacer adjacent to a compatible protospacer adjacent motif (PAM).

Cas9 first recognizes the PAM, which causes nearby DNA to unwind so the guide RNA can pair with the target strand. Once the RNA matches the DNA, Cas9 undergoes conformational changes that activate its nuclease domains. After Cas9 binds the protospacer, the HNH and RuvC domains cleave opposite DNA strands three nucleotides upstream of the PAM (17 nucleotides from the gRNA 5' end), producing a blunt double-strand break [34] (Fig. 3).

Genome-editing strategies usually work by generating targeted double-strand breaks (DSBs) that the cell must repair. When Cas9 introduces a DSB, the break is mainly resolved by non-homologous end-joining (NHEJ) and less frequently by homology-directed repair (HDR) (Fig. 3) or Microhomology-mediated end joining (MMEJ) [35].

In mammalian cells, NHEJ is the dominant repair pathway. It reconnects the broken DNA ends without a template [35]. This process often removes or adds a few nucleotides before ligation, generating insertions or deletions (indels). Repeated cycles of cleavage and repair can accumulate indels until the target site is no longer recognized. These indels can disrupt gene reading frames or remove essential coding regions, making end-joining an effective method for generating gene knockouts [36]. Introducing two DSBs close together can also delete larger DNA segments, enabling complete removal of defined genomic regions through dual-targeting approaches.

HDR or homology-dependent repair is an error-free pathway that requires a homologous DNA template (sister chromatid or an exogenous donor) [35]. Extensive 5'→3' resection creates long ssDNA tails that invade the template allowing DNA synthesis and precise sequence replacement (Fig. 3). HDR is restricted to S/G2 phases of the cell cycle when a template is available [35].

3.6 CRISPR Base Editing

CRISPR–Cas9–based editing induces DSBs and is effective for gene disruption and general genome modifications. However, precise correction of single-nucleotide variants remains challenging because of inefficient and infrequent homology HDR in most cell types. The HDR pathway is required for precise repair after Cas9 induced DSB. These limitations drove the development of "second-generation" CRISPR systems that edit DNA without generating DSBs. One of the most significant innovations in this category is the base editor (BE)[34].

CRISPR-derived base editors enable targeted conversion of single nucleotides without

breaking both DNA strands or supplying a repair template, making them especially useful for correcting point mutations. Base editors consist of an impaired Cas protein with an inactivated RuvC domain (a nickase form of Cas9) fused to a DNA-modifying enzyme, typically a nucleotide deaminase. The Cas9 nickase is directed to the target sequence through its binding to a guide RNA. Once the target is recognized, the gRNA binds the DNA strand containing the PAM and forms an R-loop, exposing a segment of single-stranded DNA that serves as activating substrate for the deaminase [37] (Fig. 3). Two major types of base editors have been developed. Cytosine base editors (CBEs) use cytidine deaminases such as APOBEC1, together with a uracil glycosylase inhibitor, to convert cytosine to thymine. Adenine base editors (ABEs) convert adenine to guanine using an evolved form of the TadA deaminase capable of acting on single-stranded DNA. The first highly efficient ABE variant, ABE7.10, was derived from TadA-7.10, a deoxyadenosine deaminase engineered from the E. coli tRNA adenosine deaminase TadA [37]. After the Cas9 nickase binds its target site, the displaced non-target DNA strand becomes accessible to the deaminase. Within a defined "editing window," CBEs or ABEs convert cytosine or adenine into uracil or inosine, respectively, which are read during DNA replication as thymine or guanine (Fig. 3). These changes allow predictable and precise introduction of transition point mutations [34].

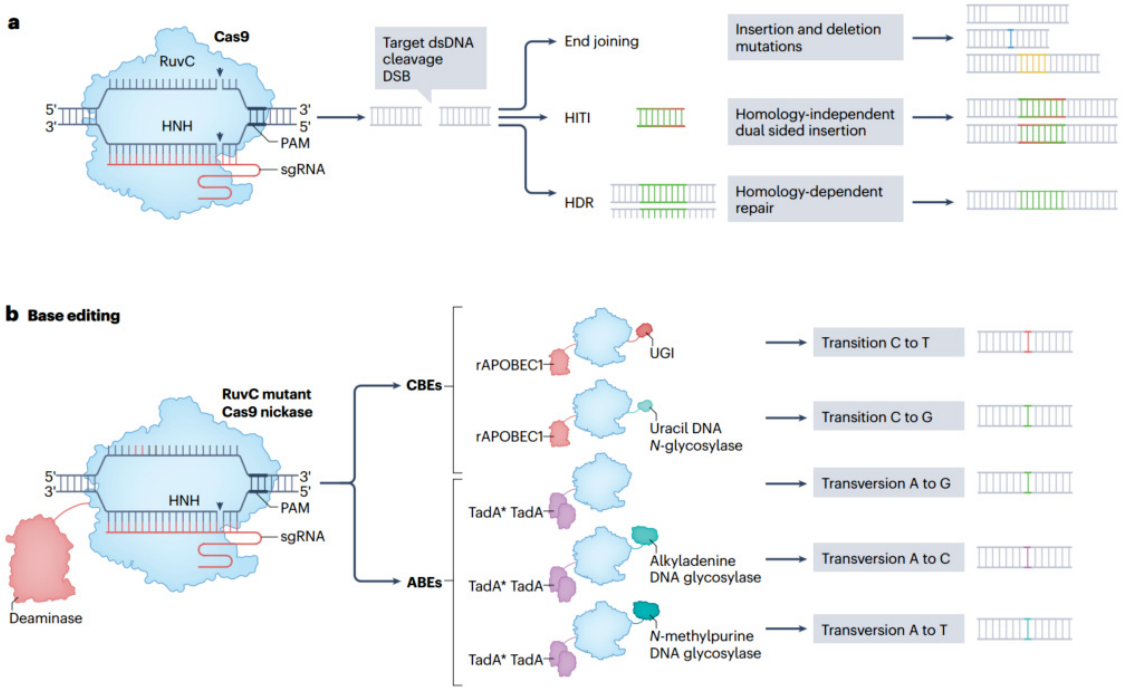

Figure 3: **Molecular principles of CRISPR genome editing. a.** Cas9 nucleases use guide RNAs to target specific genomic sites and create double-strand breaks (DSBs). These breaks are generated by the RuvC and HNH nuclease domains. A protospacer adjacent motif (PAM) located downstream of the gRNA target site is required for cleavage. Once a DSBs are induced, cells can repair it through three major pathways. The first, non-homologous end joining (NHEJ), typically results in insertions or deletions (indels). The presence of donor templates can further shape repair outcomes: homology-independent targeted insertion (HITI) allows integration of double-stranded DNA lacking homology, whereas homology-directed repair (HDR) uses flanking homology sequences from either dsDNA or ssDNA templates, linear or circular. In most cell types, NHEJ predominates. **b.** Base editing using cytosine base editors (CBEs) or adenine base editors (ABEs) employs a Cas9 nickase (impaired Cas9) fused to a nucleotide deaminase. After gRNA binding, an R-loop forms, exposing the target single-stranded DNA distal to the PAM for deamination. ABEs use an engineered adenosine deaminase TadA to mediate A-to-G conversions. Fusion of alkyladenine DNA glycosylase or N-methylpurine DNA glycosylase to ABEs enables additional A-to-C or A-to-T editing. In this study we will use a ABE to correct a G to A substitution. Figure adapted from Villiger et al. (2024)[34].

3.7 Development of NG-ABE8e

The use of base editors was initially constrained by the requirement that the target nucleotide had to fall within the editor's specific "editing window," which is determined by the Cas9 nickase and its associated PAM sequence. Over time, both CBE and ABE platforms have been optimized to improve editing efficiency and minimize unwanted deaminase activity at off-target sites. Base editors with narrower editing windows show reduced bystander editing, and the size of the editing window depends on both the Cas protein and the fused deaminas. For example, SaCas9 generates a broader editing window than SpCas9 even when fused to the same deaminase [34]. Traditional adenine base editors (ABEs) typically edit adenines across a window spanning approximately four nucleotides (protospacer positions 4–7, counting the PAM as positions 21–23) [37]. Through engineering of the deaminase domain, researchers have refined these windows and reduced unwanted sequence preferences, thereby lowering both bystander edits and off-target effects [34]. Early ABE variants, such as ABE7.10, contained a non-catalytic TadA subunit that caused unwanted RNA deamination. Introduction of specific mutations within the adenosine deaminase significantly decreased these off-target RNA edits and gave rise to variants with improved editing windows [38].

Continued evolution ultimately produced ABE8e, a TadA-8e variant with greatly enhanced on-target activity and compatibility with a broader range of Cas proteins [38]. The developed TadA-8e variants showed greatly improved deoxyadenosine deamination activity. NG-ABE8e incorporates a Cas9 variant that recognizes an NG PAM, expanding the number of accessible genomic targets while maintaining the highly active and compact TadA-8e deaminase core. Its editing window spans protospacer positions 4–8, counting the PAM as positions 21–23, thereby expanding the effective targeting scope compared with earlier ABEs. As a result, ABE8e variants can efficiently target positions that were previously difficult to edit using ABE7.10. This refined window, together with the reduced off-target profile inherited from TadA-8e and its higher deamination activity, makes NG-ABE8e particularly suitable for therapeutic applications requiring accurate single-base correction [38].

Because ABEs generate predictable outcomes and enable high-fidelity correction of pathogenic alleles without creating double-strand breaks, base editors have become widely used for genome-wide screens and for repairing mutations in genetic diseases caused by single-base substitutions. The compact and confined editing window of NG-ABE8e, alongside its reduced RNA off-target activity, provides a cleaner transcriptomic profile [38]. These features make ABE8e a promising candidate for repairing *TP53* mutations, where even a single unintended missense variant could convert p53 from a

tumor suppressor into a gain-of-function oncogenic protein. Precise editing is therefore crucial to avoid disrupting regulatory elements or generating secondary mutations. Previous research has shown that *TP53* and *KRAS* base editing is possible using ABE8e in cell lines and even in patient-derived pancreatic organoids [19].

3.8 CRISPR-Cas9 and Base Editor Delivery Strategies

Efficient delivery of genome-editing components is essential for successful CRISPR–Cas9 and base-editing applications. Because the CRISPR machinery is large and sensitive to degradation, specialized delivery systems are required to transfer Cas9 proteins and gRNAs in the form of DNA, RNA, or ribonucleoprotein (RNP) complexes into target cells [39]. Delivery strategies are broadly divided into viral and non-viral vectors, each offering distinct advantages, limitations, and suitability for specific experimental or therapeutic contexts (Table 1).

Viral vectors exploit the natural ability of viruses to introduce genetic material into host cells. The most commonly used viral systems for CRISPR delivery include lentiviruses, adenoviruses, and adeno-associated viruses (AAVs) [39]. These vectors differ in genome capacity, immunogenicity, and genome-integration properties. The general advantages of viral vectors include high delivery efficiency and stable expression of the transgenes delivered. However, disadvantages such as immune response activation and limited packaging size may reduce transfection efficiency [40].
Lentiviruses are widely used for the delivery of CRISPR, as they possess a relatively large packaging capacity (6-9 kb), allowing efficient delivery of components such as SpCas9 [40]. Lentiviral vectors have been used in preclinical studies to deliver CRISPR–Cas9 for direct RNA targeting of *KRAS*, resulting in inhibited proliferation of cancer cells [19] [41], as well as for editing the BCR–ABL fusion in myeloid leukemia models, reducing tumorigenesis and restoring drug sensitivity [25]. These studies highlight the applicability of lentiviral delivery in cancer research and functional genomics.

Given the safety challenges associated with viral vectors and the limitations imposed by cargo size, non-viral delivery systems have gained significant interest, particularly for therapeutic genome editing [42]. Non-viral platforms offer simpler production, lack of genomic integration, and the ability to deliver nucleic acids (plasmid DNA or mRNA). Common non-viral strategies include direct injection of plasmid DNA or naked mRNA (RNA transfection) and lipid nanoparticles (LNPs). These approaches enable transient expression, which is especially beneficial for base editors that require tightly controlled activity to minimize off-target effects [39]. Nucleic acids encoding Cas9 or base editors and gRNAs can be delivered using lipid formulations, electroporation, or direct RNA

transfection. Direct RNA delivery (mRNA + synthetic gRNA) enables rapid onset of editing because transcription is not required.

However, this approach may require stabilization to prevent rapid degradation of RNA in the cytoplasm [42]. The reduced stability is cell-type dependent and can be problematic, often necessitating chemical modifications to maintain sufficient on-target activity. RNA delivery is particularly useful for base editors, where short-term expression is preferred [42]. Lipid nanoparticles (LNPs) are amphiphilic carriers composed of cationic lipids such as phospholipids or cholesterol. Because nucleic acids are highly anionic and cannot easily cross the cell membrane, LNPs facilitate efficient encapsulation and delivery of nucleic acids [43]. Their ability to protect and transport nucleic acids has made LNPs the most clinically advanced non-viral delivery system. LNP delivery of Cas9 mRNA and sgRNA to liver tissue for transthyretin (TTR) amyloidosis achieved efficient editing of the TTR gene and represents the first successful systemic CRISPR therapy in humans [44]. Ongoing studies aim to expand LNP targeting beyond the liver through the development of organ-specific LNP designs [45].

Table 1: **Comparison of Viral and Non-Viral Delivery Strategie.**

Delivering Strategy	Cargo Capacitiy	Advantages	Limitations
LentiviralVectors	∼6-9 kb	- High transduction efficiency - Infect dividing & non-dividing cells - Stable transgene expression - Relatively low immunogenicity compared to AAV and Adenoviruses	- Limited cargo size - Immunogenic [39] - Long-term Cas9 expression - Risk of random genomic integration
mRNA + gRNA (non-viral RNA Transfection)	No size limitation	- Time and resource effective, fast protein expression - Simple delivery of naked RNA possible - Delivery via LNPs and Electroporation possible - Transient activity of Cas9 reduces off-target risk - Not limited by cargo size	- Instability without chemical modification - Immunogenic [39]

3.9 Clinical and therapeutic Applications

CRISPR–Cas9 and base-editing technologies have become central tools for therapeutic genome modification, enabling both ex vivo and in vivo approaches for treating human diseases [46]. In ex vivo applications, patient-derived cells are edited outside the body and then reintroduced after editing and expansion.

One of the most advanced clinical applications of CRISPR is the treatment of genetic hemoglobinopathies, such as sickle cell disease (SCD) and transfusion-dependent β-thalassemia (TDT). CRISPR-based strategy involves reactivating fetal γ-globin (HBG) expression by disrupting the γ-globin repressor gene *BCL11A* efficiently worked. This is achieved by electroporating Cas9 ribonucleoproteins (RNPs) into hematopoietic stem cells ex vivo, enabling sustained induction of fetal hemoglobin and alleviating disease

symptoms once the edited cells are reinfused into the patient [47]. This therapeutic approach has already resulted in the first CRISPR-based gene therapy approved in Europe, the UK, and the United States, leading to the approval of the first-ever CRISPR medicine, Casgevy, as a curative treatment for SCD and TDT [48].
CRISPR technologies have also expanded into the development of chimeric antigen receptor (CAR) T cell therapies. CRISPR-edited allogeneic CAR-T cells derived from healthy donors allow more standardized production and potentially improved therapeutic performance. For example, knockout of exhaustion-inducing genes such as PDCD1 enhances T-cell persistence and reduces functional exhaustion [49]. Early clinical trials using multiplex-edited CAR-T cells have shown promising results, including the successful treatment of relapsed childhood T-cell leukemia using base-edited CAR-T cells [49].

In contrast to ex vivo editing approaches, in vivo genome editing delivers CRISPR components directly into patient tissues. The liver is one of the most clinically advanced targets, largely due to its efficient uptake of lipid nanoparticles (LNPs). In patients with transthyretin (TTR) amyloidosis, LNP-mediated delivery of Cas9 mRNA and sgRNA successfully disrupted the *TTR* gene in hepatocytes, leading to marked reductions in circulating TTR protein [44]. This represents the first CRISPR-based in vivo genome-editing therapy to reach Phase III clinical development [44]. Another emerging in vivo application, currently evaluated in a Phase I clinical trial, is a CRISPR-based therapy for familial hypercholesterolemia. Here, LNP-mediated delivery of adenine base editors (ABEs) is used to inactivate the PCSK9 gene, resulting in long-lasting reductions in low-density lipoprotein (LDL) cholesterol. LNPs have been specifically optimized to support efficient uptake even in patients with LDL receptor deficiencies [45].
Moreover, the world's first personalized in vivo CRISPR therapy was recently administered to a ten-month-old infant with CPS-1 deficiency. In this case, base editing corrected two pathogenic point mutations in the CPS1 gene directly in the liver, delivered by LNPs, leading to significant clinical improvement [46].
While these breakthroughs highlight the enormous therapeutic potential of CRISPR-based gene editing, it is important to note that no in vivo CRISPR therapy to date has directly targeted oncogenic mutations within solid tumors. Current clinical CRISPR interventions focus primarily on ex vivo editing of immune cells or in vivo targeting of monogenic liver diseases. Thus, unlike targeted therapies that act at the protein level and therefore remain vulnerable to resistance mechanisms, CRISPR technologies offer the possibility to intervene directly at the genomic origin of oncogenesis. This makes genome editing a fundamentally transformative approach for cancer therapy, capable of permanently correcting or disabling pathogenic mutations rather than inhibiting their consequences.
Together, these advances demonstrate how CRISPR–Cas9 and base editing technolo-

gies have rapidly transitioned from experimental genome engineering tools to clinically relevant therapeutic platforms with expanding potential, and I am absolutely eager to explore how we can adapt these systems to the benefit of lung cancer patients.

3.10 Aims of the Thesis

The major goal of this work is to explore CRISPR-based genome editing approaches as potential future therapeutics by the disruption or correction of key genetic alterations occurring in lung cancer and their functional analysis using patient-derived lung cancer organoids as a model system.
This thesis is organized into two major experimental projects:

3.10.1 Correcting *TP53* C275Y mutation and its functional analysis using adenine base editing

Since the tumor suppressor *TP53* is the most frequently mutated gene in human cancers and the functional consequences of many individual hotspot mutations remain incompletely understood, I aimed to correct the C275Y (G→A) mutation located within the *TP53* DNA-binding domain. The patient-derived organoid model isolated from a liver metastasis of a lung adenocarcinoma patient.
Therefore, I aimed to:

1. Apply the CRISPR-based adenine base editing (ABE) strategy in lung cancer organoids using NG-ABE8e in order to repair the TP53 C275Y G->A point mutation to the wild-type sequence. This included verifying the mutation site and designing high efficient gRNA with high on-target score and low off-target score.

2. Evaluate functional rescue of TP53 by assessing organoid survival and analyzing the editing consequences using flow-cytometry based quantification of edited cell viability. Editing efficiency was further examined by genotypic analyses, including genomic PCR and Sanger sequencing.

3.10.2 CRISPR–Cas9–based inactivation of the KIF5B–RET fusion oncogene

RET gene fusions are potential oncogenic drivers in NSCLC and represent important therapeutic targets. The organoid line used in this study harbors a KIF5B–RET fusion.
The aim of the second Project is to design CRISPR–Cas9 editing strategies to selectively disrupt the fusion gene using two approaches:

1. Breakpoint targeting with a single gRNA that cleaves directly at the fusion junction.

2. Dual-intron targeting with two gRNAs that cut within the introns of KIF5B and RET, deleting the intervening sequence. The dual-intron strategy tests the feasibility of fusion disruption independent of the exact breakpoint, offering the potential future advantage of applying the same approach across multiple patients without needing to sequence of each individual breakpoint.

And to explore Cas9 mRNA and gRNAs delivery into organoids via both viral (lentiviral) and non-viral (liposome based nanoparticle) methods to achieve editing. Assess editing consequences by evaluating cell viability, measuring editing efficiency, confirming fusion disruption using genomic PCR and Sanger sequencing.

By applying both viral and non-viral delivery methods in patient-derived organoids, we gain a comprehensive understanding of how CRISPR technologies can be used to develop a platform for functional studies of genetic alterations in additional lung cancer organoid lines. This platform could ultimately enable the creation of a systematic library of functional analyzes of potential oncogenic drivers in NSCLC, helping to decipher their biological roles and identify important mutations that could be therapeutically targeted in the future. This work establishes a framework for evaluating genome-editing of oncogenes in organoids as a clinically relevant model, enabling more precise therapeutic decisions in specific cases based on individual patients.

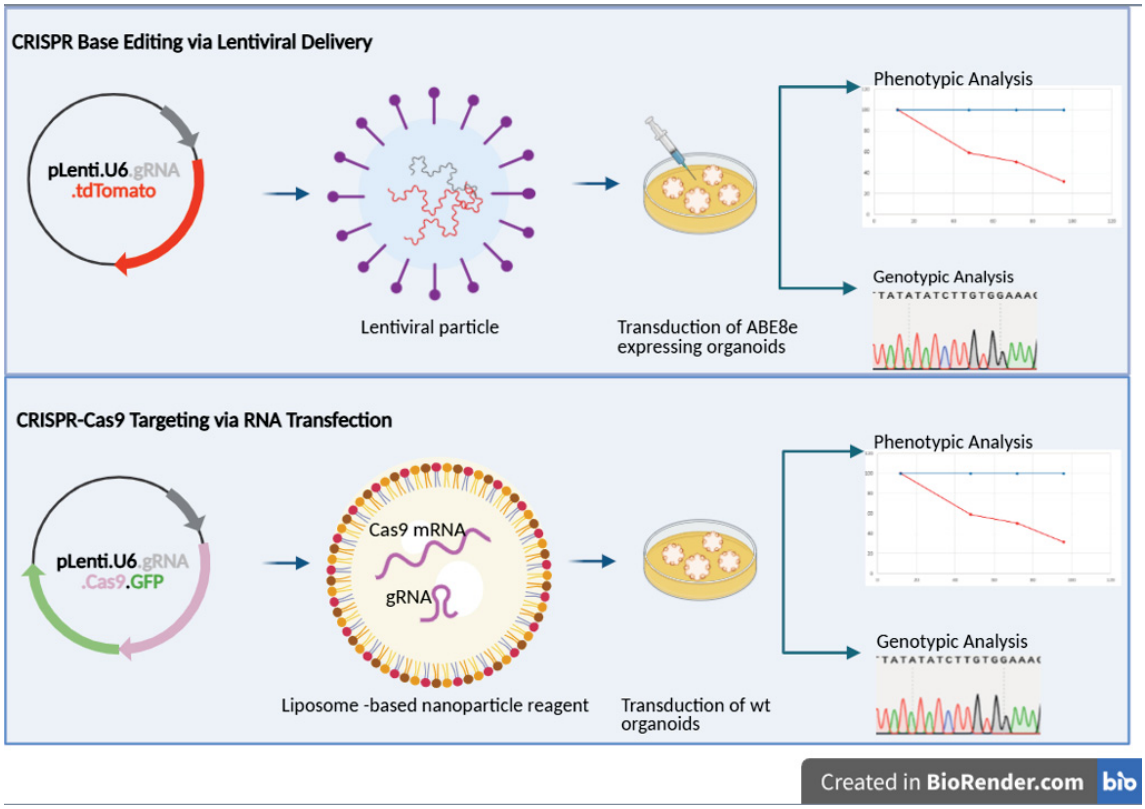

Figure 4: **Schematic workflow of the experiments.** Upper panel (Project 1): A lentiviral vector (pLenti U6 gRNA-tdTomato) is packaged into lentiviral particles, which transduce organoid cultures. Transduced organoids are subjected to phenotypic assays (flow cytometry quantification of tdTomato-positive cells) and genotypic analysis (Sanger sequencing).Lower panel (Project 2): A gRNA-Cas9 GFP expression cassette (pLenti U6 gRNA-Cas9 GFP) is complexed with a liposome based nanoparticle reagent and delivered as RNA to organoids by transfection. Edited cells are similarly evaluated by phenotypic readouts and by sequencing the fusion disruption locus via Sanger sequencing.

Genome editing technologies, CRISPR-Cas9 and base editors, require efficient delivery of the editing components into target organoids. Different delivery strategies can influence editing efficiency, specificity, and downstream validation. Figure (4) illustrates the two genome editing workflows I did in my thesis. In the first project, a lentiviral vector carrying a gRNA-tdTomato expression cassette is packaged into viral particles and used to transduce ABE8e-organoid line. In the second approach, a gRNA-Cas9-GFP cassette is delivered as RNA using lipid nanoparticles. Edited cells subsequently evaluated by phenotypic assays and sequencing. This comparison highlights the contrasting delivery modalities, viral versus non-viral I used in my projects.

4 Materials and Methods

4.1 Organoid Culture

The lung tumor organoids used in this study were created from patient-derived primary tissue. A biopsy was taken from a liver metastasis of an adenocarcinoma in a 55-year-old female patient. The patient-derived biopsy received the Preclinical Model Unit sample ID 315 (PMU315).

Patient tumor specimens were washed with Biobank Medium in a petri dish and then mechanically cut into small pieces (2–3 mm). These were transferred into a digestion mix made of (dispase II (2.5 mg/mL), collagenase D (2.5 mg/mL), DNase (25 µL), and Y-27632 (5 µL) in 5 mL Biobank Medium. The Biobank Medium is made of 500 mL F+++ Medium and 1 mL Primocin. The tissue was chopped again into smaller pieces with scissors. Then, 2.5 mL Biobank Medium was added. The digestion mix was incubated at 37°C for 45–60 min with rotation. After digestion, the supernatant was passed through a 70 µm cell strainer into a 50 mL falcon tube. The suspension was centrifuged at 300 x g and 4°C for 5 min and the pellet was resuspended in 2 mL red blood cell lysis buffer and incubated for 2–5 min at room temperature. The reaction was stopped by adding PBS and the sample was centrifuged again and the cell pellet was resuspended in Matrigel (depending on pellet size; generally, 20 µL Matrigel/well is used). After seeding the organoids the plate was placed in the incubator for 20 min at 37°C. After polymerization of the Matrigel, 250 µL of Lung Tumor Medium was added to each well. The lung tumor organoids were grown in the incubator at 37°C, 95% humidity, and 5% CO_2.

Establishing the patient-derived adenocarcinoma tumor organoids was successful. Below is a histological image of the PMU315 lung tumor organoids with the passage number 20 stained with hematoxylin and eosin (H&E). Hematoxylin stains the nuclei dark purple, which appear as the round, densely colored structures, while eosin stains the cytoplasm and extracellular matrix light pink. The cells are arranged in spherical and irregular clusters, a common morphology in 3D organoid cultures. Many nuclei appear hyperchromatic and pleomorphic, which is typical of malignant cells. The pale areas between the clusters represent matrix or empty spaces where the organoids were embedded in Matrigel during culture.

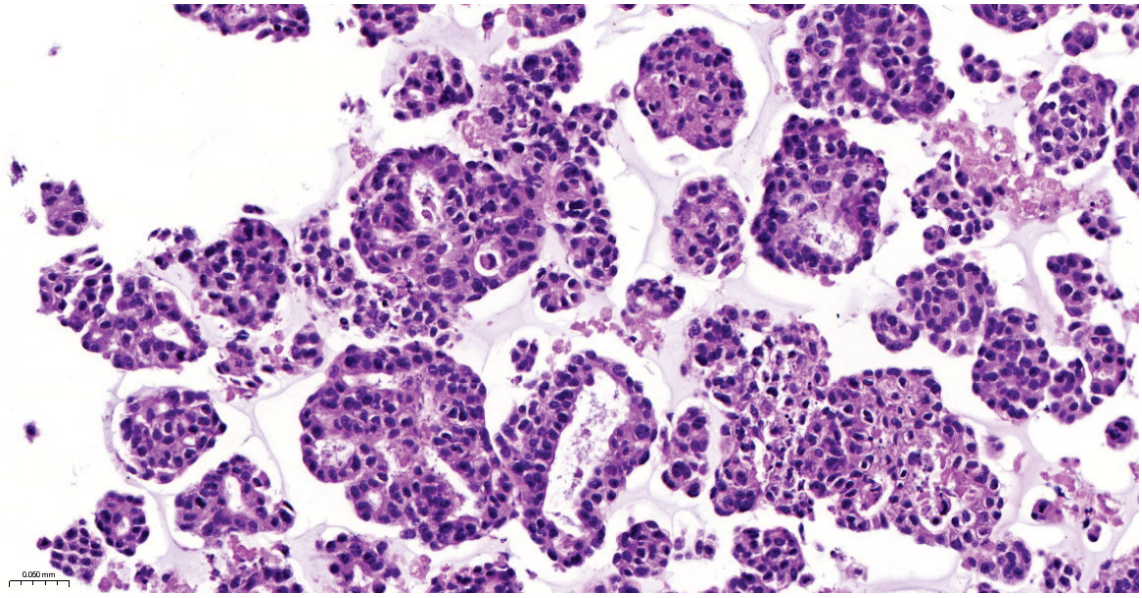

Figure 5: PMU315 organoids stained with hematoxylin and eosin

4.2 Genotyping of PMU315 *TP53* exon8

Organoids were mechanically disrupted and genomic DNA was isolated using QIAamp® DNA Blood Mini kit, the isolation was done according to manufacturer's instructions. Briefly, 20µl proteases were added to organoids in their 200 µl lung tumor medium and 200µl lysis buffer was added. The mixture was heated at 56°C for 10 min and centrifugatiion and washing steps were followed according to manufacturer's instructions.
The genomic DNA (with a concentration 50-180 ng/µl) was used as a template for PCR analysis. PCR amplification of Exon8 of TP53 was performed using high-fidelity Phusion polymerase using the following protocol (Table 2). The primers used were designed around the Exone 8 and codon C275 of TP53 (Table 3).

Table 2: **Protocol of Phusion PCR.**

Component	1x Reaction
5X Phusion HF or GC Buffer	10 μl
10 μM (Forward Primer TP53 367)	2.5 μl
10 μM (Reverse Primer TP53 368)	2.5 μl
10 mM dNTPs	1 μl
Template DNA	variable
Nuclease-free water	to 50 μl
Phusion DNA Polymerase	0.5 μl
Total Volume	50 μl

Table 3: **Primers for *TP53* exon8 Amplification.**

Order Number	Primer Name	Primer Sequence
367	TP53-Fwd1	CTTCTTTGGCTGGGGAGAGG
368	TP53-Rev1	CACCTCTCATCACATCCCCG

10 µl of each PCR product was assessed on an 2% agarose gel to verify that the primers amplified the expected targets and confirm correctly sized bands. To determine the size of the bands, 1 kb Plus DNA Ladder (NEB) and 6x Orange DNA Loading Dye (NEB) were used. The PCR products were then purified using the Bioline kit following the manufacturer's instructions. DNA concentrations were measured using a Nanodrop spectrophotometer. The purified DNA, along with the primers 367 and 368 were subsequently submitted for Sanger sequencing. DNA samples for Sanger sequencing were run by Microsynth Seqlab GmbH (Göttingen, Germany)[50].

4.3 Genotyping of PMU315 KIF5B-RET fusion breakpoint site

Same procedure as in the previous section were applied in order to isolate gDNA and to amplify the predicted KIF5B-RET Fusion breakpoint. Because the exact breakpoint was unknown, several primer pairs were designed and tested (Table 5). PCR amplification of the KIF5B and RET regions of inter-est was carried out with a Herculase II polymerase using the following protocol (Table 4) and using multiple primers positioned around the predicted breakpoint within KIF5B and RET introns.

Table 4: **Protocol of Herculase II PCR.**

Component	1x Reaction
5X Herculase II reaction Buffer	10 μl
10 μM Forward Primer	1.25 μl
10 μM Reverse Primer	1.25 μl
100mM dNTP mix	0.5 μl
Nuclease-free water	to 50 μl
Template DNA	variable
Taq Polymerase	1 μl
Total Volume	50

Table 5: **Primers for *KIF5B-RET* breakpoint validation.**

Order Number	Primer Sequence	Annealing Temperature	Extention Time
P31	TGTTTTGGGTTCTCTTAGGCA	50°C	2.5
P33	GGCAGGTACCTTTCAGCATCT	50°C	2.5
P32	CAACTTTAGCGAGTATAGATGCTGA	50°C	2.5
P34	ACCTTTCAGCATCTTCACGG	50°C	2.5
P5	CTCATTTCAGTGCTGTGGGC	53°C	4
P18	CTCCAACTCTACTGGTGCCG	53°C	4
P7	GGTTTCCTGCCCCTATGAGT	53°C	3
P20	CCTCTAAACTCACCCAGCCC	53°C	3

The primer have been designed around the predicted breakpoint site of the KIF5B intron 15 and RET intron 11 (Fig. 21). 10μl of each PCR product was assessed on an 2% agarose gel to verify that the primers amplified the expected targets. To determine the size of the bands, 1 kb Plus DNA Ladder (NEB) and 6x Orange DNA Loading Dye (NEB) were used. The PCR products were then purified using the Bioline Kit following the manufacturer's instructions. DNA concentrations were meas-ured using a Nanodrop spectrophotometer. The purified DNA, along with the used primers were subsequently submitted for Sanger sequencing. DNA samples for Sanger sequencing were run by Microsynth Seqlab GmbH (Göttingen, Germany)[[50]].

4.4 Primer Design for Validating the KIF5B:RET Fusion Breakpoint

The resulting chimeric mRNA is predicted to connect exon 15 of KIF5B directly to exon 12 of RET. Deep RNA Sequencing analysis performed by our collaborators at the NCT, Dresden, shows that the breakpoint between exons based on Exome sequencing data which reflects the transcript-level fusion, not the genomic-level rearrangement (Fig. 21). The sequence of the following regions have been imported from the Genome Browser UCSC (https://genome.ucsc.edu/): exon14-intron14-exon15-intron15 of *KIF5B* and exon11-intron11-exon12-intron12-exon13 of *RET*. I designed multiple primers after determining the correct orientation for each. For example, in KIF5B, the translocated sequence at the 5'-end is flipped, so the primer must be in the 5' to 3' direction, starting with exon 14, in case the fusion junction occurs before exon 5. For each primer I identified a small sequence 18–24 base pairs (bp) long and have 40–60% GC content. To locate the suitable place for the reverse primer a space inbetween should be 1kb-1.3kb downstream of the forward primer. To ensure highquality sequencing data for the protospacer region, the primers should be at least 100 bp away from the target sequence. The primers can be analyzed using the software tools IDT and Primer3Plus (https://www.primer3plus.com/index.html).

4.5 Design of small guide RNA (sgRNA)

A Single guide RNA (sgRNA) can direct the Cas9 protein to a specific site in the genome, and designing efficient and specific sgRNAs against these mutations is therefore a critical step. sgRNA design tools for generating a knockout or edited gene sequence have greatly improved in the past few years. I used the UCSC Genome Browser to import the target sequence. SnapGene software was used as the sequence-viewing software of choice. I annotated the mutation and identified PAM sequences downstream of the mutation. I identified a 20 bp sequence (gRNA also called spacer) upstream of the PAM and without including the PAM. I used the online tools IDT (https://eu.idtdna.com/page/tools), CasOFFinder (http://www.rgenome.net/cas-offinder/), and CCTop (Stemmer et al., 2015; https://cctop.cos.uni-heidelberg.de), and cross-checked the results through a combination of all of them in order to assess the efficiency and off-target effects of the gRNAs. These tools have been instrumental in planning a gene knockout experiment, and in our case targeting the KIF5B-RET oncogene. However, in the other project of my thesis we used a base-editing approach targeting the point mutation TP53 C275Y. All sgRNAs used for this project were manually designed to place the mutant base within the editing window (4–8 nt) and upstream of an NG PAM. The target effi-ciency and potential off-target effects were checked using the above-mentioned software tools. The manually designed gRNAs were checked for their targeting efficiency and off-target potential. The best predicted candidates were then nominated and shortlisted. After selecting the gRNAs, they must be cloned into lentiviral vectors. We utilized common restriction sites, specifically BbsI and BsmBI, for this purpose. The design process involved the following steps:

1. Top Oligo Design: The top oligo was designed with the sequence 5'-CACC[spacer sequence]-3'.

2. Bottom Oligo Design: The bottom primer oligo was designed with the sequence 5'-AAAC[reverse complement of spacer sequence]-3'.

These oligos were engineered to contain complementary overhangs that facilitate cloning using the BbsI and BsmBI restriction sites.

4.6 gRNAs Cloning into Lentiviral Vectors

For the expression of Cas9 and sgRNAs from lentiviral vectors, we cloned the designed complementary oligonucleotides into pL-CRISPR.EFS.GFP (Addgene #57818) (Fig. S3). In cases where the protospacer did not begin with a guanine, a guanine was added to the 5'-end of the protospacer before cloning to boost the expression of the gRNA from the human U6 promoter. The same procedure was followed for the ABE8e

base editing experiment. Protospacers were cloned into the LRT2B vector (Addgene plasmid #110854) (Fig. S4) using BsmBI/BbsI sites, following the standard protocol [[51]]. The cloning protocol include the following steps:

4.6.1 Oligos Annealing

For cloning all lentiviral vectors, the first step was annealing the oligos. The oligos for gRNA were annealed in a 10 μl reaction containing 1 μl of each sgRNA oligo (100 μM), 1 μl of 10X T4 ligation buffer, and 0.5 μl of polynucleotide kinase. The reaction was run in a thermocycler at 37°C for 30 minutes, followed by 95°C for 5 minutes, and then slowly brought down to 25°C.

4.6.2 Restriction/Ligation Golden Gate

The reaction was then diluted 250 times in water, and 2 μl was used for the digestion/ligation reaction. In this reaction, 100 ng of the backbone plasmid (e.g., pLCRISPR.EFS.GFP) was added to the annealed oligos, along with 2 μl of Tango buffer, 1 μl of 10 mM DTT, 1 μl of BsmBI/BbsI, and 0.5 μl of T4 DNA ligase, resulting in a final reaction volume of 20 μl. To digest the vector and ligate the oligos into it, the following temperature profile was repeated six times in the thermocycler: 37°C for 5 minutes and 23°C for 5 minutes.

4.6.3 Bacterial Transformation

2 μl of the ligated product was transformed into competent E. coli cells (XL1-blue). We plated 50 μl of the cells on an agar plate containing 100 μg/mL ampicillin and left them to grow overnight at 37°C. The next day, colony PCR was performed using isolated and purified plasmid DNA, following the manufacturer's instructions for the Thermo Fisher GeneJET Plasmid Mini-prep. The PCR was conducted with MyTaq Red Polymerase according to the manufacturer's instructions. DNA concentration was measured using a Nanodrop, and an aliquot of the amplicon was run on a 1.5% agarose gel alongside a 100 bp DNA ladder to check the quality of the PCR. Plasmids were sequenced through the sequencing service provider Microsynth Seqlab GmbH (Göttingen, Germany) using the forward primer for the U6 promoter: 5'- GAGGGCCTATTTCCCATGATCC-3'.

4.7 Cloning of Adenine Base Editor into Lentiviral Vector

To deliver the ABE into the cells, a lentiviral vector, pLenti-NGABE8e-P2A-GFP-PGK-PuroR, was established and optimized in the Buchholz lab (Addgene #242000) (Fig. S2) [19]. The NG-ABE8e plasmid (Addgene #138491) was cloned into the lentiviral vector using the pLenti-FNLS-P2A-GFP-PGK-Puro backbone (Addgene #110869), re-

ferred to as the pL-Backbone, and the pLenti-NGABE8e-P2A-GFP-PGK-PuroR (Fig. S2) construct was generated.

4.8 Cell Culture

Cell line used in order to produce virus is modified human embryonic kidney cell line (HEK293T), the cells were kept at 37°C, 5% CO2 and cultured in following media: Dulbecco's modified Eagle's medium DMEM (high glucose, GlutaMAX™, Invitrogen, Carlsbad, CA). All of the media were supplemented with 10% fetal bovine serum (FBS, Gibco) and 1% Penicillin-Streptomycin (Gibco). After thawing, the cells were given two passages to recover before experiments were initiated. Most of the cell lines dis-played similar doubling times and were typically maintained on a 2–3-day passaging schedule. The day before transfection, HEK293T cells were plated to ensure they reached an appropriate confluency for the procedure in the format: T-175 flask: 15–20 million cells (in 20 mL Full medium).

4.9 Lentivirus Production

Before transfection of the HEK293T cells, the flask were at 80% confluence. To prepare the plasmid transfection solution for one T175 flask, we prepared the following mixture:

1. 10 μg transfer vector (e.g., pL-CRISPR.EFS.GFP.gRNA, Addgene plasmid #57818),
2. 6 μg psPAX2 (Addgene plasmid #12260), and
3. 2 μg pMD2.G (Addgene plasmid #12259).

psPAX2 and pMD2.G express packaging signals for virus assembling. These components were combined and brought to a total volume of 1 mL using DMEM media without FBS or antibiotics. In a separate tube, we diluted 45 μL polyethylenimine (PEI) stock (1 mg/mL) in 955 μL blank medium. The PEI solution was added to the plasmid mixture. Then, 4 mL of DMEM was added to the transfection mixture. The transfection was incubated for 20 hours. If the transfer vector expresses a fluorescent protein, transfection efficiency can be assessed by monitoring the percentage of fluorescent-positive HEK293T cells. After 48 hours, we collected the supernatant and centrifuged it for 2 h at 100,000 g in a sterile Tube compatible with an ultracentrifuge rotor (e.g., JS-24.38, Beckman Coulter). The tubes containing the virus were placed into aluminum swinging buckets and balanced to the nearest 0.01 g. After centrifugation (2 h, 100,000 g, slow acceleration/deceleration, 4°C), the supernatant was carefully decanted, and 300 μL PBS was added to resuspend the viral pellet. The virus was aliquoted in 50 μL portions into labeled cryovials and stored at –80°C.

4.10 Transduction of Lung Organoids

Lung organoids (PMU315) were collected from Matrigel and dissociated mechanically and chemically. Organoids from 3-4 wells were pooled, washed with F+++ medium, and dissociated using narrowed glass pipettes. After centrifugation, pellets were resuspended in TrypLE Express, transferred to a pre-warmed 48-well plate, and incubated at 37 °C for maximum 2 minutes until single cell suspensions were obtained. TrypLE activity was stopped with F+++ medium, and cells were centrifuged and resuspended in lung tumor medium supplemented with ROCK inhibitor (Y-27632).
For transduction, lentiviral vectors (e.g., pLenti-U6-gRNA1-tdTomato-p2A-BlasR and controls) were prepared with protamine sulfate (into 1:1000 final concentration). First I diluted protamine sulfate 1:10 into F+++ medium and then another 1:10 in a final volume of 800µl. 200µl of Virus mixture were added to 600 µl single-cell suspensions. The plates were centrifuged at 700 g for 1 h before incubation for 4–5 h at 37 °C. Cells were then collected, washed, pelleted, and embedded in Matrigel (20 µL per well). Organoids were seeded in four replicate wells per condition and overlaid with lung tumor medium containing ROCK inhibitor.

4.11 Flow Cytometry Analysis

After transduction, organoids were further cultured and analyzed to assess the infection rate and to compare the viability of non-infected and infected cells. Transduced cells were analyzed by flow cytometry using the MACSQuant VYB Analyzer (Miltenyi Biotec) and FlowJo software for fluorescent marker expression (either GFP or tdTomato). A reduction in the percentage of GFP/tdTomato-positive cells indicates that the infected cells expressing the nuclease-sgRNA complex have a growth disadvantage compared to non-infected cells.
The organoids were transduced in 48-well plates and kept in a 37°C incubator. Several hours or days after transduction, the organoids were washed, and fresh medium was added. For flow cytometry quantification, organoids from one well were dissociated using narrowed glass pipettes. After centrifugation, the pellet was resuspended in 100 µL F+++, of which 50 µL was used for FACS acquisition. The remaining volume was used for gDNA isolation. The 50 µL used for FACS was mixed with TrypLE Express, transferred to a pre-warmed 48-well plate, and incubated at 37°C for a maximum of 2 minutes until single-cell suspensions were obtained. TrypLE activity was stopped with F+++ medium, and the cells were centrifuged, pellet was resuspended in 400 µL FACS buffer and split into two FACS tubes for duplicate measurement. For fluorescence detection, when individual cells pass through a laser beam, they scatter light that is detected by two optical detectors. Forward scatter (FSC), measured along the path of the laser, provides information about cell size. Side scatter (SSC), measured

at a 90° angle to the laser, provides information about the internal complexity (granularity) of the cell. Together, these two parameters provide a strong basis for analyzing the fluorescent-postive-cell population and determining viability and live cell numbers within the sample.

4.12 EditR to quantify base editing efficiency

After isolating gDNA from the organoids, amplifying, and Sanger sequencing the target region, I measured the base editing efficiency after transducing the organoids with pLenti-U6-gRNA1-tdTomato-p2A-BlasR. To quantify the editing efficiency in the treated organoids, I used the online software EditR (https://moriaritylab.shinyapps.io/editr_v10/). I uploaded the tool's required input files, including the .ab1 Sanger sequencing file of the potentially edited region and the 20 bp gRNA sequence.
EditR provides a plot displaying the editing efficiency at each base within the gRNA. It shows the protospacer chromatogram peak areas for each nucleotide along with an underlying box plot that determine whether base editing has occurred. The underlying plot consists of four individual boxes, one for each base. If one or more of these boxes are colored, they represent base reads that are considered significant, meaning that if multiple colored tiles appear under a single base call, base editing likely occurred. For example, an "editing efficiency of 60%" indicates that 60% of all analyzed cells carry a successful edit at the target base "A," which is reflected by overlapping chromatogram peaks at the edited nucleotide.

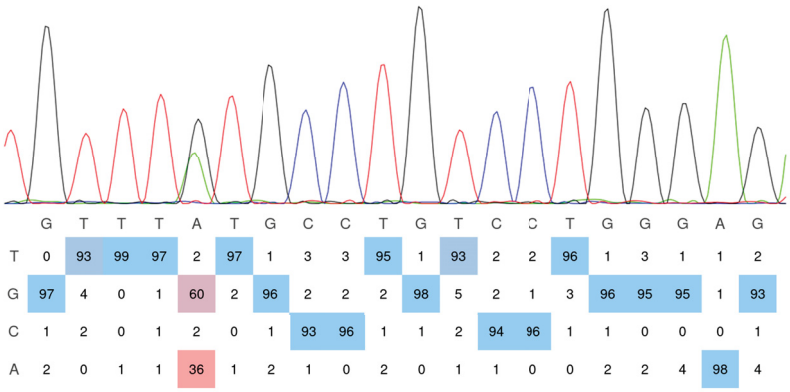

Figure 6: **Example output from the EditR analysis.** The upper plot displays Sanger sequencing chromatogram for the target protospacer region. Each tile represents the percentage contribution of a given nucleotide at each position. Blue tiles correspond to predominant unedited bases, while red tiles indicate significant edited base signals detected above background. This output is used to calculate the editing efficiency at the target nucleotide following organoid transduction with base editors.

4.13 Materials, Equipments and Medias

4.13.1 Reagents and Kits

- MyTaq DNA polymerase with 5x MyTaq buffer (Bioline, BIO-21105)
- Phusion High Fidelity DNA Polymerase with 5x Phusion HF Reaction Buffer (NEB, M0530S)
- MyTaq DNA polymerase with 5x MyTaq buffer (Bioline, BIO-21105)
- Phusion High Fidelity DNA Polymerase with 5x Phusion HF Reaction Buffer (NEB, M0530S)
- dNTP solution mix, 25 mM each (Enzymatics, cat. no. N205L)
- 1-kb Plus DNA ladder (Life Technologies, cat. no. 10787-018)
- Gel Loading Dye, Purple (6x) (New England BioLabs, cat. no. B7024S)
- BsmBI (New England BioLabs, cat. no. R0580S)
- BbsI (NEB)
- 10x Tango buffer (Thermo Scientific, cat. no. BY5)
- DTT (Thermo Scientific, cat. no. R0862)
- RedSafe Nucleic Acid Staining Solution (intron Biotechnology)
- T4 DNA ligase with 10x ligation buffer (New England BioLabs, cat. no. B0202S
- T4 polynucleotide kinase (New England BioLabs, cat. no. M0201S)
- Stbl3 chemically competent E. coli (Life Technologies, cat. no. C7373-03)
- Ampicillin, 100 mg ml - 1, sterile filtered (Sigma, cat. no. A5354)
- Bioline PCR Purification Kit (BIO-52060)
- QIAprep Spin Miniprep Kit (Qiagen 27106)
- QIAGEN-tip 20 Maxiprep Kit (Qiagen 10023)
- QIAquick gel extraction kit (Qiagen, cat. no. 28704)
- QIAamp® DNA Blood Mini kit (Qiagen, 51104)
- NEBridge Golden Gate Assembly Kit
- Bovine Serum Albumin (BSA) (NEB)
- Normal Agarose (Invitrogen)

4.13.2 Materials for Cell and Organoid Culture

- HEK 293T cells (Life Technologies, cat. no. R700-07)
- PANC-1 were a kind gift from Max Heiduk, Seifert AG, Department of Surgery at the Univeristy Hospital Carl Gustav Carus Dresden
- DMEM, Glutamax (Life Technologies, cat. no. GIBCO 10829018)
- Fetal Bovine Serum (Invitrogen 10108165)
- 0.05% Trypsin–EDTA (GIBCO 25300054).

- Penicillin-streptomycin, 100x (GIBCO 15070063)
- Protamine sulfate (Sigma-Aldrich)
- Puromycin dihydrochloride (Life Technologies, cat. no. A11138-03)
- Amicon® Ultra-15 Centrifugal Filter Devices (Merck Millipore)
- Filtropur S 0.45 m (Sarstedt)
- Open-Top Thickwall Polycarbonate Tube (Beckman Coulter)
- Falcon tubes, polypropylene, 15 ml (BD Falcon, cat. no. 35209)
- Falcon tubes, polypropylene, 50 ml (BD Falcon, cat. no. 352070)

4.13.3 Equipments

- Thermocycler with programmable temperature stepping functionality.
- UV spectrophotometer (NanoDrop 2000c, Thermo Scientific).
- Desktop microcentrifuges (e.g., Eppendorf, cat. nos. 5424 and 5804). Centrifuge (Eppendorf 5810).
- MACSQuant® VYB (Miltenyi Biotec, Bergisch Gladbach, Germany)
- Odyssey® CLx Imaging System (Li-cor Biosciences GmbH, Bad Homburg von der Höhe, Germany)
- Avanti JXN-30 centrifuge (Beckman Coulter).
- FlowJo™ Software FlowJo, LLC, Ashland, Oregon, United States.
- Avanti JS-24.38 swinging-bucket rotor (Beckman Coulter).

4.13.4 Media and solutions for organoid culture

Table 6: F+++ Medium

Supplement	**Amount**
Advanced DMEM/F12	500 mL
GlutaMAX	5 mL
HEPES	5 mL
Penicillin-Streptomycin	5 mL

Table 7: Biobank-Medium

Supplement	**Amount**
+++ Medium	500 mL
Primocin	1 mL

Table 8: Medium for Human Lung Tumor and Normal Tissue

Supplement	**Amount**
Biobank-Medium	48097 mL
B27*	1000 mL
Noggin	50 mL
A83-01	10 mL
Nicotinamid	500 mL
N-Acetyl-Cystein	125 mL
FGF10	10 mL
FGF7	100 mL
SB202190	8 mL
Rspondin	50 mL
Y-27632	50 mL

Table 9: Digestion-Mix Lung Normal Tissue und Lung Tumour Tissue

Supplement	**Amount**
Biobank-Medium	5 mL
Collagenase D	2,5 mg
Dispase II	2,5 mg
DNAse	25 μL
Y-27632	5 μL

Table 10: Bacterial media recipe with Lysogeny broth (LB-Lennox version)

Supplement	**Amount**
Bacto tryptone	10 g
Yeast extract	5 g
NaCl	5 g

Bacterial media: For total volume of 1000 ml, all components were dissolved in distilled water and the pH was adjusted to using NaOH to 7.5, or adjusted to 8 for LS-LB. The volume was the filed up to 1000 ml and the medium was autoclaved for 20 min at 121°C before using it in cell culture. Medium was supplemented with am-picillin with a concentration of 100 μg/ml.

Table 11: 10X Phosphate Buffered Saline (10X PBS)

Supplement	**Amount**
43 mM Na2HPO4 (Na2HPO4H2O; MW = 178.0 g/mol)	7.6 g
14 mM KH2PO4 (MW = 136.1 g/mol)	1.9 g
27 mM KCl (MW = 74.6 g/mol)	2.0 g
1.47 M NaCl (MW = 58.4 g/mol)	85.9 g

Phosphate Buffered Saline (10X PBS): All components were dissolved in distilled water for a total volume of 1000 ml. The pH of this solution was adjusted to 7.4 and the solution was autoclaved for 20 min at 121°C before using it for cell culture work.

5 Results

5.1 Correcting *TP53* C275Y Mutation in Patient-Derived Lung Cancer Organoids

Since tumors harboring *TP53* point mutations are difficult to target using conventional therapeutic approaches [9], we aim to explore genetic correction strategies as a permanent and more precise strategy to restore *TP53* function in cancer cells. Genome editing using CRISPR-Cas9 nucleases is not suitable for correcting such mutations, as DSBs followed by error-prone repair mechanisms are unlikely to restore the wild-type sequence of tumor suppressor genes. In contrast, CRISPR-nCas9-based base editors enable precise single nucleotide conversions without inducing DSBs. Previous work in our laboratory has demonstrated that applying such base-editing systems can correct *TP53* point mutations and restore p53 functionality in cancer cell lines [19] [20].
Therefore, we decided to apply the CRISPR-nCas9 base editing approach in order to correct the *TP53* C275Y (G→A) mutation in patient-derived organoids of lung cancer and to characterize the biological function of this point mutation. We hypothesized that restoring wild type *TP53* function would suppress tumor growth and lead to a reduction in the cancer cell population due to reactivation of p53-mediated tumor suppressor pathways.

To test this hypothesis, I first needed to confirm the presence of the *TP53* C275Y mutation in the patient-derived lung organoids PMU315. Subsequently, I generated organoid lines expressing the NG-ABE8e base editor and GFP via lentiviral transduction with the construct pLenti-NGCas9ABE8e-GFP-Puro (pL-NG-ABE8e). Finally, we cloned each candidate guide RNA targeting the TP53 C275Y (C275Y-gRNA) site into a tdTomato-expressing lentiviral vector (pLenti-C275YsgRNA-tdTomato) for delivering gRNA and *tdTomato* into the mutant organoids.

5.1.1 Confirmation of the *TP53* C275Y Mutation in the PMU315 Lung Cancer Organoid Line

To validate the presence of the *TP53* C275Y mutation located in exon 8, organoid cells from the patient-derived line PMU315 were collected and genomic DNA was extracted. The region encompassing exon 8 of *TP53* was amplified by PCR, and the purified PCR product was subsequently analyzed by Sanger sequencing. Sanger sequencing chromatograms were visualized and analyzed using SnapGene software. The resulting sequence aligned perfectly with the reference *TP53* wildtype sequence, except for a single base substitution (G→A) at position c.824 (Fig. 7).

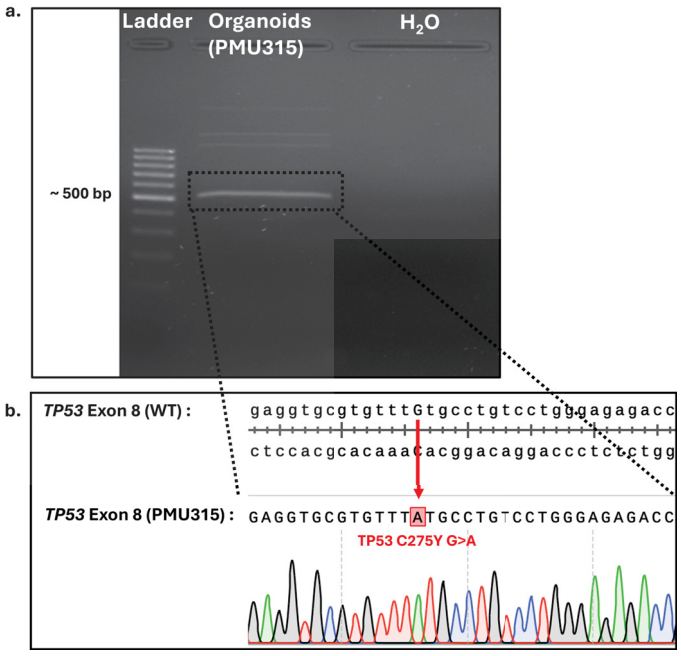

Figure 7: **Validation of the *TP53* C275Y (G→A) mutation in PMU315 lung cancer organoids. a.** Agarose gel electrophoresis showing PCR amplification of TP53 exon 8 from gDNA of the PMU315 organoid line. A clear band of the expected size (~504 bp) was observed in the TP53 lane, confirming successful amplification. The control (H_2O) showed no amplification, indicating the absence of contamination. A 100 bp DNA GeneRuler ladder was used as a size reference. **b.** Sanger sequencing chromatogram showing the upper sequence corresponding to the wild-type region of *TP53* exon 8, and the lower sequence derived from PMU315 lung cancer organoids. A point mutation (c.824 G→A, resulting in p.C275Y) is visible in exon 8. The mutated base is highlighted by a red box and arrow, indicating a G→A substitution.

This confirmed that the PMU315 organoid line harbors a point mutation in *TP53* (c.824 G>A, resulting in p.C275Y) within exon 8, a region known to represent a hotspot for inactivating mutations [14]. This point mutation likely disrupts p53 function, and its correction may be sufficient to restore wild-type activity and potentially terminate the tumorigenic phenotype. Since I can identify two NG-PAM sequences close to the muta-

tion site (dotted green boxes) and absence of NGG PAMs (Fig. 8), the NG-ABE8e base editor was chosen, as it recognizes NG PAMs rather than the NGG motif. To achieve a precise correction of the *TP53* C275Y mutation, two candidate gRNAs (shown in green) were designed to position the target adenine (A) within the predicted editing window of the NG-ABE8e base editor, which typically spans 13–18 nucleotides upstream of the PAM site (shown in blue). Based on these findings, we subsequently generated organoid line PMU315 expressing the NG-ABE8e base editor via lentiviral transduction with pL-ABE8e.

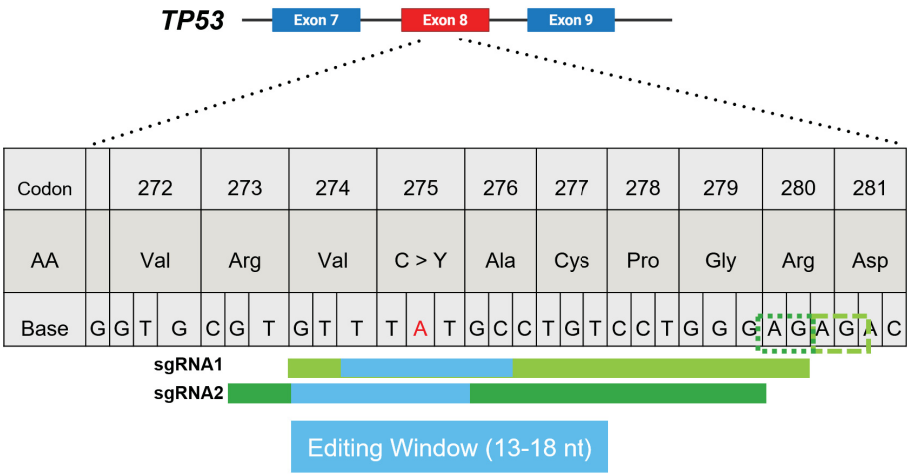

Figure 8: **Schematic of *TP53* C275Y Mutation Site and sgRNA Design** Illustration highlighting the position of exon 8, where the *TP53* C275Y (c.824 G→A) mutation is located. The codon and corresponding amino acid sequence surrounding the mutation site are shown. The G→A substitution (red letter) results in a cysteine-to-tyrosine (C→Y) change at codon 275. Two NG PAM sequences"AG" are highlighted with dotted green boxes. The position of the PAM sequences have facilitated the selection of the NG-ABE8e base editor. Two gRNAs (sgRNA1 and sgRNA2) were designed to place the target adenine within the predicted ABE8e editing window, which spans 13–18 nucleotides upstream of the PAM site (indicated by blue boxes).

5.1.2 Generation of Lung Cancer Organoid Line Expressing NG-ABE8e Base Editor

To enable precise correction of the TP53 C275Y point mutation using CRISPR base editing, it was necessary to establish an organoid line expressing an adenine base editor (ABE-line). Because the target mutation is located near two suitable “NG” PAM site, we selected the NG-ABE8e base editor, which offers an optimal editing window spanning approximately 13–18 nucleotides upstream of the PAM sequence (Fig. 8). To generate the ABE-line, wild-type PMU315 lung cancer organoids were transduced with a lentiviral vector carrying the pLenti-NGCas9ABE8e-P2A-GFP-PGK-PuroR construct (pL-ABE8e). Successful transduction was expected to result in GFP fluorescent cells. At six

days after infection (6 dpi), flow cytometric analysis revealed that approximately 35.5% of the cells were GFP-positive, indicating stable expression of the NG-ABE8e base editor (Fig. 9).

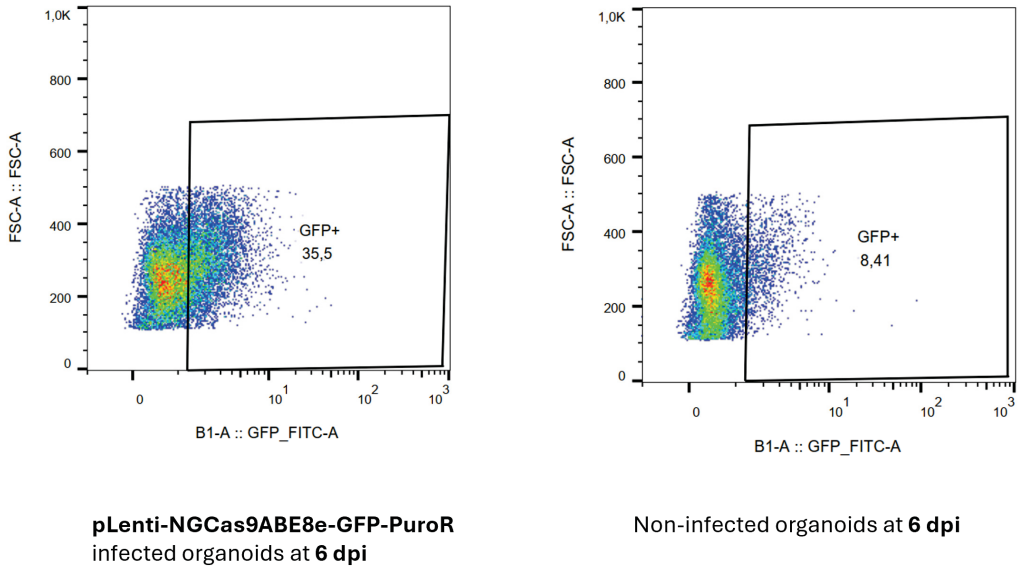

Figure 9: **Flow cytometric Plots of GFP-positive cells infected with pL-ABE8e.** FACS plot showing 35.5% GFP-positive cells in PMU315 organoids 6 days after lentiviral transduction with the pLenti-NGCas9ABE8e-P2A-GFP-PGK-PuroR construct, compared to 8% background signal in the non-infected control. This infection efficiency was sufficient to proceed with puromycin selection of organoids harboring the construct

For the selection of successfully transduced cells, we utilized the puromycin resistance gene encoded in the same lentiviral construct. To determine the minimal effective puromycin concentration that efficiently eliminates wilt-type organoids, a puromycin kill curve assay was performed. PMU315 Organoids were treated with increasing puromycin concentrations, 0.1, 0.5, 1, 1.5, 2, 2.5, and 3 $\mu g/\mu l$. Based on these results, a concentration of 0.5 $\mu g/\mu l$ was identified as the lowest dose at which wild-type organoids were all eradicated. This concentration was therefore subsequently used to select for NG-ABE8e-expressing cells.

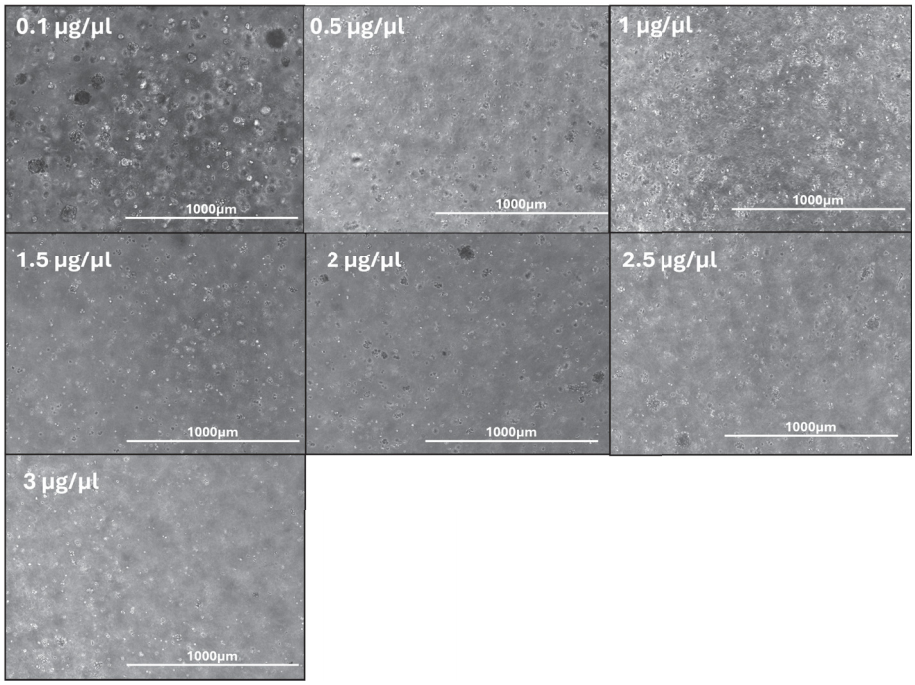

Figure 10: **Puromycin kill curve of wild-type PMU315 lung cancer organoids.** Microscopic images of wild-type PMU315 organoids treated with increasing concentrations of puromycin (0.1–3 $\mu g/\mu l$) for 6 days. Organoid number progressively decreased with increasing puromycin concentration. Complete organoid death observed at **0.5 $\mu g/\mu l$** and higher. Based on these results, 0.5 $\mu g/\mu l$ puromycin was selected as the optimal minimum concentration for subsequent selection of successfully transduced organoids. Scale bar = 1000 μm.

After determining the minimum efficient puromycin concentration to be 0.5 $\mu g/\mu l$, this concentration was applied to the pL-ABE8e-transduced organoids in order to selectively enrich for the 37% of organoids expressing the ABE8e base editor and GFP. The organoids were continuously cultured in lung tumor medium supplemented with 0.5 $\mu g/\mu l$ puromycin, maintaining this selection pressure over several passages. After several days of puromycin treatment, the pLenti-ABE–infected organoids, which express the puromycin resistance gene, appeared healthy, dense, and compact compared to the eradicated wild-type organoids, which lack puromycin resistance under the same conditions. This ensured the stable proliferating of ABE8e-GFP-expressing organoids and the elimination of non-transduced cells lacking puromycin resistance, ABE8e and GFP.

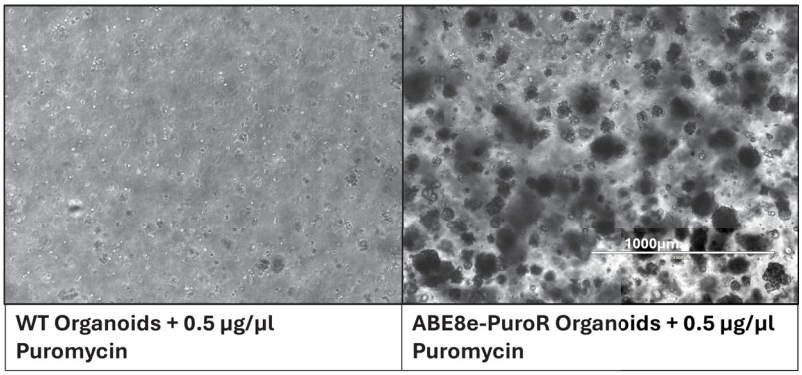

Figure 11: **Establishment of ABE8e organoid line using puromycin.** microscopic images showing wild-type and pL-ABE8e transducted PMU315 organoids after treatment with 0.5$\mu g/\mu l$ puromycin. wild-type organoids (left) display organoid cell death, while pL-ABE8e transducted organoids exhibit denser, more compact, and healthy morphology (right), indicating successful selection and enrichment of puromycin-resistant, NG-ABE8e–expressing organoids. Scale bar = 1000 μm.

This selection process resulted in the establishment of a stable PMU315 organoid line expressing NG-ABE8e, which was then used for targeted correction of the TP53 C275Y mutation.

5.1.3 Efficient Correction of the *TP53* C275Y (G→A) Mutation in Lung Cancer Organoids Using Adenine Base Editing Approach

To test my hypothesis for base editing the *TP53* C275Y mutation, the PMU315 organoid line expressing ABE and grown in puromycin was transduced with lentivirus carrying C275Y-targeting gRNAs and a tdTomato reporter gene. Both components were cloned into a single construct (pLenti-C275YsgRNA-tdTomato). Two C275Y-specific gRNAs were tested in parallel, along with a non-targeting control (NTC) lentivirus carrying a gRNA directed against an irrelevant region within the VEGF gene. To monitor infection efficiency and potential phenotypic effects following the transduction, tdTomato-positive cells were weekly quantified by flow cytometry. This time-course analysis allowed me to assess the potential changes in cell viability or proliferation associated with *TP53* correction, since tdTomato-positive cells also carry the gRNA. Cell viability of tdTomato-positive cells was measured over time relative to the first time point (4 dpi).

Interestingly, while the percentage of tdTomato-positive cells remained stable in organoids transduced with NTC-gRNA (blue line), both C275Y-targeting gRNAs (red lines) led to a progressive decrease in tdTomato-positive cells, although with different kinetics (Fig. 12). Notably, C275Y-gRNA1 (light red line) caused more depletion, over 50% reduction, compared to C275Y-gRNA2 (dark red line). This observation suggests that cells transduced with the C275Y-targeting constructs were selectively depleted due to a successful

correction of TP53 and restoration of functional p53 activity.

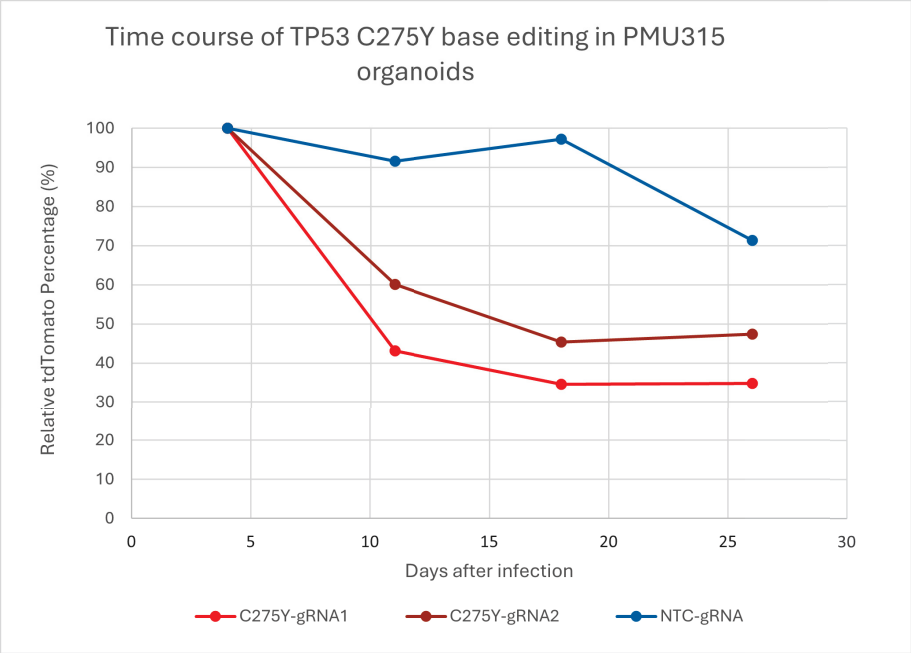

Figure 12: **Time course analysis of tdTomato-positive cells over 26 days following the Adenine base editing approach in PMU315 *TP53* C275Y organoids.** Flow cytometry analysis shows percentage of tdTomato positive cells (y-axis), calculated from two technical replicates per condition, at 4, 11, 18 and 26 days (x-axis) after lentiviral infection. Experimental conditions: C275Y-targeting gRNAs (C275Y-gRNA1: light red, C275Y-gRNA2: dark red) and a non-targeting control gRNA (NTC-gRNA: gray). The percentage of tdTomato-positive cells was normalized to day 4 after infection. Both C275Y-targeting gRNAs induced a progressive depletion of tdTomato-positive cells over time, with gRNA1 showing a stronger effect, whereas NTC-gRNA–infected organoids maintain proliferation.

To confirm that the observed depletion of tdTomato-positive cells was correlated with the genetic correction of the *TP53* C275Y mutation, organoid cells were collected at 4dpi for genomic DNA extraction and targeted Sanger sequencing following PCR over exon 8. The figure (13) shows the successful amplification of *TP53* exon 8 which resulted in 504 bp sequece in both conditions, the gRNA1 treated and the NTC organoids. As shown in Figure 14**a**, the top fragment represents the *TP53* sequence in the untreated organoids of PMU315, displaying the mutant adenine (A) at position c.824 (highlighted in the red box). The middle chromatogram shows the sequence from non-transduced control organoids at 4 dpi, where the mutation remains unchanged. In contrast, the lower chromatogram of the infected organoids with gRNA1 displays a strong guanine (G) signal at the same position, indicating efficient base editing and reversion of mutant A to wild-type G.

To quantify the editing efficiency, the sequencing reads were analyzed using EditR, a software tool for estimating base editing frequencies. As shown in Figure 14**b**, EditR

analysis revealed an average conversion efficiency of 92% A→G (highlighted in red circle), demonstrating a highly efficient correction of the *TP53* C275Y mutation back to the wild-type sequence. These findings strongly support that the depletion of tdTomato-positive cells results from successful *TP53* correction. Given the unexpectedly high and rapid editing efficiency observed in the organoids, I next sought to validate these findings and to analyze earlier time points to determine how quickly editing occurs and when phenotypic changes first become apparent.

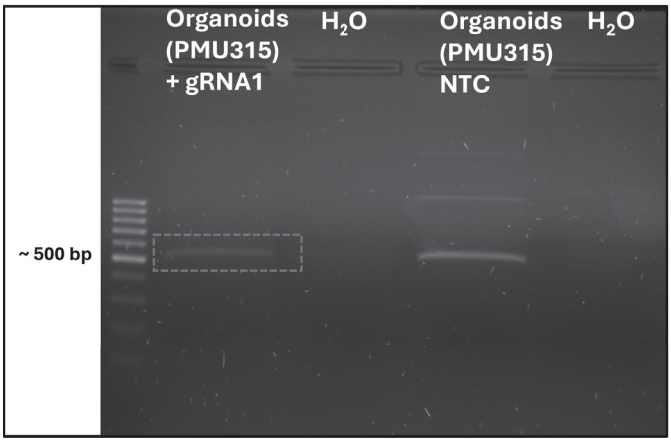

Figure 13: **PCR amplification of *TP53* exon 8 in PMU315 organoids after lentiviral infection.** Agarose gel electrophoresis showing PCR amplification of *TP53* exon 8 from gDNA of the PMU315 organoids after lentiviral infection. A clear band of the expected size (520 bp) was observed in the gRNA1 infected organoids and in the non-targeting control, confirming successful amplification. The water control (H_2O) showed no amplification, indicating the absence of contamination. A 100 bp DNA GeneRuler ladder was used as a size reference.

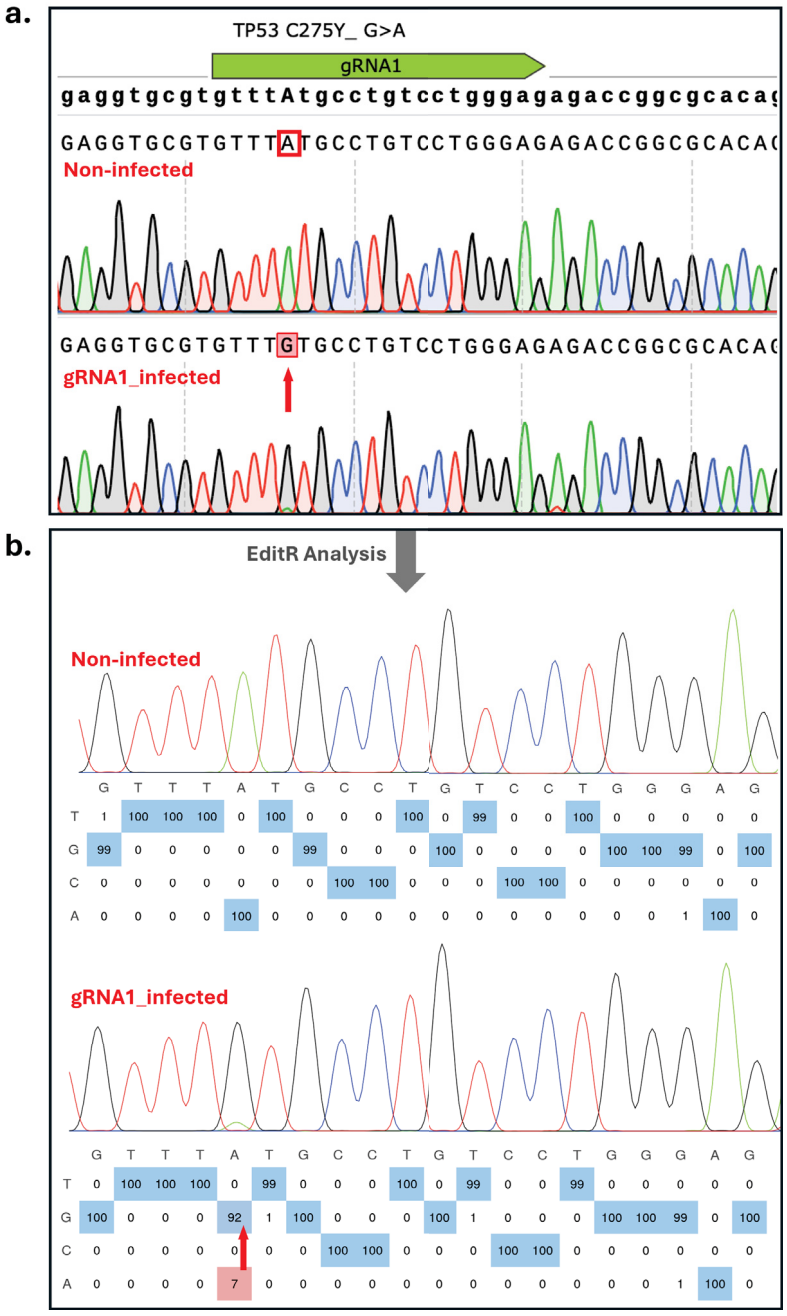

Figure 14: **Sanger sequencing chromatograms of *TP53* C275Y (G→A) mutation at 4 dpi using NG-ABE8e base editing in PMU315 organoids. a.** Sanger sequencing chromatograms showing a region of *TP53* exon 8 encompassing the C275Y (G→A) mutation. The top fragment displays the mutant sequence in untreated PMU315 organoids with the adenine (A) highlighted (red box). The middle chromatogram shows the non-infected control, where the mutation (A) remains unchanged. The bottom chromatogram represents organoids transduced with C275Y-gRNA1, showing the restoration of the wild-type guanine (G) base (indicated by a red arrow), confirming precise base editing. **b.** Quantification of the base-editing efficiency using EditR analysis of Sanger sequencing reads from non-treated and C275Y-gRNA1-treated organoids. The red highlighted boxes show mixed base frequencies, while blue boxes denote unchanged base. At the target site high frequencies of the base G have been quantified indication base conversion (A→G). EditR indicates 92% A→G conversion efficiency (indicated by a red arrow), demonstrating efficient editing.

5.1.4 Early Time Course Analysis Reveals Efficient Correction of the TP53 C275Y (G→A) within 12 Hours following Adenine Base Editing Approach

To further validate the previously observed correction of the *TP53* C275Y mutation (c.824G→A) and to better understand the onset of the editing, we performed an early time course experiment covering the period 12 to 96 hours after lentiviral transduction. The ABE8e-organoid line was transducted with the lentivirus C275Y-gRNA1–tdTomato, as gRNA1 had shown greater depletion in tdTomato-positive cells in the previous experiment. The less efficient gRNA2 was excluded from this analysis.
Notably, organoids transduced with the non-targeting control (NTC-gRNA) showed consistent proliferating tdTomato-positive cells over time. In contrast, organoids transduced with C275Y-gRNA1 displayed decreasing tdTomato signal up to 50% already at 48 hours after infection, followed by a gradual decline after day 3 (Fig. 15). The progressive depletion (over 75%) of tdTomato-positive cells at 96 hpi, suggests a potential induced apoptosis in the gRNA1 treated organoids. This observation further suggests that the population infected with gRNA1 has undergone *TP53* correction and cell death.

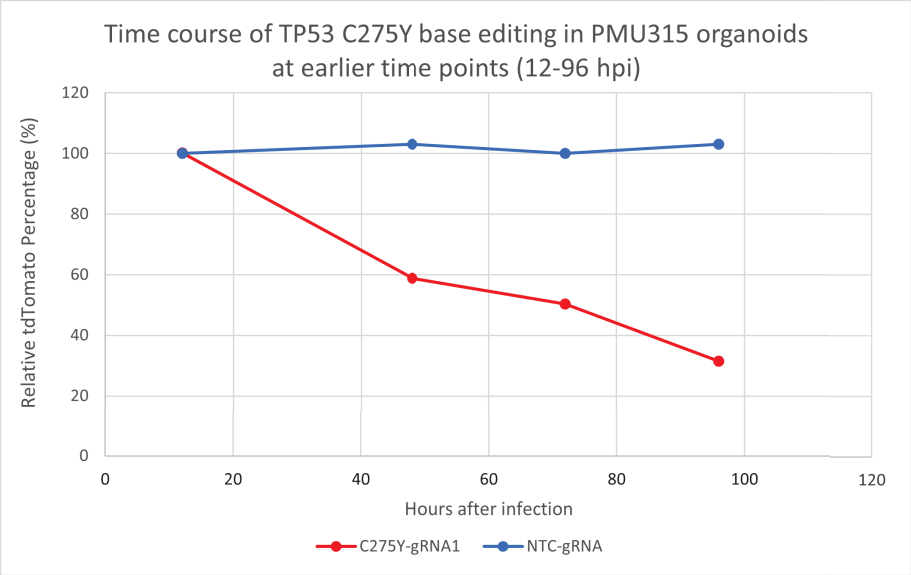

Figure 15: **Early time course analysis of tdTomato-positive cells in PMU315 *TP53* C275Y organoids following the Adenine base editing approach (12-96 hours after infection).** Flow cytometry analysis shows percentage of tdTomato positive cells (y-axis), calculated from two technical replicates per condition, at 12, 24, 48, 72, and 96 hours (x-axis) after lentiviral infection. Lentiviral constructs expressing either C275Y-gRNA1 or a non-targeting control (NTC-gRNA). The values on the y-axis represent the normalized percentage of tdTomato-positive cells relative to the initial time point (12 hpi). While the NTC-gRNA-infected organoids (blue) showed consistent expression in tdTomato-positive cells over time, the C275Y-gRNA1–transduced cells (red) showed progressive depletion in tdTomato-positive cell number.

To confirm that a growth disadvantage of C275Y-gRNA1 infected organoids is associated with correction of the *TP53* C275Y mutation, genomic DNA was isolated at 12, 48, 72, and 96 hours after infection, and *TP53* exon 8 was PCR-amplified and Sanger sequenced. The figure (16) shows the successful amplification of *TP53* exon 8 which resulted in 504 bp sequece in gRNA1-treated organoids. As an example, the successful amplicons are shown at two time points, at 12 and 48 hpi.

As shown in Sanger sequencing chromatograms (Fig. 17**a**), the upper fragment represents the sequence of untreated PMU315 organoids (non-infected), showing the mutated adenine (A) (highlighted in red). The lower chromatograms show the sequences of organoids treated with C275Y-gRNA1, where the overlapping A and G peaks (R = A or G) indicate partial editing and reversion of the mutant base toward the wild-type guanine (G). Quantitative analysis using EditR revealed approximately a 60% A→G conversion efficiency at 12 hours post infection, demonstrating that base editing occurs rapidly within hours after transduction (Fig. 17**b**). At later time points 48, 72 and 96 hpi, the editing efficiency gradually decreased to 43%, 40% and 37%, respectively (Fig. 18). This decline parallels the observed reduction in tdTomato-positive cells, supporting the hypothesis that corrected cells are selectively depleted due to *TP53* correction.

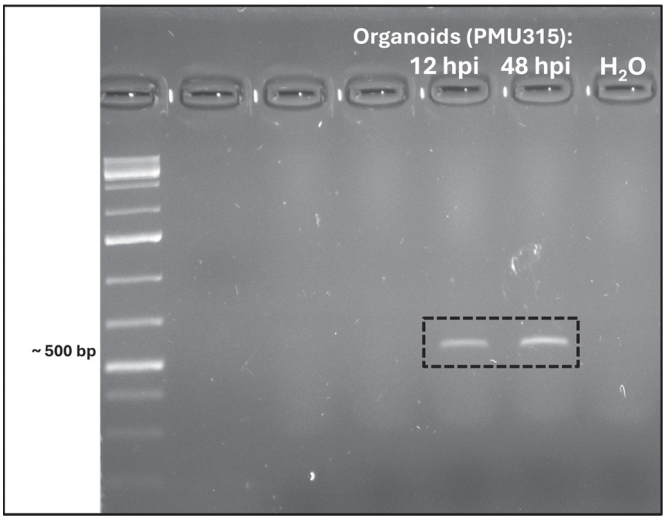

Figure 16: **PCR amplification of *TP53* exon 8 in PMU315 organoids at 12 and 48 hours after lentiviral infection.** Agarose gel electrophoresis showing PCR amplification of *TP53* exon 8 from gDNA of the PMU315 organoids after lentiviral infection with gRNA1. A clear band of the expected size (520 bp) was observed in the gRNA1 infected organoids at 12 and 48 hpi, confirming successful amplification. The water control (H_2O) showed no amplification, indicating the absence of contamination. A 100 bp DNA GeneRuler ladder was used as a size reference.

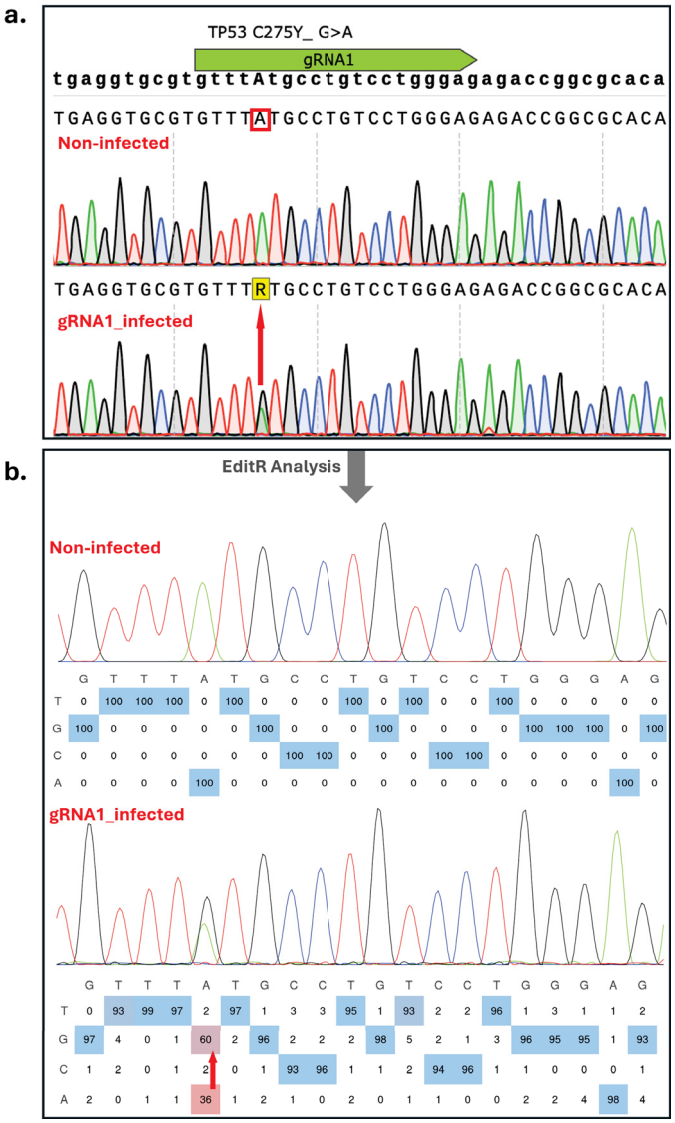

Figure 17: **Sanger sequencing chromatograms of *TP53* C275Y correction at early time point, 16 hpi, in PMU315 organoids using NG-ABE8e base editing a.** Sanger sequencing chromatograms showing a region of *TP53* exon 8 encompassing the C275Y (G→A) mutation. The top fragment displays the mutant sequence in untreated PMU315 organoids with the adenine (A) highlighted (red box). The middle chromatogram shows the non-infected control, where the mutation remains unchanged. The bottom chromatogram represents organoids transduced with C275Y-gRNA1, showing overlapping A and G peaks (R = A or G) indicate partial reversion of the mutant base toward the wild-type guanine (G) (indicated by a red arrow). **b.** Quantification of the efficiency of base-editing using EditR analysis of Sanger sequencing reads from non-treated and C275Y-gRNA1-treated organoids. The red highlighted boxes show mixed base frequencies, while blue boxes denote unchanged base. At the target site high frequencies of the base G have been quantified indication base conversion (A→G). EditR indicates 60% A>G conversion efficiency, demonstrating partial correction.

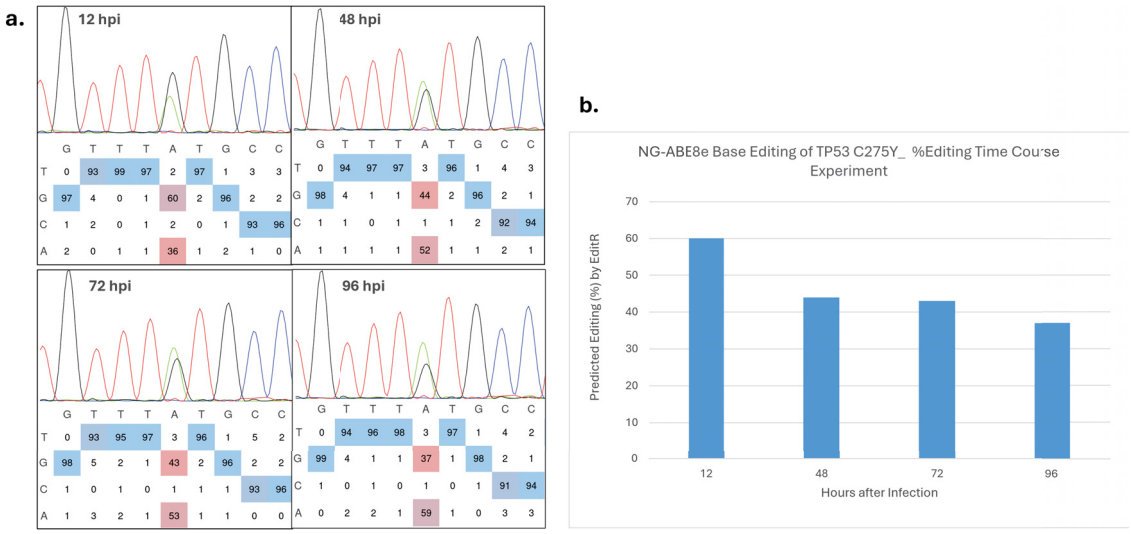

Figure 18: **EditR Quantification of predicted editing percentage of *TP53* C275Y (G→A) at early time points. a.** Sanger sequencing chromatograms analyzed with EditR show base editing of the TP53 C275Y (G→A) mutation at 12, 48, 72, and 96 hours after infection (hpi). The red highlighted boxes show mixed base frequencies, while blue boxes denote unchanged base. At the target site high frequencies of the base G have been quantified indication base conversion (A→G). **b.** Quantification of the predicted editing efficiency from EditR is summarized in the bar graph. Editing efficiencies 60%, 43%, 40%, and 37% are plotted against time points 12, 48, 72, and 96 hpi, respectively. This demonstrates that base editing occurs rapidly within hours after infection and declines over time due to depletion of corrected cells.

EditR Quantification of predicted editing TP53 C275Y (G→A) Sanger sequencing chromatograms analyzed with EditR show progressive base editing of the TP53 C275Y (G→A) mutation at 12, 48, 72, and 96 hours post-infection (hpi). The red highlighted boxes show adenine base conversion (A→G) frequencies at the target site, while blue boxes denote unchanged base. Quantification of the predicted editing efficiency from EditR is summarized in the bar graph (right), This consistent detection of rapid and efficient A→G conversion demonstrates the reproducibility of the base editing approach and the efficiency of the designed gRNA1 in correcting *TP53* C275Y point mutation using the NG-ABE8e.

5.1.5 Deviation between Editing Efficiency and tdTomato Expression Suggests Partial Viral Packaging or Reporter Silencing

Although, the percentage of edited cells decreased within the first three days after infection (Fig. 18), tdTomato-positive cells remained relatively stable during this period (Fig. 15). This observation suggests that edited cells were not necessarily tdTomato-positive, indicating that successful gRNA1 delivery does not strictly correlate with tdTomato expression.

Flow cytometry quantification from both experiments, the long-term experiment (chapter 5.1.3) and the Early time course experiment (chapter 5.1.4), revealed low infection rate, despite high editing. Looking at the percentage of tdTomato-positive cells, which theoretically represents the infection rate, we can see that it has never exceeded approximately 37.2% at 4 dpi in the long-term experiment and 27.1% at 12 hpi in the early time course (Fig. 19). In contrast, Sanger sequencing from the same samples (at 4 dpi) indicated up to 92% A→G conversion efficiency at 4 dpi in the long-term experiment and 60% A→G conversion at 12 hpi in the early time course.

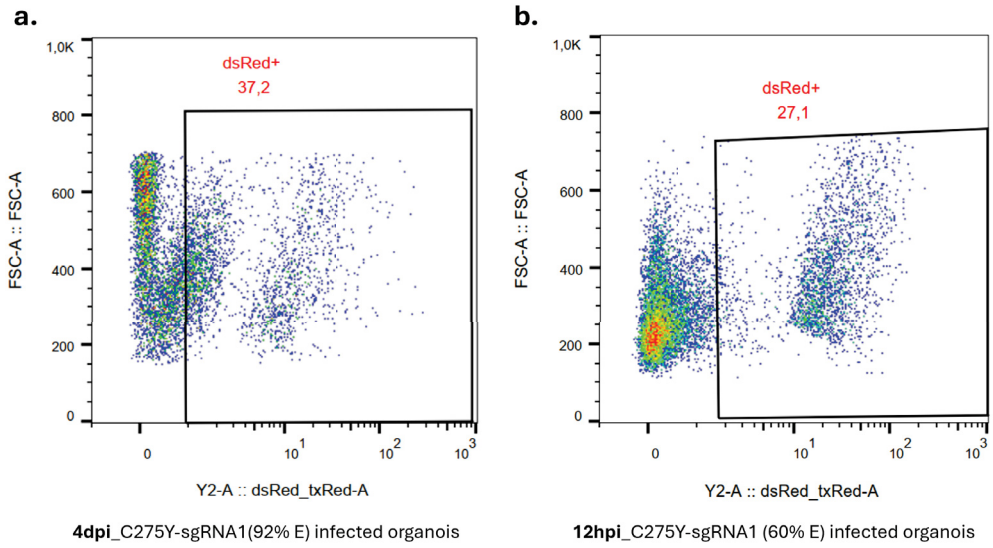

Figure 19: **Flow cytometric Plots of tdTomato-positive cells at 12 hpi and 4 dpi with sgC275Y-gRNA1. a.** Representative FACS plot showing 37.2% tdTomato-positive cells (dsRed$^+$) in PMU315 organoids 4 days after lentiviral transduction with the sgC275Y-gRNA1-tdTomato construct. This lentiviral infection experiment showed 92% Editing (C275Y-gRNA1 (92% E)) at 4 dpi. **b.** Approximately 27.1% of the organoid cells were tdTomato-positive (dsRed$^+$) at 12 hpi in the next lentiviral transduction experiment where we showed 60% Editing (C275Y-gRNA1 (60% E)). Despite the low tdTomato signal in both experiments, corresponding Sanger sequencing analysis of genomic DNA from 4 dpi and 12 hpi revealed 60% and 92% A→G base conversion efficiency respectively.

While tdTomato served as a marker for infection rate, its expression did not accurately reflect the percentage of edited cells. Two possible explanations were considered: (1) heterogeneous viral packaging during lentivirus production, leading to separation of the tdTomato and gRNA sequences, or (2) transcriptional silencing of the tdTomato promoter (EF1α) sequence in organoid cells.

To assess which of these two hypotheses was more likely, we next performed an experiment using another characterized cell model which routinely used in our laboratory

and known to robustly express lentiviral transgenes.

5.1.6 Characterization of tdTomato Reporter Expression in Panc-1 Cells

To investigate whether the reduced tdTomato expression observed in lung cancer organoids was caused by virus packaging problems or by organoid-intrinsic mechanisms, we designed an experiment using a cell line established in the laboratory, the well characterized pancreatic cancer cell line Panc-1. The same lentiviral vectors used in the previous experiments were tested for their ability to drive tdTomato expression in this cell line. The following conditions (viral constructs) were included:

1. sgC275Y-tdTomato (92% E)— used in the experiment showing 92% editing efficiency at 4 dpi.
2. sgC275Y-tdTomato (60% E) — used in the experiment showing 60% editing efficiency at 12 hpi.
3. sgR173H-tdTomato and V133-tdTomato — additional control viruses targeting unrelated genomic sites.

The last two viruses served as positive controls for proper viral packaging and reporter expression, as they are known to yield strong tdTomato signals in other assays done in our laboratory. Panc-1 cells were infected with each of the four viral preparations using increasing viral volumes (1 μL, 10 μL, and 50 μL) and analyzed by flow cytometry at 24, 48, and 72 hours post infection (hpi). Flow cytometric analysis revealed that tdTomato expression in Panc-1 cells increased in a dose-dependent manner for all viral constructs. Here I will show the example of the infection with one viral volume, 50μl.
Notably, the sgC275Y-tdTomato (92% E) virus produced the highest tdTomato-positive cell percentages, almost 100% across all tested viruses, followed by sgC275Y-tdTomato (60% E) with 80% tdTomato-positive cells at 24hpi and almost 100 at 72 hpi (Fig. 20). Both constructs exhibited robust reporter expression levels comparable or even exceeding to those of the positive control viruses sgR175H-tdTomato and V133-tdTomato.

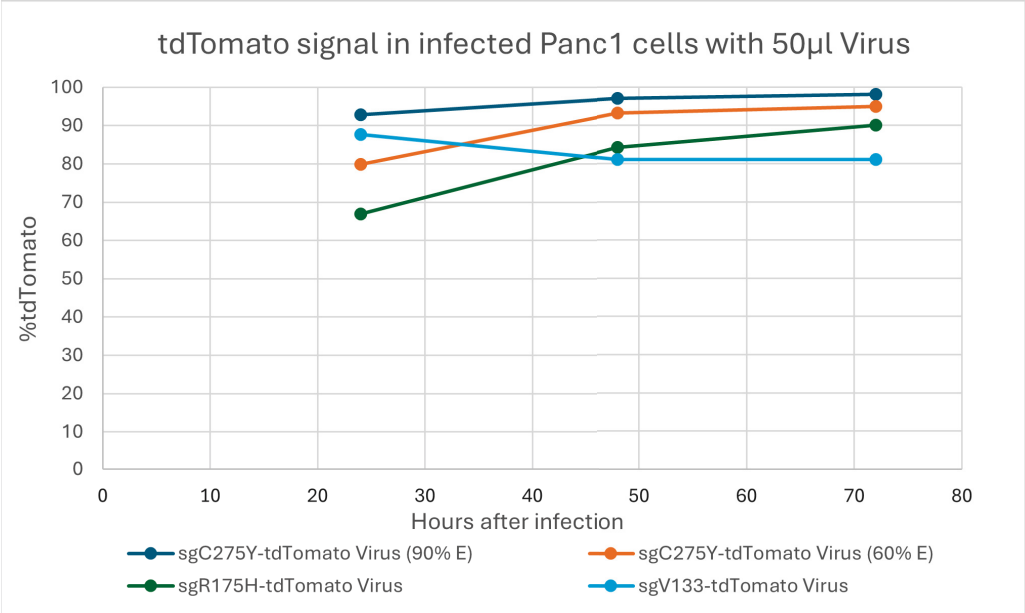

Figure 20: **Time course of tdTomato-positive Panc-1 cells over 72 hours following infection with four different lentiviral constructs.** Flow cytometry quantification of tdTomato-positive Panc-1 cells at 24, 48, and 72 hours post infection (hpi). The sgC275Y-tdTomato infected cells exhibited a steadily increasing tdTomato-positive population, reaching nearly 100% by 72 hpi. Control infections with sgR173H-tdTomato and sgV133-tdTomato also shows high tdTomato expression levels, though slightly lower than those observed in sgC275Y-tdTomato–infected cells at the same time point (72 hpi).

Together, these experiments demonstrate that adenine base editing can efficiently and precisely correct the *TP53* C275Y mutation in patient-derived lung cancer organoids. The high correction rates, combined with the subsequent depletion of corrected cells, indicate that the C275Y mutation provides a strong survival advantage to the lung tumor organoids PMU315 and that restoring wild-type p53 function may reactivates tumor-suppressive pathways. Despite partial reporter silencing, the overall findings establish a robust framework for functionally question *TP53* mutations directly in organoid models. These results highlight the feasibility and biological relevance of base-editing approaches in lung cancer organoids and set the stage for applying CRISPR strategies to additional oncogenic alterations such as the KIF5B–RET fusion examined in the next section.

5.2 Targeting approaches of Fusion Oncogene KIF5B:RET in Lung Cancer Organoids

Fusion oncogenes involving REarranged during Transfection *RET* represent potent driver mutations in non-small cell lung cancer (NSCLC). RET encodes a receptor tyrosine ki-

nase that plays an important role in cell growth and differentiation. Its constitutive activation through gene fusion leads to uncontrolled oncogenic signaling. Despite the development of selective RET tyrosine kinase inhibitors (TKIs), patients frequently develop acquired resistance during treatment [7]. Recent advances in CRISPR-Cas9 genome-editing technologies have opened new ways to directly disrupt oncogenic fusion genes. By introducing double-strand breaks (DSBs) at defined genomic loci, CRISPR–Cas9 induces an error-prone non-homologous end joining (NHEJ) repair pathway, which can generate insertions or deletions (indels) that disrupt gene function [52].

Therefore, I aimed to establish a genome-editing approach to selectively disrupt fusion oncogenes in patient-derived lung cancer organoids. This approach is designed to serve as functional analysis of oncogenic drivers and to explore its potential use for future personalized therapeutic platform. To achieve this, two CRISPR–Cas9 nuclease-based targeting strategies were designed. The first strategy is *Breakpoint targeting*, which targets the unique junction region of the *KIF5B–RET* fusion gene. The second is *Dual-intron targeting*, which involves two gRNAs designed to cut within intronic regions, designed to delete a larger genomic fragment encompassing the fusion breakpoint [53]. While the breakpoint-targeting strategy is designed to directly cleave the unique KIF5B–RET fusion junction, the dual-intron-targeting approach induces double-strand breaks within introns flanking the fusion region, resulting in a large genomic deletion. Unlike the breakpoint-targeting method, the dual-intron strategy does not require prior knowledge of the exact fusion breakpoint sequence, which represents a potential advantage for therapeutic applications, as it could be applied based on standard diagnostic information alone [53].
Both approaches mostly followed by the non-homologous end joining (NHEJ) DNA repair mechanism. In the breakpoint-targeting approach, repair through NHEJ often introduces small indels at the cut site, leading to frameshift and the generation of premature stop codons that disrupt the fusion transcript. In the dual-intron approach, repair following cleavage and excision results in the joining of distant exons in an out-of-frame configuration, also producing premature stop codons and a non-functional fusion transcript [54].
For experimental validation, we utilized the PMU315 organoid line, derived from a lung adenocarcinoma patient harboring the *KIF5B–RET* fusion oncogene, which is known to act as a key oncogenic driver in this cancer subtype [23]. If the CRISPR components successfully induced double-strand breaks and disrupted the oncogenic *KIF5B-RET* fusion, a reduction in the number of live cells was expected in the treated conditions due to loss of oncogene function.

5.2.1 Validation of oncogenic Fusion *KIF5B-RET* in PMU315 organoids

Before applying CRISPR-Cas9 strategies, it was necessary to confirm the presence and precise genomic sequence of the *KIF5B–RET* fusion in PMU315 organoids. For this purpose, genomic DNA (gDNA) was isolated from the organoids and used as a template for polymerase chain reaction (PCR) to amplify the region encompassing the predicted fusion breakpoint. The amplified fragments were then analyzed by agarose gel electrophoresis, purified, and analyzed to Sanger sequencing for breakpoint verification. Fusion coordinates were initially predicted based on deep RNA sequencing data generated by collaborators at the NCT Institute (Fig. 21). Because the exact genomic fusion junction was unknown, several primer pairs were systematically designed to cover potential breakpoint regions across the *KIF5B* and *RET* introns and exons (Fig. 21).

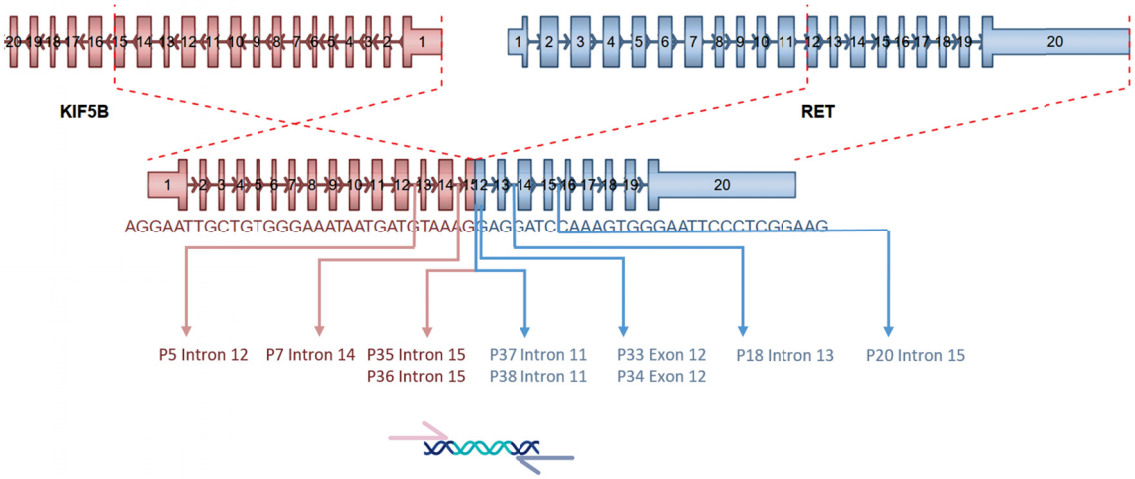

Figure 21: **Schematic representation of *KIF5B–RET* fusion region and primer design strategy.** The diagram illustrates the gene structures of KIF5B (red) and RET (blue) on chromosome 10, with exon–intron organization shown based on deep RNA Sequencing analysis of the fusion oncogene. The fusion involves the 5'-region of KIF5B and the 3'-region of RET. It shows the breakpoint between exons (15 and 12) since it reflects only the transcript-level fusion. Multiple candidate primer sites were designed within the intronic and exonic regions surrounding the predicted breakpoint to identify the exact correct sequence fusion junction. Arrows indicate the positions and orientations of primers used for PCR reactions. KIF5B primers (P5, P7, P35, P36) are located within introns 12, 14, and 15, while RET primers (P18, P20, P33, P34, P37, P38) are positioned within introns 11, 13 and 15 or exon 12. The KIF5B primers are forward and the RET primers are reversed.

Initial PCR attempts using Phusion High-Fidelity DNA Polymerase and Taq DNA Polymerase did not produce specific amplification products. Consequently, Herculase II Fusion DNA Polymerase was selected for subsequent reactions due to its higher processivity with complex or GC-rich templates. PCR conditions were optimized for each primer

pair, including annealing temperature and extension time. To accommodate the expected large amplicon size, the extension phase was gradually increased to 2.5 minutes per cycle.
PCR products obtained with Herculase II were evaluated on a 1% agarose gel to assess amplification specificity and yield. Among all tested primer combinations, only the P31, P33 pair generated a distinct and reproducible product. Gel electrophoresis using DNA Ladder 1 kb Plus as a reference revealed a single prominent band of approximately 4 kb (Fig. 22), indicating successful amplification of the genomic region containing the KIF5B-RET fusion breakpoint.

Herculase II Fusion DNA Polymerase successfully amplified the target region, showing higher processivity and better tolerance for complex templates.
To confirm that the amplified fragment encompassed the predicted KIF5B-RET fusion region, the corresponding 4 kb PCR product was analyzed by Sanger sequencing. Sanger sequenced PCR product from PMU315 organoid aligned to regions within KIF5B intron 15 and RET intron 11, using reference sequences (GRCh38) obtained from the UCSC Genome Browser (Retrieved March 20, 2025). The alignment can be visualized using SnapGene software, confirmed that the amplified fragment spans the genomic junction between KIF5B intron 15 and RET intron 11 (Fig. 22). The sequencing results verified that the amplicon contained sequences derived from both the KIF5B and RET genes, confirming the successful amplification of the genomic fusion fragment. Finally, I experimentally validated that the KIF5B–RET genomic fusion in the PMU315 organoid line occurs between KIF5B intron 15 and RET intron 11. This results amends the initial illustration provided by our collaborators at the NCT, which presented an exon–exon fusion based on exome sequencing data. Confirming the exact intronic breakpoint established PMU315 organoids as a reliable model for subsequent CRISPR–Cas9 targeting experiments.

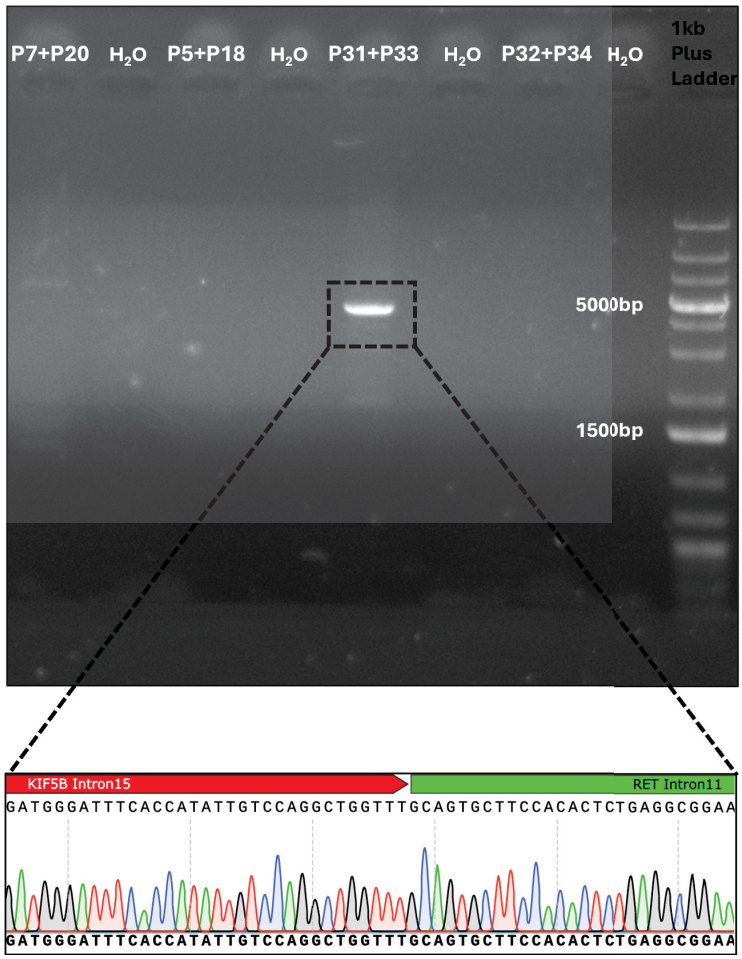

Figure 22: **PCR amplification and validation of *KIF5B–RET* fusion.** Agarose gel electrophoresis showing PCR products amplified from genomic DNA of PMU315 cells using several primer pairs. Only the primer combination **P31 + P33** (indicated by black box) produced an amplicon of approximately 4 kb. A 1 kb Plus DNA Ladder was used as a molecular size reference. Sanger sequencing reads visualized in SnapGene chromatogram showing the validated junction between KIF5B intron 15 (red) and RET intron 11 (green) in PMU315 genomic DNA. Single, narrow peaks indicate a confident base call. The corresponding nucleotide sequence alignment is shown above the chromatogram, illustrating the precise transition from KIF5B to RET. The data confirm the presence of the fusion mutation *KIF5B-RET*.

5.2.2 Targeting *KIF5B-RET* Fusion Oncogene in Lung Cancer Organoids using CRISPR-Cas9 based viral Infection Approach

After confirming the *KIF5B-RET* fusion breakpoint in the PMU315 organoid line, guide RNAs (gRNAs) were designed to disrupt the fusion using two CRISPR–Cas9 strategies. The first strategy aimed to cleave directly at the fusion breakpoint (breakpoint-targeting), while the second was designed to introduce double-strand breaks within intronic regions flanking the fusion junction (dual-intron targeting). A total of 20 gRNA candidates were designed using the design tool Integrated DNA Technologies (IDT) CRISPR, based on predicted on-target efficiency and minimal off-target activity. The top candidates were further cross-validated using Cas-OFFinder and CCtop to confirm specificity. Based on these analyses, 14 gRNAs with the highest predicted cutting efficiency and lowest off-target potential were selected for experimental testing (Supplementary Fig. S1). Due to limited organoid material, only a subset of sgRNA combinations could be tested. Therefore, the experiment was conducted using two dual-intron-targeting (DI) gRNA pairs (DI5 and DI8) and one breakpoint-targeting (BP) gRNA (Fig. 23).

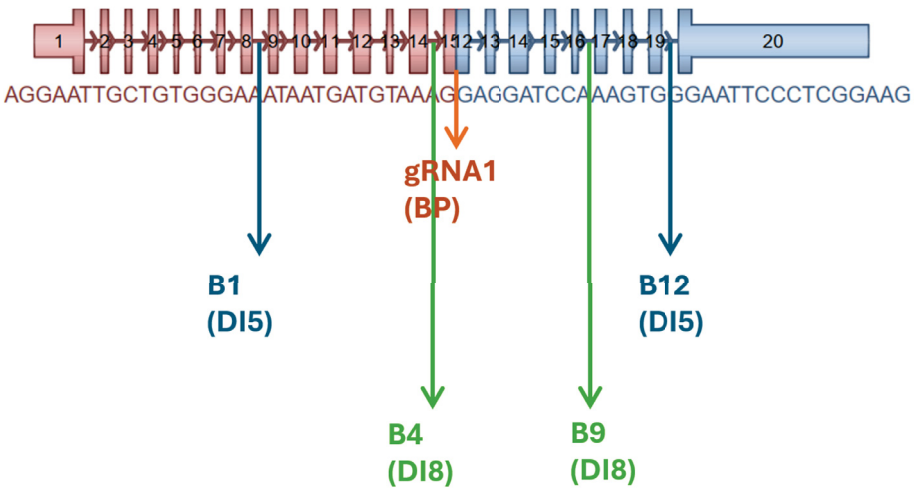

Figure 23: **Schematic representation of the *KIF5B–RET* fusion and gRNA design.** The diagram shows the gene structures of *KIF5B* (shown in red) and *RET* (shown in blue) located on chromosome 10. The *KIF5B–RET* fusion involves the 5' region of *KIF5B* and the 3' region of *RET*. Candidate guide RNAs (gRNAs) were designed to target within intronic regions, Dual-Intron-Targeting (DI), and at the breakpoint (BP) of the fusion junction. The arrows indicate the positions of the designed gRNAs: B1 in *KIF5B* intron 8, B12 in *RET* intron 19 (both in blue), B4 in KIF5B intron 14, B9 in *RET* intron 16 (both in green), and BP–gRNA1 (orange) targeting the breakpoint region.

To deliver the CRISPR components into lung cancer organoids, a lentiviral vector system

was employed. Each gRNA was cloned into the pL-CRISPR.EFS.GFP.gRNA vector (Addgene plasmid #57818; see Supplementary Fig. S3), which expresses Cas9 and a GFP fluorescent reporter. Lentiviral particles were produced using transfer vectors encoding different gRNAs to create the following experimental conditions:

1. One gRNA targeting the fusion breakpoint (BP gRNA),
2. Two gRNAs targeting the flanking introns. Each gRNA was cloned under different promoter on the same vector (e.g. U6-gRNA-B1, H1-gRNAB12),
3. One gRNA against an essential region within *Psma1* as a positive control, and
4. One gRNA targeting an irrelevant region within *VEGF*, serving as a negative control.

The same number of organoids was transduced with each lentivirus condition and flow cytometry analysis was performed at 6 dpi to evaluate transduction efficiency by quantifying GFP-positive cells (Table 12). Across all tested conditions, the percentage of GFP-positive cells did not exceed 6%, whereas an infection efficiency of approximately 50% was desired.

Table 12: **GFP expression following lentiviral transduction at 6 dpi with CRISPR–Cas9 constructs targeting *RET:KIF5B* fusion.**Table showing the percentage of GFP-positive cells following lentiviral infection with pL-CRISPR-gRNA-Cas9-GFP construct using different targeting gRNAs. Treatments include breakpoint-targeting gRNA (BP-gRNA), Dual-Intron-Targeting gRNAs (DI8), Psma1 targeting gRNA (+ control), non-targeting control (NTC), and no infection (baseline control). The proportion of GFP+ cells ranged from approximately 4% to 6%, means the level of transduction achieved was insufficient.

Lenti viral Infection with pL-CRISPR-gRNA-Cas9-GFP	GFP+ cells
BP-gRNA	4,16 %
BP-gRNA	4,08 %
Dual-Intron-Targeting-gRNAs (DI8)	6,24 %
Dual-Intron-Targeting-gRNAs (DI8)	5,80 %
Psma1 (+ control)	4,69 %
Psma1 (+ control)	4,87 %
NTC (- control)	5,27 %
NTC (- control)	4,85 %
no infection	4,00 %
no infection	4,02 %

The observed low infection rate likely resulted from the large size of the transfer vector used for the virus production, which can hinder efficient viral packaging and results

in low virus titer. Thus, the infection of the organoid line was insufficient. Consequently, the level of transduction achieved was insufficient to observe any meaningful CRISPR-mediated editing or phenotypic changes. Given these limitations, we decided to pursue an alternative virus-free delivery approach to deliver CRISPR-Cas9 components. Based on recent studies demonstrating successful RNA transfection approach and efficient targeting of fusion oncogenes [53], we proceeded to test Cas9 mRNA and gRNA transfection as an alternative delivery method.

5.2.3 Targeting *KIF5B-RET* Fusion Oncogene in Lung Cancer Organoids using RNA Transfection Approach

To demonstrate the functionality of the two CRISPR-Cas9 strategies, Breakpoint Targeting and Dual-Intron Targeting) we next employed a virus-free RNA transfection approach to deliver Cas9 and the gRNA into lung cancer organoids. This method was selected to overcome the low infection efficiency observed with lentiviral delivery. The designed sgRNAs targeted either the *KIF5B–RET* fusion breakpoint or distinct intronic regions along the fusion locus (as illustrated in Fig. S1). Therefore, the experiment was conducted using two dual-intron-targeting gRNA pairs (DI5 and DI8) and one breakpoint-targeting gRNA (Fig. 23).
Several experimental and control conditions were included:

1. BP gRNA targeting the fusion breakpoint.
2. DI5 and DI8 dual-intron gRNA combinations, each targeting two intronic regions within *KIF5B* and *RET*.
3. *POLR1C* gRNA, targeting an essential region within *POLR1C*, used as a positive control for Cas9 activity.
4. *VEGF* gRNA, targeting an irrelevant region within *VEGF*, used as a negative control.
5. Non-transfected organoids, used to control for potential transfection toxicity.

I first tested transfection efficiency using 2 pmol of Cas9 mRNA and GFP mRNA as controls. Organoids were then transfected with Cas9 mRNA and the respective fusion-targeting gRNAs. If the CRISPR components successfully induced double-strand breaks and disrupted the oncogenic *KIF5B-RET* fusion, a reduction in the number of live cells was expected in the treated conditions due to loss of oncogene function. To evaluate these effects, we performed flow cytometry analysis at two time points, 3 dpt and 7 dpt, to quantify live cell number and transfection efficiency, alongside Sanger sequencing at 3 dpt to verify genomic alterations at the target sites. The FACS dot plot displays the targeted cell population on forward scatter (FSC-A) in conjunction with GFP fluorescence

intensity (B1-A, GFP FITC-A). A distinct GFP$^+$ population was observed, representing successfully transfected cells. Quantification from the FACS plot (Fig. 24A) shows that 73.8% of the cells were GFP-positive at 3 dpt compared to the non-treated condition (Fig. 24B), indicating efficient mRNA delivery.

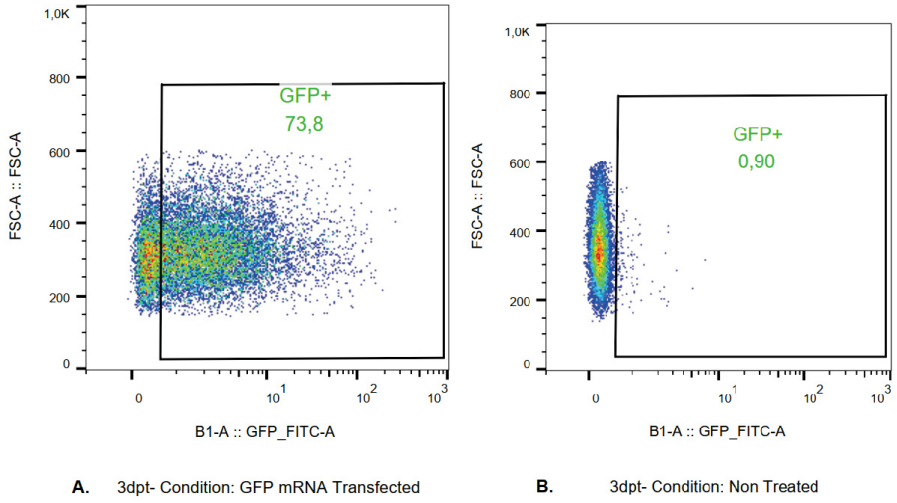

Figure 24: **GFP expression following mRNA transfection at 3 days post-transfection (3 dpt).**Flow cytometry (FACS) dot plots display the distribution of the targeted cell population based on forward scatter (FSC-A; y-axis) and GFP fluorescence intensity (GFP-FITC-A; x-axis). Plot A represents cells transfected with GFP mRNA, and Plot B shows non-treated control cells analyzed at 3 days post-transfection. At 3 dpt, 73.8% of the cells were GFP-positive (GFP$^+$) compared to only 0.9% in the non-treated control, indicating a high transfection efficiency and successful delivery of GFP mRNA.

Cell viability analysis revealed a reduction in live cell numbers in both the GFP and targeting conditions at 3 dpt, indicative of mild transfection cytotoxicity. At 7 dpt, a more pronounced decline in live cell numbers was detected in all targeting conditions BP, DI5, and DI8 compared to the VEGF control (Fig. 25). This reduction suggests impaired proliferation and recovery in organoids. These observations might be due to the expected functional consequences of efficient sgRNA-mediated cleavage at critical fusion sites.

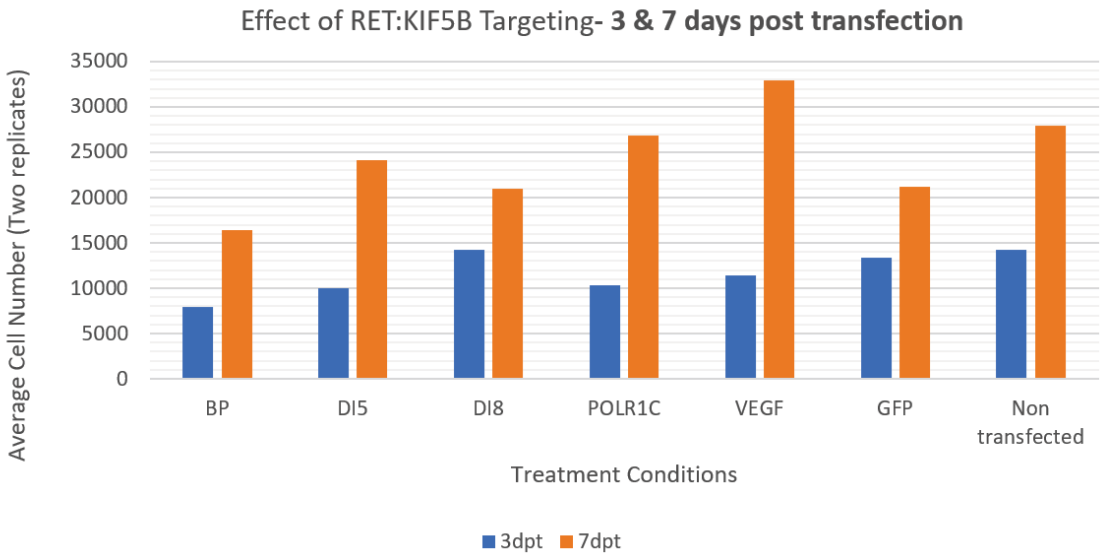

Figure 25: **Effect of *RET:KIF5B* targeting on organoid viability at 3 and 7 days post-transfection.** Bar graph showing the average number of live cells (two replicates) under different transfection conditions at 3 days after transfection (3 dpt, blue bars) and 7 days after transfection (7 dpt, orange bars). Treatment conditions include breakpoint targeting gRNA (BP gRNA), dual-intron targeting gRNAs (DI5 and DI8 gRNA pairs), POLR1C targeting gRNA, VEGF targeting gRNA and GFP mRNA-transfected organoids (transfection efficiency control), and Non-transfected organoids.

To confirm that the observed effects were indeed caused by CRISPR–Cas9-mediated editing I did a genotypic analysis. For each gRNA, the corresponding genomic region was amplified by PCR. For this, PCR performed on the gDNA isolated from organoids at 3 dpt across all experimental and control conditions. PCR amplicons were purified and analyzed by sanger sequencing. Here are the corresponding genomic regions surrounding the gRNA predicted cut site:

1. B1: KIF5B intron 8
2. B4: KIF5B intron 14
3. B9: RET intron 16
4. B12: RET intron 19

All PCR products were purified and sequenced. The resulting chromatograms (Fig. 26) display the wild-type reference sequence at the top and the treated and non-treated control sequences below. The gRNA target site is indicated by an orange arrow. For B1, a noisy sequence pattern was detected downstream of the predicted cleavage site, typical observation for NHEJ-mediated repair following Cas9 cutting. These mixed reads suggest the presence of indels that could cause frameshifts and introduce premature stop codons, thereby inactivating the fusion oncogene.

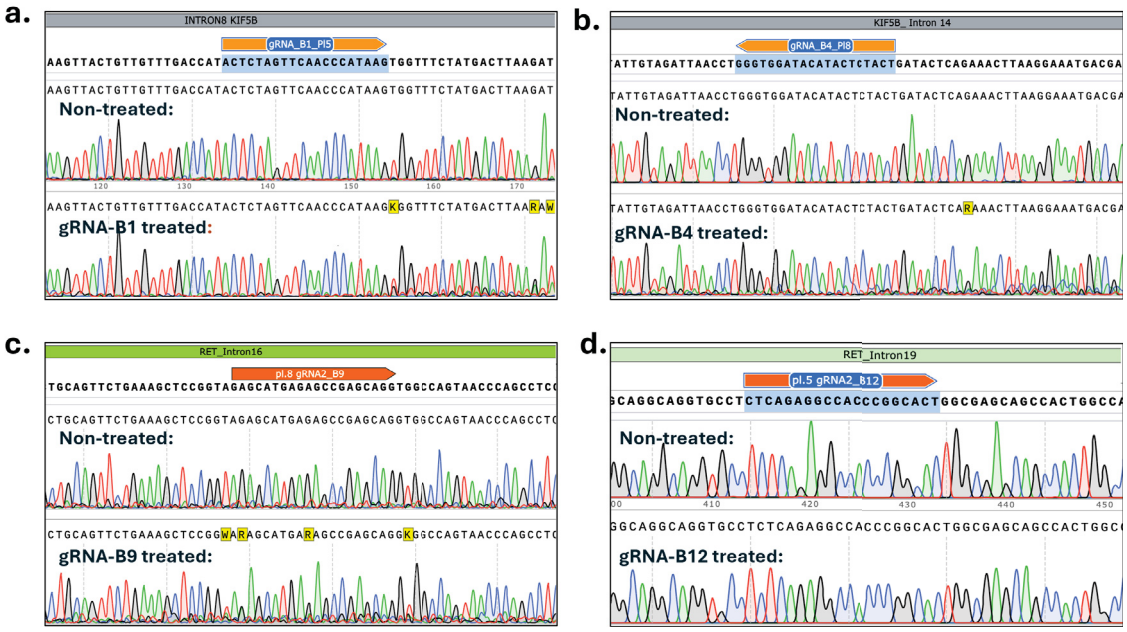

Figure 26: **Sanger sequencing validation of CRISPR–Cas9-induced edits in KIF5B and RET target introns.** locus. Sanger sequencing chromatograms showing the genomic regions surrounding the predicted Cas9 cleavage sites for the selected gRNAs: B1 (KIF5B intron 8), B4 (KIF5B intron 14), B9 (RET intron 16), and B12 (RET intron 19). The orange arrows indicate the positions and orientations of the designed gRNAs relative to the target sequence. Wild-type reference sequences are shown at the top (in bold). Target squences from CRISPR–Cas9–treated organoids and non-treated controls displayed below. **a.** In the gRNA-B1 treated sample mixed sequencing peaks downstream of the predicted cut site can be observed.

To validate editing outcomes, we used the EditCO software, which applies Inference of CRISPR Edits (ICE) algorithm. ICE analysis estimate the predicted editing efficiency by comparing the sanger sequencing mixed reads with that of a wild-type control to quantify indels introduced at the Cas9 cleavage site. In Figure 27, the sequence of the non-treated condition is shown on the top (green arrow), the edited sequence is shown below (After the red arrow). The cut sites are indicated by black vertical dotted lines, the PAM sequences by red horizontal dotted lines, and the gRNA target region is underlined. Mixed reads are clearly visible after the cutting site in the B1-treated sample (Upper one), confirming editing activity. ICE analysis predicted that approximately 10% of the sanger sequencing reads contained a single nucleotide insertion directly after the cutting site. Additional indels included 3% of reads with a deletion, 1% with two insertions and 1% with three deletions.

Figure 27: **ICE analysis of CRISPR editing outcomes using EditCO software.** The sequence targeted by gRNA B1 is shown in bold at the top. The sequence of the non-treated condition is shown on the top (green arrow), the predicted edited sequences are shown below (After the red arrow). The predicted cut site is indicated by black vertical dotted lines, the PAM sequence (TGG) by red horizontal dotted lines, and the gRNA target region is underlined. ICE analysis revealed an 15% indel prediction rate. Among edited reads there is a predominant +1 insertion (10%), with 5% minor contributions from deletions and other insertions. Sequencing data for gRNA B4 and B9 were excluded due to poor read quality.

The sequencing results for gRNA B4 could not be analyzed due to low read quality in the treated sample. Similarly, for gRNA B9, both the treated and control samples showed poor sequencing quality. In contrast, the gRNA B12 treated sample produced clean, high-quality reads identical to the control sequence, indicating that gRNA B12 was not effective in inducing a cut at the target site.

Taken together, these experiments demonstrate that CRISPR–Cas9 can successfully induce approximately 15% targeted editing at intron 8 of KIF5B using gRNA-B1 in patient-derived lung cancer organoids. Although editing efficiency remained low and no strong phenotypic effects were detected, the results establish an important foundation for further optimization of Cas9 delivery and disruption strategies of fusion oncogenes. These findings set the stage for a broader discussion of technical limitations, biological factors, and future improvements in the following section.

6 Discussion

6.1 TP53 C275Y Correction

In this project, I applied CRISPR-mediated adenine base editing (ABE8e) to correct the TP53 C275Y (G→A) point mutation in patient-derived lung cancer organoids. This work demonstrates, for the first time, the feasibility of precise genetic correction of TP53 mutations in primary lung tumor organoids. These results demonstrate not only

the technical feasibility of achieving high editing efficiency in a complex 3D model but also provide functional evidence that repairing TP53 C275Y point mutation impacts tumor cell survival in lung cancer.

6.1.1 Efficient and Rapid Correction of the TP53 C275Y Mutation in Lung Cancer Organoids

The editing kinetics revealed that correction the G→A mutation occurred remarkably fast after lentiviral transduction, with approximately 92% editing efficiency detectable at 4 days post infection. The rapid 60% editing already at 12 hours after infection highlights the high efficiency of the NG-ABE8e base editor and underscores its potential for precise genome correction in organoid systems. The editing efficiency of 37% in early-time course experiment was lower than the 92% observed previously, both measured at 4 dpi. This variation likely reflects differences in viral titer between two independent lentiviral preparations. Nevertheless, the consistent detection of rapid and efficient A→G conversion demonstrates the reproducibility of the base editing approach, the efficiency of the designed gRNA1 and confirms the feasibility of correcting *TP53* point mutations in lung cancer organoids using base editors.
Importantly, this work provides the first demonstration of successful base-editing–mediated correction of the TP53 C275Y mutation in human lung cancer organoids, establishing a proof of principle that disease-relevant mutations can be efficiently repaired in patient-derived 3D cancer models. Although editing efficiencies varied between experiments, the consistent detection of early A→G conversion validates the robustness of the approach and confirms that TP53 can be efficiently and precisely corrected.

6.1.2 Functional Consequences of TP53 Correction

A key finding of this study is that the population of cells carrying the corrected TP53 allele was progressively depleted over time, as seen by the decline in tdTomato-positive cells following infection with the C275YgRNA-targeting construct. This depletion indicates that restoration of wild-type p53 function confers a strong growth disadvantage or loss of viability to the edited cells. In other words, tumor cells harboring the C275Y mutation appear to rely on the mutant p53 for survival, and its correction reactivates tumor-suppressive pathways leading to growth arrest and apoptosis. This functional outcome provides direct biological evidence that the TP53 C275Y mutation is essential for maintaining tumor cell viability. Thus, beyond technical success, the data reveal a functional dependency on mutant p53, underscoring the oncogenic importance of this C275Y mutation. Together, these findings represent the potential of base editing to test

such mutation dependencies in organoid systems, and a significant step toward applying base editing as a potential therapeutic tool in personalized cancer models.

6.1.3 Deviation between Editing Efficiency and Reporter Expression

An interesting technical observation was the deviation between high editing efficiency and relatively low tdTomato reporter expression. While tdTomato served as a marker for infection rate, its expression (27.1-37.2%) did not accurately reflect the percentage of edited cells (60-90%).
This clear discrepancy between tdTomato expression and measured editing percentage raises an important technical question: how can a relatively low infection rate, indicated by tdTomato-positive cells, correspond to such a high base editing efficiency?

We considered two main hypotheses to explain this observation.
First, incomplete or heterogeneous viral packaging during lentiviral production could have led to unsuccessful encapsulation of the full-length transfer vector (U6-C275YsgRNA-EF1α-tdTomato) in some viral particles, leading to separation of the tdTomato reporter cassette from the gRNA expression cassette [55]. As a result, some viral particles may have delivered only the functional gRNA without the linked tdTomato sequence. Given that the organoid line already constitutively expresses the ABE8e base editor, the presence of the gRNA alone would be sufficient to induce rapid editing immediately after viral-RNA entry, without requiring reverse transcription and integrating into the genome of the transducted RNA sequence. Second, as Tdtomato is expressed from EF1α polII DNA promoter, in contrast to the gRNA expressed from the U6 polIII RNA promoter, the organoids may exhibit transcriptional silencing of the EF1α promoter, potentially through epigenetic mechanisms such as promoter methylation or chromatin remodeling. Such silencing could lead to incomplete or variable reporter expression even in cells that were successfully transduced with the full construct.
Taken together, these results suggest that tdTomato expression alone may underestimate the actual infection and editing rates in this particular Lung cancer organoids. To assess which of these two hypotheses was more likely, we next performed an experiment using Panc-1 cells, a well characterized pancreatic cancer cell line established in our laboratory and known to robustly express lentiviral transgenes. This experiment aimed to determine whether the reduced tdTomato signal observed in lung cancer organoids resulted from intrinsic silencing mechanisms within the organoids or from technical issues related to virus production.

Subsequent validation in Panc-1 cells confirmed strong and consistent tdTomato expression for all constructs.

These findings demonstrate that the tdTomato reporter gene and its promoter within the sgC275Y-tdTomato construct is functional and efficiently expressed in Panc-1 cells. Therefore, the reduced tdTomato signal observed in the patient-derived lung cancer organoids is more likely due to cell type specificity rather than to defective viral packaging. Thus, a plausible explanation for this phenomenon is that patient-derived lung cancer organoids may exhibit transcriptional silencing of the tdTomato gene, potentially through epigenetic mechanisms such as promoter methylation or histone modification around the integrated reporter gene locus. Indeed, a study has shown that lentiviral-delivered transgenes can undergo silencing in human and murine cells. This could happen via methylation of promoters and heterochromatin formation [56].
Together, these results support the conclusion that the low tdTomato expression observed in lung cancer organoids is primarily due to intrinsic silencing mechanisms, rather than errors in viral vector packaging of tdTomato sequence beside the gRNA. However, we cannot definitively exclude that, in some viral particles, the gRNA sequence may have been packaged independently of the tdTomato reporter gene [55] [57]. Moreover, the detection of editing events within hours after infection points to the possibility of gRNA-mediated editing occurring even before a complete tdTomato transcription and translation. These data therefore confirm our hypothesis that organoid-intrinsic silencing of the tdTomato reporter likely contributes to the deviation between editing efficiency and tdTomato expression, although partial separation of gRNA and reporter packaging remains a potential co-occurring event.

6.1.4 Implications and Future Directions

These findings have both biological and methodological implications. Biologically, they reveal that restoring wild-type *TP53* in tumor organoids triggers cell loss, providing direct evidence that the *TP53* C275Y mutation is critical for tumor cell survival. This establishes base editing not only as a correction tool but also as a functional approach for identifying mutation-specific dependencies in cancer.
Future work should focus on integrating deep sequencing and single-cell transcriptomic profiling to better understand editing heterogeneity and the cellular consequences of *TP53* restoration. In particular, performing deep sequencing on genomic DNA isolated at 26 dpi from sorted tdTomato-positive cells will be crucial to determine whether the 30% of persistent tdTomato-positive cells at 26 dpi represent successfully edited cells that survived, or non-edited tdTomato-positive cells that escaped base editing. This analysis will clarify whether a subpopulation of this tumor can tolerate p53 reactivation or whether resistance mechanisms may have emerged in edited cells. In parallel, bulk RNA sequencing would enable a direct assessment of p53 pathway activation,

confirming whether the corrected *TP53* allele is not only genetically reverted but also functionally expressed and translated. This approach would also identify downstream p53 target genes and reveal which transcripts are up- or downregulated upon *TP53* correction. Such information would provide insight into which p53-dependent cell death pathways, such as apoptosis, ferroptosis, or pyroptosis, are activated in the organoids and help map the transcriptional programs driving growth arrest or cell death in edited cells. Single-cell RNA sequencing would further allow us to assess whether different cell subpopulations within the organoids respond differently to p53 restoration or whether they uniformly activate the same p53-dependent stress programs. Finally, extending and validating *TP53* C275Y correction in additional cell lines or organoid models carrying the same mutation would be essential to confirm the reproducibility of the observed p53 activation and strengthen the biological conclusions of this study.

6.2 Targeting the Oncogenic Fusion *KIF5B-RET*

In this experiment we aimed to establish a CRISPR-Cas9-based genome editing strategies to selectively target oncogenic fusion genes in patient-derived lung cancer organoids. The KIF5B–RET fusion, a well-characterized driver oncogene in non-small cell lung cancer (NSCLC), was chosen as a model to evaluate two editing strategies in the lung cancer organoids: (1) breakpoint targeting and (2) dual-intron targeting. Both strategies were developed with the goal of establishing functional analysis platform of fusion mutations. A total of 14 gRNAs were successfully designed and computationally validated based on predicted on-target activity and low off-target potential. Candidate guides were cross-validated using Cas-OFFinder and CCtop to ensure target specificity.

6.2.1 Validation of oncogenic Fusion *KIF5B-RET* in PMU315 organoids

Determining the precise *KIF5B–RET* fusion breakpoint in the PMU315 organoid line required several rounds of PCR optimization using different primer combinations, polymerases, and cycling conditions. Multiple attempts with standard high-fidelity enzymes failed to yield a product, indicating that the fusion locus is a technically challenging region to amplify. Although Phusion polymerase is known for its exceptionally low error rate ($\approx 4.4 \cdot 10^{-7}$) [58] and high fidelity, it did not yield detectable products for the KIF5B–RET fusion region. This outcome is likely due to the technical challenges associated with amplifying long genomic fragments (4 kb) that encompass intronic regions with high GC content and potential secondary structures [59]
However, amplification was successful only when using the primer pair P31/P33 together with the Herculase II polymerase, which enabled amplification of the genomic junction between KIF5B intron 15 and RET intron 11.

This outcome highlights an important methodological consideration. PCR success could depends on the compatibility between the polymerase and the structural complexity of the target sequence. Long genomic regions, high GC content might significantly reduce amplification efficiency. Previous studies have similarly shown that polymerase choice greatly affects amplification of GC-rich or complex templates [59]. Herculase II, optimized for long, GC-rich, and structurally difficult amplicons, proved most suitable for amplifying the fusion breakpoint in PMU315. This underscores the importance of systematically optimizing PCR parameters, including polymerase selection, annealing temperature, and extension time, to achieve amplification of challenging genomic regions. Successfully resolving the *KIF5B–RET* breakpoint was essential for confirming the exact intronic junction in this organoid line and provided the required foundation for designing and validating CRISPR–Cas9 targeting strategies in the subsequent experiments.

6.2.2 Targeting *KIF5B-RET* Fusion Oncogene in Lung Cancer Organoids using CRISPR-Cas9 based viral Infection Approach

First we produced a lentiviral system to deliver the CRISPR-Cas9 components via all-in-one lentiviral plasmid (Fig. S3). However, the infection efficiency, as measured by GFP-positive cells at six days post-infection, was markedly low. This inefficiency can be attributed to the large size of the lentiviral transfer vector, which is known to hinder viral packaging efficiency during virus production and dramatically reduce viral titers [60]. Lentiviruses have a packaging limit of approximately 8–9 kb, and exceeding this range often lead to low titer virus. As a result, the transduction efficiency in PMU315 organoids was insufficient to induce genome editing or phenotypic effects. Therefore, the big vector size contributed to the poor infection rates observed in this experiment.

6.2.3 Targeting KIF5B-RET Fusion Oncogene in Lung Cancer Organoids using RNA Transfection Approach

Due to the limitations of viral delivery, a virus-free RNA transfection approach was tested as an alternative method for delivering the CRISPR–Cas9 components. Transfection of Cas9 mRNA and gRNAs led to efficient uptake, as confirmed by GFP mRNA transfection control. A slight reduction in live cell numbers was observed in the targeting conditions compared to the non-targeting control (VEGF), suggesting potential cutting related activity (Chapter 5.2.2).
Sanger sequencing analysis of the B1 gRNA target site indicated that approximately 10% of the sequencing reads contained a single-nucleotide insertion downstream of the Cas9 cleavage site, as predicted by ICE analysis (Inference of CRISPR Edits). This finding is consistent with successful DSB induction and subsequent error-prone repair

NHEJ pathway, which commonly introduces small indels leading to frameshift mutations. However, sequencing of other target regions (B4, B9, B12) resulted in low-quality chromatograms, likely due to insufficient genomic DNA resulting from limited organoid material.
Because the observed editing efficiency was not sufficient and phenotypic changes were not significant, a second round of optimization was performed using increased Cas9 mRNA concentration (6 pmol) and new gRNA combinations (B1 + B9 and B4 + B9). Despite these efforts, no distinct genotypic phenotypic effects were detected. A likely reason for the limited editing efficiency observed could be an imbalance between the amounts of Cas9 mRNA and gRNA, which could have reduced the formation of active Cas9-gRNA complexes. Future experiments could test different ratios with higher Cas9 concentrations (up to 10 pmol). Increasing the number of organoids per experimental condition would also allow more robust analysis by providing sufficient genomic DNA concentration for sequencing at multiple time points, capturing early and late repair events.
Another possible explanation for the low editing efficiency is the instability or silencing of exogenous Cas9 mRNA in organoid cells. Previous reports have shown that exogenous nucleic acids, particularly those encoding large proteins such as Cas9, can undergo rapid degradation or transcriptional silencing in mammalian and stem cell–derived systems [61].

6.2.4 Future Optimization

In this project, two CRISPR–Cas9–based strategies were designed to disrupt the KIF5B–RET fusion oncogene in patient-derived lung cancer organoids. Although measurable Cas9 activity was achieved, overall editing efficiencies remained modest, and no strong phenotypic changes were observed. Several technical and biological factors likely contributed to these outcomes.
An additional and important explanation lies in the biological context of the organoids. The PMU315 organoid line carries the *TP53* C275Y mutation, located within the DNA-binding domain of p53. Mutant p53 alters the cellular response to DNA damage and can shift the balance between DNA repair pathways [62]. Specifically, *TP53* mutations within DBD have been shown to reduce the efficiency of NHEJ, the primary pathway that introduces disruptive indels following CRISPR–Cas9 DSBs [62]. If NHEJ activity is compromised, cells may increasingly rely on alternative, more precise repair mechanisms such as homology-directed repair (HDR) or microhomology-mediated end joining (MMEJ), which can religate double-strand breaks in a manner that maintains the oncogene function [63].
This raises the possibility that CRISPR-induced double-strand breaks at the KIF5B–RET

locus were repaired in a way that preserved the oncogenic reading frame, thereby preventing functional knockout of the fusion. In the context of oncogene addiction [64], TP53 mutant cells may even selectively favor repair outcomes that maintain survival, enabling the fusion to remain functional despite Cas9 cleavage. Therefore, the co-occurrence of the KIF5B–RET fusion with a TP53 mutation is likely to have had a direct impact on the genome-editing outcome.

This interpretation highlights the importance of studying how p53 status influences CRISPR editing outcomes, particularly in cancer models where multiple driver alterations interact. It also reinforces the need to compare editing efficiency of the same CRISPR strategy in TP53-mutant and TP53-unmutant organoids. Such comparisons would clarify whether the reduced editing efficiency observed here stems from technical delivery limitations, p53-dependent DNA repair biases, or both.

To overcome technical limitations, future work could employ engineered cell line models carrying the KIF5B–RET fusion, which would provide a more controlled and reproducible system for testing the targeting strategies and gRNA efficiency before moving to organoid validation. Once efficient gRNAs are established, they could then be introduced into patient-derived organoids to confirm editing and functional effects in a clinically relevant setting.

Alternatively, implementing two lentiviral delivery systems, one lentiviral plasmid delivering Cas9 sequence and another carrying gRNAs and the GFP reporter gene, could overcome the packaging limitations of the large size lentiviral construct. Such separated plasmids have been shown to significantly enhance infection efficiency and enable stable expression of large genetic elements in organoid and primary cell cultures (Chapter 5.1.3).

Despite the technical challenges encountered, this study lays the groundwork for the CRISPR–Cas9–mediated disruption of oncogenic fusion genes in patient-derived lung organoids. Successfully establishing a reliable delivery and editing platform would enable functional analysis of driver mutations directly in physiologically relevant tumor models. This could not only improve our understanding of oncogene dependency but also provide a foundation for personalized genome editing strategies aimed at selectively targeting patient-specific fusion events.

7 Conclusion

In this thesis, CRISPR-based genome editing strategies were applied in patient-derived lung adenocarcinoma organoids to target two clinically relevant genetic alterations and evaluate their biological consequences: the *TP53* C275Y mutation within the DNA-binding domain of p53 and the KIF5B–RET fusion oncogene.

Using adenine base editing (ABE8e), I achieved efficient and precise A→G conversion

at the *TP53* C275Y mutation. Sanger sequencing quantification analysis consistently showed high editing rates, reaching 60–90%, confirming that base editing can be successfully applied in 3D lung cancer organoids. Correction of the mutation resulted in more than 50% depletion of live cells, indicating that mutant *TP53* expression was essential for sustaining oncogenic phenotypes, while reversion toward the wild-type allele may restore a tumor-suppressive transcriptional program. Excitingly, this study establishes a robust workflow for base editing in organoids and demonstrates the feasibility of correcting *TP53* point mutations in lung tumor organoids. It provides an important foundation for future investigations into the functional and transcriptional effects of cancer hotspot mutations and the development of mutation-targeted therapeutic strategies.

Future experiments could include transcriptomic analysis of TP53-corrected organoids to assess activation of the p53 pathway and identify downstream genes that become up-or down-regulated upon mutation correction. Moreover, single cell transcriptomic analysis would reveal whether individual cell populations within the organoid regulate different pathways of cell death or senescence.
To evaluate CRISPR–Cas9 approach for disrupting the KIF5B–RET fusion, two strategies were developed: Fusion breakpoint-targeting, and dual-intron-targeting which designed to delete large genomic segment independent of the exact fusion junction. One of the designed gRNAs successfully induced 10% editing in organoids. However, the editing efficiency was not efficient, and no significant phenotypic effects were detected. These observations indicate that the targeting strategies can be further optimized. One explanation for low editing efficiency is the instability of Cas9 mRNA or the silencing of exogenous mRNA in organoid cells. Previous studies have shown that exogenous nucleic acids (especially those encoding large proteins like Cas9) are prone to transcriptional silencing in mammalian and stem cell–derived systems [56].

This project raises the question of whether the mutant p53 altered DNA damage responses and altered the balance between DNA repair pathways, as has previously been shown [62]. This highlightes the importance of investigating gene expression programs of mutant *TP53* C275Y and corrected *TP53* to understand how such co-occurring mutations influence genome-editing outcomes.

Moving forward, testing the CRISPR-cas9 based targeting strategies in engineered cell lines (after generating the same fusion) before the application to organoids would allow rapid validation of CRISPR-cas9 and gRNA efficiency. Another approach would be to use two separate lentiviral vectors -one encoding Cas9 and another encoding the gRNAs and GFP reporter- to overcome the packaging limitations of a single large lentiviral

construct. Despite these technical challenges, this project establishes the conceptual and experimental foundation for CRISPR–Cas9–mediated disruption of oncogenic fusions in patient-derived lung cancer models. Dual-intron targeting, in particular, offers the advantage of being applicable across multiple patients regardless of individual fusion breakpoint variability, making it a promising strategy for fusion-driven cancers.

The combined findings of both projects highlight the value of establishing CRISPR-based genome-editing platforms in patient-derived organoids to functionally characterize driver mutations in a clinically relevant setting. Moreover, unlike targeted therapies that act at the protein level and therefore remain vulnerable to resistance mechanisms, CRISPR technologies offer the possibility to intervene directly at the genomic origin of oncogenesis. This makes genome editing a fundamentally transformative approach for cancer therapy, capable of permanently correcting or inactivating pathogenic mutations rather than inhibiting their consequences.

References

[1] M. et al. Stratton. “The cancer genome.” In: *Nature* 458 (2009), pp. 719–724. DOI: 10.1038/nature07943.

[2] International Agency for Research on Cancer. *Cancer Today: GLOBOCAN 2022, version 1.1*. https://gco.iarc.who.int/today. World Health Organization, accessed November 13, 2025. 2025.

[3] Herbst et al. “The biology and management of non-small cell lung cancer.” In: *Nature* 553,7689 (2018), pp. 446–454. DOI: 10.1038/nature25183.

[4] Martin Sattler et al. “The expanding role of the receptor tyrosine kinase MET as a therapeutic target in non-small cell lung cancer.” In: *Cell Reports Medicine* (2025). DOI: doi:10.1016/j.xcrm.2025.101983.

[5] Hoe HJ et al. “Treatment of non-small cell lung cancer with RET rearrangements.” In: *Cancer* (2025). DOI: PMID:4017198710.1002/cncr.35779..

[6] Jean-Charles et al. Soria. “Osimertinib in Untreated EGFR-Mutated Advanced Non-Small-Cell Lung Cancer.” In: *The New England journal of medicine* (2018). DOI: doi:10.1056/NEJMoa1713137.

[7] Gomatou G et al. “Osimertinib Resistance: Molecular Mechanisms and Emerging Treatment Options.” In: *Cancers Basel* (2023). DOI: doi:10.3390/cancers15030841..

[8] L.M. et al. Drusbosky. “Therapeutic strategies in RET gene rearranged non-small cell lung cancer.” In: *J Hematol Oncol.* 14, 50. (2021). DOI: https://doi.org/10.1186/s13045-021-01063-9.

[9] Naval G. Daver et al. “Treatment outcomes for newly diagnosed, treatment-naïve *TP53*-mutated acute myeloid leukemia: a systematic review and meta-analysis”. In: *Journal of Hematology & Oncology* 19 (2023). DOI: 10.1186/s13045-023-01417-5.

[10] Akira Mogi and Hiroyuki Kuwano. “TP53 Mutations in Non small Cell Lung Cancer”. In: *Journal of Biomedicine and Biotechnology* (2011). Published January 18, 2011. DOI: 10.1155/2011/583929. URL: https://doi.org/10.1155/2011/583929.

[11] F. et al. Xu. “A TP53-associated gene signature for prediction of prognosis and therapeutic responses in lung squamous cell carcinoma.” In: *OncoImmunology* 9 (1). (2020). DOI: https://doi.org/10.1080/2162402X.2020.1731943.

[12] Lane D P. et al. “Cancer. p53, guardian of the genome.” In: *Nature* 6381 (1992). DOI: doi:10.1038/358015a0.

[13] Lane D. et al. “p53 Research: The Past Thirty Years and the Next Thirty Years.” In: *Cold Spring Harb. Perspect. Biol.* (2010). DOI: doi:10.1101/cshperspect.a000893..

[14] Donehower L. A. et al. “Integrated Analysis of TP53 Gene and Pathway Alterations in The Cancer Genome Atlas”. In: *Cell Rep.* 5 (2019), pp. 1370–1384. DOI: doi:10.1016/j.celrep.2019.07.001.

[15] Guillermina et al. Lozano. “Mutant p53 Gain of Function: Why Many See It, Why Some Do Not.” In: *Cancer discovery* 15 (2025), pp. 1099–1104. DOI: doi:10.1158/2159-8290.CD-24-1638.

[16] Edward R et al. Kastenhuber. “Putting p53 in Context.” In: *Cell* 170 (2017), pp. 1062–1078. DOI: doi:10.1016/j.cell.2017.08.028.

[17] Alvarado-Ortiz E. et al. “Role in Cancer Development, Progression, and Therapeutic Approaches.” In: *Front Cell Dev Biol.* (2021). DOI: 10.3389/fcell.2020.607670..

[18] Nishikawa S. et al. “Drugs Targeting p53 Mutations with FDA Approval and in Clinical Trials.” In: *Cancers (Basel)* (2023). DOI: doi:10.3390/cancers15020429..

[19] Sayed S. et al. “Efficient Correction of Oncogenic KRAS and TP53 Mutations through CRISPR Base Editing”. In: *Journal of Cancer Research* 82.17 (2022). DOI: doi:10.1158/0008-5472.CAN-21-2519.

[20] L.T. et al. Schmitt. “Quantification of evolved DNA-editing enzymes at scale with DEQSeq.” In: *Genome Biol* (2023). DOI: https://doi.org/10.1186/s13059-023-03097-3.

[21] K.J. Harrington et al. “The biology of cancer”. In: *Medicine* 51 (2023). DOI: https://doi.org/10.1016/j.mpmed.2022.10.001..

[22] Tsuta K. et al. “RET-rearranged non-small-cell lung carcinoma: a clinicopathological and molecular analysis.” In: *Br J Cancer* (2014). DOI: doi:10.1038/bjc.2014.36.

[23] Seok Y. et al. “A transforming KIF5B and RET gene fusion in lung adenocarcinoma revealed from whole-genome and transcriptome sequencing.” In: *Genome Research* 22(3) (2012), pp. 436–445. DOI: doi:10.1101/gr.133645.111.

[24] Drusbosky J. et al. “RET fusions as mechanisms of resistance and therapeutic targets in NSCLC.” In: *Cancer Res.,* (2021). DOI: doi:10.1186/s13045-021-01063-9.

[25] S.-H. et al. Chen. “ABL Genomic Editing Sufficiently Abolishes Oncogenesis of Human Chronic Myeloid Leukemia Cells In Vitro and In Vivo.” In: *Cancers* (2020). DOI: https://doi.org/10.3390/cancers12061399.

[26] Broutier L et al. “Human primary liver cancer-derived organoid cultures for disease modeling and drug screening.” In: *Nat Med.* (2017). DOI: 10.1038/nm.4438..

[27] van de Wetering M et al. “Prospective derivation of a living organoid biobank of colorectal cancer patients”. In: *Cell* (2015). DOI: 10.1016/j.cell.2015.03.053..

[28] Daisong et al. Wang. “Human organoids as 3D in vitro platforms for drug discovery: opportunities and challenges.” In: *Nature reviews Drug discovery* (2025). DOI: doi:10.1038/s41573-025-01317-y.

[29] Haque MR et al. “Patient-derived pancreatic cancer-on-a-chip recapitulates the tumor microenvironment.” In: *Microsyst Nanoeng.* (2022). DOI: doi:10.1038/s41378-022-00370-6..

[30] Matthew A et al. Coelho. “Base editing screens map mutations affecting interferon-signaling in cancer.” In: *Cancer cell vol.* (2023). DOI: doi:10.1016/j.ccell.2022.12.009.

[31] M. Jinek et al. “A programmable dual-RNA-guided DNA endonuclease in adaptive bacterial immunity.” In: *Science (New York, N.Y.)* (2012). DOI: doi:10.1126/science.1225829.

[32] JE. Garneau et al. “The CRISPR/Cas bacterial immune system cleaves bacteriophage and plasmid DNA.” In: *Nature* (2010). DOI: doi:10.1038/nature09523.

[33] MA. Hossain et al. “CRISPR-Cas9: A fascinating journey from bacterial immune system to human gene editing.” In: *Progress in molecular biology and translational science* (2021). DOI: doi:10.1016/bs.pmbts.2021.01.001.

[34] Villiger Lukas et al. “CRISPR technologies for genome, epigenome and transcriptome editing.” In: *Nature reviews, Molecular cell biology.* (2024). DOI: doi:10.1038/s41580-023-00697-6.

[35] Tarun S. et al. “CRISPR-based genome editing through the lens of DNA repair.” In: *Molecular Cell* (2022). DOI: https://doi.org/10.1016/j.molcel.2021.12.026..

[36] C. Xue et al. “DNA Repair Pathway Choices in CRISPR-Cas9-Mediated Genome Editing.” In: *Trends in genetics* 37,7 (2021), pp. 639–656. DOI: doi:10.1016/j.tig.2021.02.008.

[37] NM Gaudelli et al. “Programmable base editing of A•T to G•C in genomic DNA without DNA cleavage.” In: *Nature* 551,7681 (2017), pp. 464–471. DOI: doi:10.1038/nature24644.

[38] M. F. et al. Richter. “Phage-assisted evolution of an adenine base editor with improved Cas domain compatibility and activity.” In: *Nat Biotechnol* 38 (2020), pp. 883–891. DOI: doi.org/10.1038/s41587-020-0453-z.

[39] Mohadeseh et al. Khoshandam. “Clinical applications of the CRISPR/Cas9 genome-editing system: Delivery options and challenges in precision medicine.” In: *Genes and Diseades* 11.1 (2024), pp. 268–282. DOI: https://doi.org/10.1016/j.gendis.2023.02.027..

[40] S. et al. Tang. “Overcoming the Delivery Challenges in CRISPR/Cas9 Gene Editing for Effective Cancer Treatment: A Review of Delivery Systems.” In: *International Journal of Medical Sciences* (2025). DOI: https://doi.org/10.7150/ijms.112724..

[41] H.S. Kim et al. W. Kim S. Lee. “Targeting mutant KRAS with CRISPR-Cas9 controls tumor growth.” In: *Genome Res.* 28.3 (2018), pp. 374–382. DOI: doi:10.1101/gr.223891.117.

[42] Ling et al. Li. “Non-viral delivery systems for CRISPR/Cas9-based genome editing: Challenges and opportunities.” In: *Biomaterials* 171.1 (2018), pp. 207–218. DOI: doi:10.1016/j.biomaterials.2018.04.031.

[43] Dominik Witzigmann et al. “Lipid nanoparticle technology for therapeutic gene regulation in the liver.” In: *ELSEVIER* (2020), pp. 4–33. DOI: doi.org/10.1016/j.addr.2020.06.026.

[44] Julian D et al. Gillmore. “CRISPR-Cas9 In Vivo Gene Editing for Transthyretin Amyloidosis.” In: *The New England journal of medicine* 385 (2021), pp. 493–502. DOI: doi:10.1056/NEJMoa2107454.

[45] Lisa N et al. Kasiewicz. “GalNAc-Lipid nanoparticles enable non-LDLR dependent hepatic delivery of a CRISPR base editing therapy.” In: *Nature communications* 14 (2023). DOI: doi:10.1038/s41467-023-37465.

[46] Heidi et al. Ledford. “World’s first personalized CRISPR therapy given to baby with genetic disease.” In: *Nature* (2025). DOI: 10.1038/d41586-025-01496-z.

[47] H. et al. Frangoul. “CRISPR-Cas9 gene editing for sickle cell disease and -thalassemia.” In: *N. Engl. J. Med.* 384 (2021), pp. 252–260. DOI: 10.1056/NEJMoa2031054.

[48] US National Library of Medicine. “EDIT-301 for Autologous Hematopoietic Stem Cell Transplant (HSCT) in Participants With Transfusion-Dependent Beta Thalassemia (TDT)”. In: *ClinicalTrials.gov.* NCT05444894 (2023). DOI: https://clinicaltrials.gov/ct2/show/.

[49] Robert et al Chiesa. “Base-Edited CAR7 T Cells for Relapsed T-Cell Acute Lymphoblastic Leukemia.” In: *The New England journal of medicine.* 389 (2018), pp. 899–910. DOI: doi:10.1056/NEJMoa2300709.

[50] Sanger Sequencing service. “Microsynth AG. Schützenstrasse 15 · P.O. Box · 9436 Balgach · Switzerland Phone +41 71 722 83 33 · info@microsynth.ch”. In: (). DOI: https://www.microsynth.com/company-overview-ch.html.

[51] F Ann et al. Ran. “Double nicking by RNA-guided CRISPR Cas9 for enhanced genome editing specificity.” In: *Cell* 154,6 (2013). DOI: doi:10.1016/j.cell.2013.08.021.

[52] Mali P. et al. “RNA-guided human genome engineering via Cas9.” In: *Science* 339.6121 (2013), pp. 823–826. DOI: DOI:10.1126/science.1232033.

[53] Neldeborg S et al. “Dual intron-targeted CRISPR-Cas9-mediated disruption of the AML RUNX1-RUNX1T1 fusion gene effectively inhibits proliferation and decreases tumor volume in vitro and in vivo.” In: *Leukemia* 37 (2023), pp. 1792–1801.

[54] Mali P et al. “In vivo CRISPR/Cas9 targeting of fusion oncogenes for selective elimination of cancer cells.” In: *Nature Communications* 339.5060 (2020). DOI: doi.org/10.1038/s41467-020-18875.

[55] Hadi Esmaeili Gouvarchin Ghaleh et al. “Concise review on optimized methods in production and transduction of lentiviral vectors in order to facilitate immunotherapy and gene therapy.” In: *Biomedicine Pharmacotherapy* 128 (2020). DOI: https://doi.org/10.1016/j.biopha.2020.110276..

[56] Battulin N. et al. “The human EF1a promoter does not provide expression of the transgene in mice”. In: *Transgenic Res.* 31 (2022), pp. 525–535. DOI: 10.1007/s11248-022-00319-5.

[57] Jiaying et al. Han. “-Globin Lentiviral Vectors Have Reduced Titers due to Incomplete Vector RNA Genomes and Lowered Virion Production.” In: *Stem cell reports* 16 (2021). DOI: doi:10.1016/j.stemcr.2020.10.007.

[58] Thermo Scientific™. “Phusion™ High-Fidelity DNA Polymerase Product Information Sheet”. In: *thermofischer.com/support* (January 2020). DOI: Pub.No.MAN0012393.

[59] Muhammad Tanveer Khan et al. “Optimizing PCR amplification of GC-rich nicotinic acetylcholine receptor subunits from invertebrates.” In: *Biochemistry and Biophysics Reports* 42 (2025). DOI: https://doi.org/10.1016/j.bbrep.2025.102052..

[60] M et al. Kumar. “Systematic determination of the packaging limit of lentiviral vectors.” In: *Human gene therapy* 12,15 (2001), pp. 1893–905. DOI: doi : 10 . 1089/104303401753153947.

[61] J. et al. Kim. “Loss of Cas9 expression due to epigenetic silencing limits genome editing efficiency in human stem cells”. In: *Frontiers in Genome Editing* 3 (2021).

[62] Ferdinandos et al. Skoulidis. “Co-occurring genomic alterations in non-small-cell lung cancer biology and therapy.” In: *Nature reviews.* (2019), pp. 495–509. DOI: 10.1038/s41568-019-0179-8.

[63] Fagherazzi P et al. “Specific TP53 mutations impair the recruitment of 53BP1 to DNA double-strand breaks underlying the mechanism of radioresistance.” In: *Eur Biophys J.* (2025). DOI: doi:10.1007/s00249-025-01774-8..

[64] H. et al. Wang. “Targeting p53 pathways: mechanisms, structures and advances in therapy.” In: *Sig Transduct Target Ther* (2023). DOI: https://doi.org/10.1038/s41392-023-01347-1.

8 Supplement

gRNAs Combination for Dual-Intron-Targeting				
Oligo Nr.	**KIF5B::RET**	**Sequences of gRNAs designed for cloning**	**PCR Amplicon Number**	**Transfer Vector Number**
oSS_B1	oSS_KIF5B_Intron8	AAAGGACGAAACACCGACTCTAGTTCAACCCATAAG GTTTTAGAGCTAGAAATAGCAAG	PCR 5	PL5
oSS_B12	oSS_RET_Intron19	TTCTAGCTCTAAAACCTCAGAGGCCACCCGGC ACTGGATCCAAGGTGTCTCATAC		
oSS_B2	oSS_KIF5B_Intron9	AAAGGACGAAACACCGTGTGTAAGTTAGTTGT CTTTGTTTTAGAGCTAGAAATAGCAAG	PCR 6	PL6
oSS_B11	oSS_RET_Intron18	TTCTAGCTCTAAAACCCCATGCCTGTCTGTAG AGAGGATCCAAGGTGTCTCATAC		
oSS_B3	oSS_KIF5B_Intron12	AAAGGACGAAACACCGCATCTCCCCGACCTG ATCCAGTTTTAGAGCTAGAAATAGCAAG	PCR 7	PL7
oSS_B10	oSS_RET_Intron17	TTCTAGCTCTAAAACGGGCCATCTGGAATTAC CTTGGATCCAAGGTGTCTCATAC		
oSS_B4	oSS_KIF5B_Intron14-A	AAAGGACGAAACACCGAGTAGAGTATGTATCC ACCCGTTTTAGAGCTAGAAATAGCAAG	PCR 8	PL8
oSS_B9	oSS_RET_Intron16	TTCTAGCTCTAAAACCCTGCTCGGCTCTCATG CTCGGATCCAAGGTGTCTCATAC		
oSS_B5	oSS_KIF5B_Intron14-B	AAAGGACGAAACACCGGATTTTCGAGCACTTC GGAGGTTTTAGAGCTAGAAATAGCAAG	PCR 9	PL9
oSS_B8	oSS_RET_Intron15-B	TTCTAGCTCTAAAACCACTGCACTAAGGACAT AAAGGATCCAAGGTGTCTCATAC		
oSS_B5	oSS_KIF5B_Intron14-B	AAAGGACGAAACACCGGATTTTCGAGCACTTC GGAGGTTTTAGAGCTAGAAATAGCAAG	PCR 10	PL10
oSS_B7	oSS_RET_Intron15-A	TTCTAGCTCTAAAACCGGGTCAGTATGCTGCC AGGGGATCCAAGGTGTCTCATAC		
oSS_B5	oSS_KIF5B_Intron14-B	AAAGGACGAAACACCGGATTTTCGAGCACTTC GGAGGTTTTAGAGCTAGAAATAGCAAG	PCR 11	PL11
oSS_B6	oSS_RET_Intron13	TTCTAGCTCTAAAACCTCTGATGGAAAGTGAC CACGGATCCAAGGTGTCTCATAC		

Figure S1: **gRNA sequence and construct designs used for dual intron targeting of the KIF5B::RET fusion.** Each gRNA oligo contains a 20-nt target-specific protospacer sequence (shown in red) flanked by vector-specific cloning sequences. The 5' flanking region includes the U6 promoter-compatible overhang and restriction site for cloning (TTCTAGCTCTAAAAC), while the 3' flanking region corresponds to the beginning of the sgRNA scaffold sequence. PCR amplicon numbers and transfer vector identifiers are listed for reference.

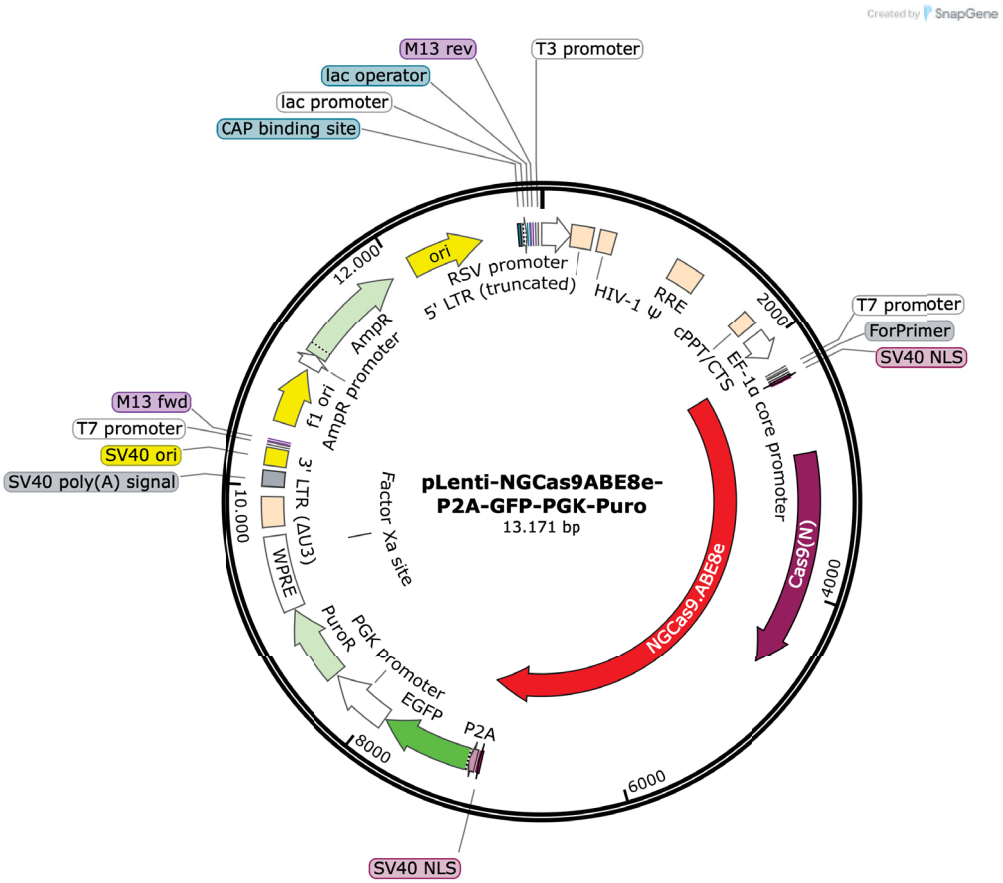

Figure S2: pLenti.NGCas9ABE8e.P2A.GFP.PGK.Puro vector used for delivering Adenine Base Editor after cloning the ABE8e sequence. Addgene number: 242000

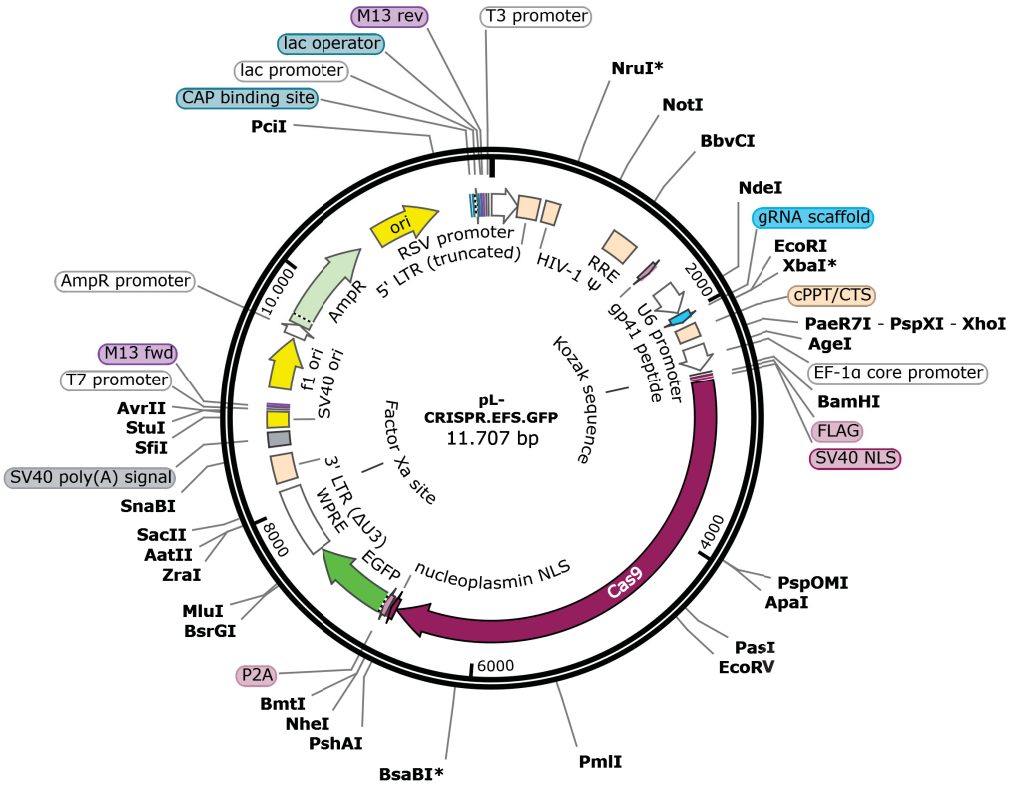

Figure S3: pL-CRISPR.EFS.GFP.U6sgRNA all in one vector used for delivering gRNA, Cas9 and GFP in the experiments of Breakpoint and Dual-Intron Targeting of fusion oncogene KIF5B-RET. The BP-gRNA (or DI-gRNAs) together with scaffold sequence were cloned after U6 promoter.Addgenenumber: 57818

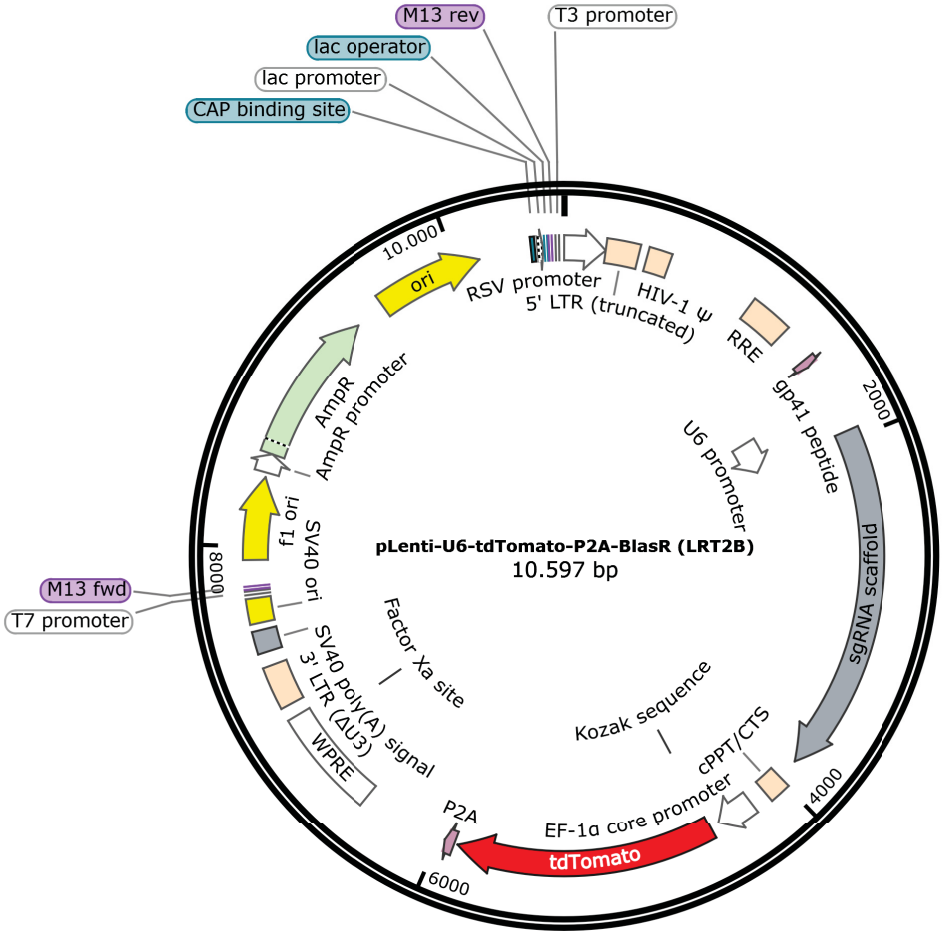

Figure S4: pLenti.U6sgRNA.EFS.Tdtomato.BlastR vector used for delivering Base Editing sgRNAs and tdTomato reporter gene. The sgRNA and scaffold sequence are cloned after U6 promoter. Addgene number: 110854

9 Acknowledgments

During my thesis journey, I have had the privilege of meeting and working with many wonderful people whose support made this work possible. My deepest gratitude goes to everyone who walked alongside me during this time. In particular, I would like to thank:

First and foremost, **Prof. Frank Buchholz** (TU Dresden, BIOTEC Center) and **Prof. João Matos** (University of Vienna) for their long-term supervision and guidance. Their support has shaped both my scientific thinking and my confidence as a researcher. I am grateful to **Prof. Martin Wermke** for giving me the opportunity to learn and explore organoid research within the NCT environment.

A special and heartfelt note of appreciation goes to **Dr. Shady Sayed** for his exceptional mentorship, continuous support, and the remarkable motivation he offered whenever I needed it the most. His dedication, patience, and encouragement were truly unique, and I remain deeply grateful for the impact he had on both my work and my development as a scientist.

I would also like to thank **Dr. Carina Wenzel** and **Annika Pätzold** from the NCT for their advice and for introducing me to organoid culture.

My appreciation extends to all **members of the Buchholz Lab**, past and present, for creating such a collaborative and motivating atmosphere. I am grateful to my colleagues, especially **Pascal Wang**, **Nico Sandoval** and **Haidy Hasan** who became not only coworkers but friends. Thank you for the after-work conversations, the laughs, and for lifting my spirits on days when experiments refused to cooperate. A small but heartfelt thanks go to the Caruso Pasta Bar at the university hospital cafeteria, whose reliably delicious meals provided energy, and the occasional much-needed boost between experiments.

Outside the lab, I am incredibly thankful to my friends for their understanding during the long periods of absence and for always cheering me on despite busy schedules and distance. And to my **boyfriend**, thank you for being a constant source of patience, strength, and support, no matter how long my days were or what mood I was in.

Last but certainly not least, my deepest gratitude goes to my **parents**, whose unwavering belief in me has been the foundation of every achievement in my life. To my **sisters** and **brothers**: thank you for standing by me even from long distances. Your encouragement crossed borders and I felt it every step of the way.